The Dissertation Committee for Tae Jin Kim Certifies that this is the approved version of the following dissertation:

Pressure and Thermal Effects on Superhydrophobic Friction Reduction in a Microchannel Flow

Committee:

Carlos Hidrovo, Supervisor

David Bogard

Li Shi

Halil Berberoglu

Thomas Truskett

Pressure and Thermal Effects on Superhydrophobic Friction Reduction in a Microchannel Flow

by

Tae Jin Kim, B.S.; M.S.

Dissertation

Presented to the Faculty of the Graduate School of

The University of Texas at Austin

in Partial Fulfillment

of the Requirements

for the Degree of

Doctor of Philosophy

The University of Texas at Austin

August 2013

Dedication

I dedicate this dissertation to my wife for her emotional support in completing my Ph.D. degree throughout the years. Even during times when I had doubts about my path, she was one who continued to believe in me and cheered me on. I cannot imagine how grateful and blessed I am to have her as my wife. I also dedicate this dissertation to my son for becoming a new member of our family. He has given me the purpose to become a proud father.

I am grateful of my parents for their continuous encouragement and sharing their wisdom whenever we encountered hardships. I would also like to thank my brother for his support and being a good buddy.

Acknowledgements

I wish to thank my principal investigator, Dr. Carlos Hidrovo, for being a patient advisor and sharing his knowledge during my Ph.D. degree. I am thankful that he was open to discussions regardless of his busy schedules, and respect his belief that teaching is as important as research. I would also like to thank Dr. David Bogard, Dr. Halil Berberoglu, Dr. Li Shi, Dr. Thomas Truskett for sharing their valuable times to serve on my dissertation committee.

I would like to acknowledge Arnav Chhabra, Ravitej Kanapuram, Juan Trejo, Sungyun Hann and Harrison Leva for being great undergraduate assistants and have relentlessly researched with me. I have enjoyed working with them and would like to wish them best of luck in their future careers.

Finally, I would like to thank my lab members for their helpful discussions and advices.

Pressure and Thermal Effects on Superhydrophobic Friction Reduction in a Microchannel Flow

Tae Jin Kim, Ph.D.

The University of Texas at Austin, 2013

Supervisor: Carlos Hidrovo

As the fluidic devices are miniaturized to improve portability, the friction of the microchannel becomes intrinsically high and a high pumping power will be required to drive the fluid. Since the pumping power delivered by portable devices is limited, one method to reduce this is to render the surface to become slippery. This can be achieved by roughening up the microchannel wall and form a bed of air pockets between the roughness elements, which is known as the superhydrophobic Cassie-Baxter state.

While the study on superhydrophobic microchannels are focused mainly in maximizing the friction reduction effects and maintaining the stability of the air pockets, less attention has been given to characterizing the microchannel friction under a metastable state, where partial flooding of the micro-textures may be present, and under heated conditions, where the air pockets are trapped between the micro-textures. In order to quantify the frictional characteristics, microchannels with micron-sized trenches on the side walls were fabricated and tested under varying inlet pressures and heating conditions.

By measuring the hydrodynamic resistance and comparing with numerical simulations, results suggest that (1) the air-water interface behaves close to a no-slip boundary condition, (2) friction becomes insensitive to the wetting degree once the

micro-trenches become highly wetting, (3) the fully wetted micro-trench may be beneficial over the de-wetted ones in order to achieve friction reduction effects and (4) heating the micro-trenches to induce a highly de-wetting state may actually be detrimental to the microchannel flow due the excessive growth of the air layer.

As part of the future work to characterize heat transfer in superhydrophobic microchannels, a rectangular microchannel with microheaters embedded close to the side walls was fabricated and the corresponding heat transfer rates were measured through dual fluorescence thermometry. Results suggested that significant heat is lost through the environment despite the high thermal resistance of the microchannel material. An extra insulation is suggested prior to characterizing the convective heat transfer coefficients in the superhydrophobic microchannel flow.

TABLE OF CONTENTS

CHAPTER 1

INTRODUCTION

1.1 Overcoming the Pumping Power Limit in Microfluidics

Principles of microfluidics have received considerable attention due to the ongoing miniaturization of fluidic systems. Application of Lab-on-a-chip devices includes drug delivery systems, diagnostic tools, and industrial/environmental testing apparatuses. One example of implementing a Lab-on-a-chip device is a diagnostic tool to detect HIV or Syphilis virus, where the hand held device can be rapidly tested in the field.

While miniaturization of the fluidic system has a multitude of benefits such as reduction of reagent use, large data collection with only a small amount of samples, and precise control of the fluidic path, the pumping power required to drive the fluid becomes significantly large as the channel cross-sectional dimensions are reduced. In order to reduce the pumping power, there are a few parameters that may be controlled:

- Microchannel dimensions
- Fluid temperature
- Flow rate of the working fluid
- Friction on the walls

Figure 1. Lab-on-a-chip HIV/Syphilis detection device for rapid sampling (C. Torres, 2011, Washington Post).

Since the purpose of portable fluidic devices is miniaturization, it is usually undesirable to alter the channel dimensions. Moreover, since many fluidic devices involve medical reagents, the fluid should be under controlled temperature conditions. While it looks simple to reduce the flow rate, microchannels generally operate under creep to low Reynolds number situations; hence the majority of these portable fluidic devices operate under low flow rate conditions. An effective alternative to reduce the pumping power requirements is to reduce the friction incident on the wall itself, thus replacing the traditional no-slip boundary condition at the wall to a reduced shear boundary condition. This reduction of the wall shear stress can be achieved by rendering the microchannel walls into superhydrophobic surfaces.

1.2 Superhydrophobic Surfaces and Friction Reduction

A surface is said to be under a superhydrophobic state if the droplet dispensed on top of the surface forms a static contact angle greater than 150°. Even though the liquid droplets forms a very high contact angle, two possible modes exist in the superhydrophobic state: the Wenzel state where the liquid droplet clings onto the surface, and the Cassie-Baxter state where the droplet rolls off the surface at an angle of inclination less than 5°. The Cassie-Baxter state (Fig. 2) is of particular interest as it is believed to reduce the hydrodynamic resistance, thus reducing the pumping power requirements to drive the fluid. This surface can be accomplished by microtexturing the surface, embedding an air layer underneath the liquid layer and hence lowering the effective surface energy of the surface. The resulting surface has a higher tendency to repel water, reducing the contact angle hysteresis with relatively simple surface modifications.

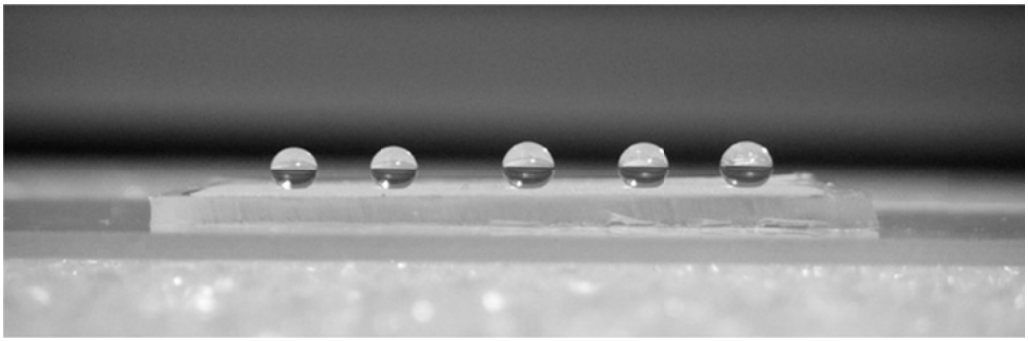

Figure 2. Water droplets bead on top of a rough surface under superhydrophic state.

1.3 Recent Developments in Application of Superhydrophobic Surfaces

Superhydrophobic surfaces, particularly the Cassie-Baxter state, have received considerable attention due to its reduced hydrodynamic resistance. The primary objective of most work in this area has been focused on minimizing the hydrodynamic resistance and hence the pumping power to drive fluid in the microfluidic systems. The slip length (Fig. 3), a quantification of how much the wall boundary condition deviates from the no-slip boundary condition, has been experimentally and theoretically/numerically calculated for various types of surface roughness configurations. Studies have shown that the slip length is generally larger if the roughness elements of the walls are connected throughout the texturing in the axial direction. Other approaches to maximize the slip length include rendering the roughness elements to nano-scale, modifying the roughness shape, or increasing the air pocket size trapped between the roughness elements.

Another area of interest in the study of superhydrophobic surfaces has been focused on delaying the flooding of water into the air pockets. Methods used to prolong the Cassie-Baxter state includes using nano-sized features as the surface texturing, chemically coating the roughness elements with a low surface energy solution, and artificially introducing air into the cavities.

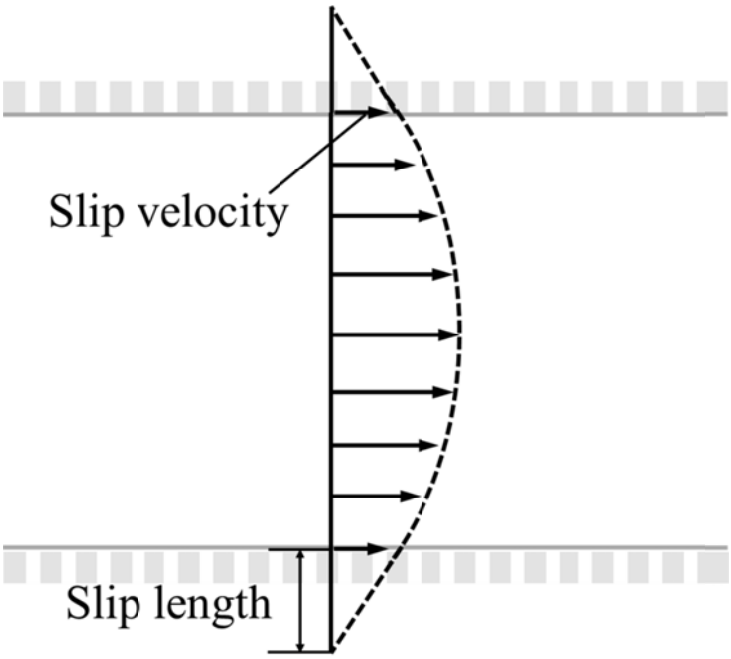

Figure 3. Schematic diagram of slip length in an internal flow with a rough surface.

1.4 Further Exploring the Behavior of Superhydrophobic Surfaces to Friction Reduction

While studies have been rigorously performed to quantify and maximize the slip in superhydrophobic surfaces or to maintain the Cassie-Baxter state under elevated pressures, the effects of the partially wetting microtextures on the friction reduction effects under different temperature conditions have received less attention and require further consideration.

Toward this end, this dissertation will focus three major topics:

- Study of the stability of the Cassie-Baxter state in a pressure driven flow and the partial wetting effects of the roughness elements on the friction reduction characteristics. The experiments in the first section have been performed under room temperature conditions.
- Study of stability of superhydrophobic microchannel under heated conditions. The air-water interface change is observed as the microchannel temperature is increased and the flow rate change of the microchannel is compared with the baseline microchannel with smooth walls.
- Developing apparatus and methodology to enable study of convective effects in a microchannel under elevated temperatures. In this section, the microchannel is heated to explore the effects of heating on the microchannel friction and the convective heat transfer effects.

CHAPTER 2

FRICTION REDUCTION EFFECTS IN A MICRO-TEXTURED MICROCHANNEL

2.1 Introduction

Friction reduction in the microchannel walls can help reduce the pumping power requirements as the pressure drop required to flow the fluid is inherently large owing to its small cross-sectional area. One possible way of achieving friction reduction is using surface microtexturing that can lead to a superhydrophobic Cassie-Baxter state, where the air pockets trapped between the microtextures promote the wall to be 'slippery'.

The major study in this area is geared towards optimizing the surface microtexturing geometry to maximize the friction reduction effects. Studies have shown that the slip length is greater if the air pockets within the roughness elements are not isolated but rather connected throughout the texturing,[1-2] Other approaches used to maximize the slip length include modifying the surface texture shape,[3-4] reducing the roughness element size to the nano-scale[5-7], and increasing the size of the air pockets. [8]

Another research topic of interest is maintaining the air pockets under elevated pressures. Prevention of liquid flooding into the air cavities has been rigorously studied because once the cavities are wetted, termed as the Wenzel state,[9] it is difficult to transition back to the Cassie-Baxter state.[8] Methods used to prevent liquid flooding include applying air between the cavities,[10] roughening up the surface texturing with nano-scale roughness elements,[11-12] and chemically coating an already rough surface with

a low surface energy material.[13-14] Instead of delaying the air pockets from flooding into the air pockets, a number of studies performed experiments which artificially transitioned from the Wenzel state back to the Cassie-Baxter state. Such examples include utilizing electrolysis to form hydrogen bubbles as the gas layer,[15] injecting air into the cavities[16] or boiling the flooded microtextures and filling the cavities with vapor.[17]

While various studies were performed to increase the slip length or maintain a Cassie-Baxter state, less attention has been paid to friction in partially wetting microtextures and the correlation between the liquid-gas interface location and the microchannel flow characteristics. Toward this end, this section will focus on the stability of the Cassie-Baxter state in a Poiseuille flow and the effects of partial roughness wetting have on the friction reduction characteristics. To properly visualize the gas-liquid interface and monitor its degree of penetration into the microtexturing, microchannels with an array of isolated trenches on the side were designed and fabricated. Global flow friction characteristics obtained from pressure versus flow rate measurements were correlated against micro-trench wetting conditions collected from this visualization setup. The experimental results for this particular enclosed microgeometry suggest that 1) the frictional characteristics of the air-water interface more closely resembles a no-slip condition rather than a shear-free behavior possibly due to immobilization of the air-water interface by contamination and/or constraining nature of the microgeometry, 2) the friction reduction is rather insensitive to liquid penetration into the roughness elements, at least for the geometries tested here and, related to these two previous corollaries, 3) fully wetted Wenzel state micro-trenches provide better friction reduction than de-wetted, air filled Cassie state micro-trenches.

2.2 Background – Fundamentals of Superhydrophobic Surfaces

2.2.1 Young's Equation and Contact Angle

Since the major phenomenon of interest is the Cassie-Baxter state, where pockets of air exist between the microtexture cavities, the three-phase interface characteristics are an important parameter. If a liquid is dispensed on a solid substrate, the liquid will either completely wet or partially wet the solid substrate. This depends on the spreading parameter,

$$S = \gamma_{SV} - (\gamma_{SL} + \gamma) \tag{1}$$

where γ_{SG} is the solid-vapor surface energy, γ_{SL} is the solid-liquid surface energy and γ is the liquid-vapor surface energy, or what is commonly referred as surface tension. If $S > 0$, the surface will try to lower its energy by spreading the dispensed liquid, and if $S < 0$ the liquid will try to minimize its footprint by forming a compact droplet or dome on the substrate.

When $S < 0$, the work δw required to displace the droplet if the liquid is advanced by a distance dx is,

$$\delta w_{in} = (\gamma_{SL} - \gamma_{SV})\, dx + \gamma (dx \cdot \cos\theta_Y) \tag{2}$$

Figure 4. Schematic representation of the spreading parameter. The liquid forms a dome if the spreading parameter is negative.

In Eq. (2), it can be inferred that when the liquid is displaced, the solid-liquid surface energy is expended by $\gamma_{SV} dx$ and the liquid-vapor surface energy is expended by $\gamma \cos\theta dx$, while the solid-vapor surface energy is gained by $\gamma_{SV} dx$. Under equilibrium conditions, $\delta w_{in} = 0$ and cancelling out dx yields,

$$\cos\theta_Y = \frac{\gamma_{SV} - \gamma_{LV}}{\gamma} \tag{3}$$

where θ_Y is known as the Young's contact angle (Fig. 5). It is customary to say that a surface is hydrophilic if the Young's contact angle is less than 90˚ and hydrophobic if the angles is greater than 90˚.

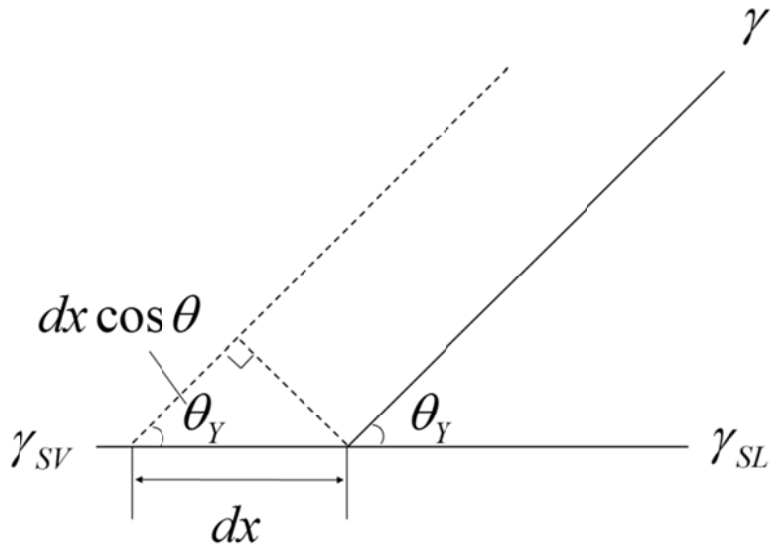

Figure 5. Schematic representation of Young's contact angle.

2.2.2 Superhydrophobic States

Using the same analogy as Section 2.2.1, the contact angle of superhydrophobic states can be expressed in terms of the three surface energies involved. For the Wenzel case (Fig. 6), where all the surface texture beneath the liquid droplet are fully wetted,

$$\delta w_{in} = r\left(\gamma_{SL} - \gamma_{SV}\right)dx + \gamma(dx \cdot \cos\theta_W) \tag{4}$$

where r is the roughness factor, a ratio of the actual rough area over the nominal flat area. Under equilibrium conditions ($\delta w_{in} = 0$) and solving for the contact angle yields,

$$\cos\theta_W = r \cdot \cos\theta_Y \tag{5}$$

As can be seen in Eq. (5), the only difference between the Wenzel's effective contact angle and the Young's contact angle is the roughness factor. Since the Young's contact angle assumes a perfectly smooth surface, the Wenzel state takes into account the actual rough surface with complete interstitial wetting. One thing to note is that the roughness factor acts as an amplification factor ($r > 1$), hence the Wenzel state is not limited only to superhydrophobic surfaces. If the surface is hydrophobic (>90˚), Eq. (5) will result in an even larger contact angle, while if the surface is hydrophilic (<90˚), the equation will result in a smaller contact angle.

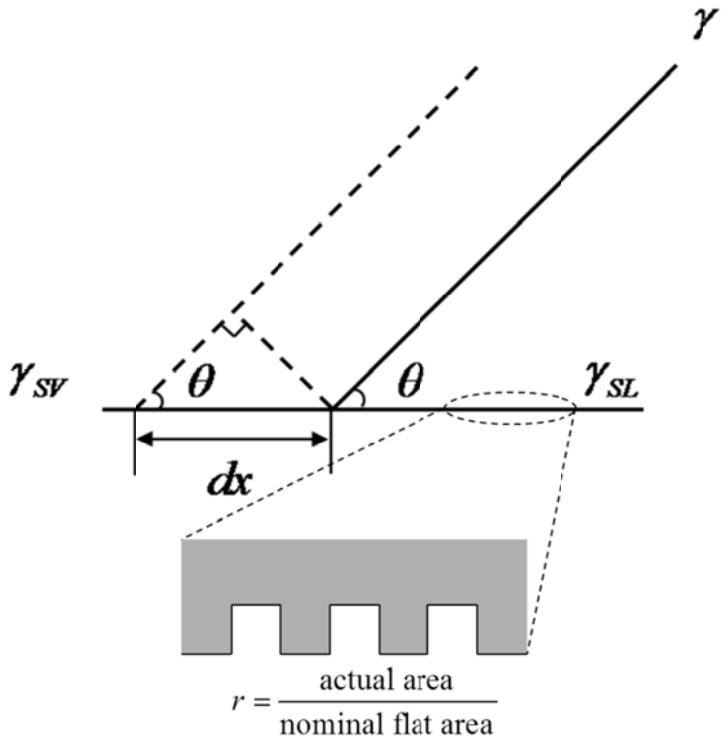

Figure 6. Schematic representation of the Wenzel state, where all the liquid wets the surface roughness elements.

The Cassie-Baxter case (Fig. 7) is different from the Wenzel case in principle, even though the contact angle between the two states can be identical. Surfaces under the Cassie-Baxter state involves and extra air-water interface underneath the liquid droplet and the work energy is expressed as,

$$\delta w_{in} = f_1 \left(\gamma_{SL} - \gamma_{SV} \right) dx + f_2 \gamma dx + \gamma (dx \cdot \cos \theta_{CB}) \tag{6}$$

where f_1 is the fraction between the area of the solid-liquid interface and the nominal flat area, and f_2 is the fraction between the area of the liquid-vapor interface underneath the droplet and the nominal flat area. Under equilibrium conditions ($\delta w_{in} = 0$),

$$\cos \theta_{CB} = f_1 \cos \theta_Y - (1 - f_1) \tag{7}$$

As seen in Eq. (7), $f_2 = 1 - f_1$, and the portion of the air-water interface underneath the liquid droplet is essentially -1 since the maximum achievable contact angle is 180˚ ($\cos \pi = -1$). As a portion of the area underneath the liquid droplet is exposed to air, this leads to a reduced hydrodynamic resistance incident on the walls.

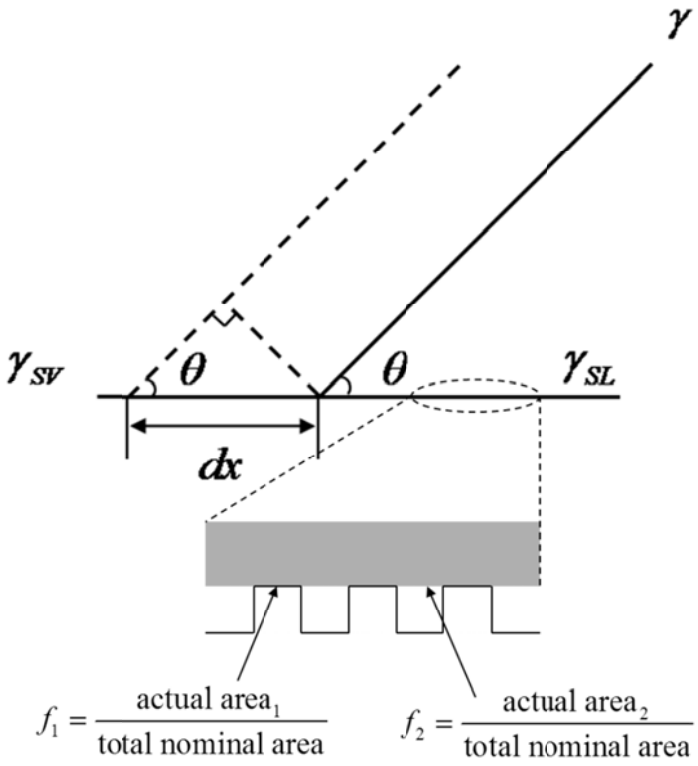

Figure 7. Schematic representation of the Cassie-Baxter state, where there are portions of liquid making contact with the solid surface and portions of liquid exposed to the air.

2.2.3 Behavior of Darcy Friction Factor-Reynolds Number Product in Smooth Duct Flows

Since the microchannel with superhydrophobic walls, particularly the Cassie-Baxter state, is under a reduced shear boundary condition, comparison should be made to quantify the deviation from the conventional duct flow conditions. The appropriate parameter to compare this deviation from the no-slip boundary condition is the Darcy friction factor-Reynolds number product (fRe), which quantifies the friction of a duct flow for a given channel geometry. The Darcy friction factor is expressed as,

$$f = 4C_f = \frac{\tau_w}{\frac{1}{2}\rho\bar{u}^2} \tag{8}$$

where C_f is the skin friction factor, τ_w is the shear stress at the wall, ρ is the fluid density and $\bar{u}$ is the average velocity in the axial direction. The fRe then can be written as,

$$fRe = 4Po = 4\frac{\Delta PA}{pL}\cdot\frac{1}{\frac{1}{2}\rho\bar{u}^2}\cdot\frac{\rho\bar{u}D_h}{\mu} = \frac{2\Delta PD_h{}^2A}{\mu QL} \tag{9}$$

where Po is defined as the Poiseuille number, ΔP is the pressure drop across the microchannel, A is the cross sectional area, p is the perimeter of the cross-section, μ is the fluid viscosity, Q is the volumetric flow rate and D_h is the hydraulic diameter ($\frac{4A}{p}$).

The friction of the duct flow with no-slip boundary condition has been very well established, both experimentally and analytically/numerically.[18] Analytically, the relation between the flow rate and the pressure drop is strictly a function of the channel dimensions,

$$Q = \frac{4ba^3}{3\mu}\left(-\frac{dp}{dx}\right)\left[1-\frac{192a}{\pi^5 b}\sum_{i=1,3,5,\ldots}^{\infty}\frac{\tanh(i\pi b/2a)}{i^5}\right] \tag{10}$$

where a is the half width, b is the half height, μ is the viscosity of the fluid and $-dp/dx$ is the pressure gradient in the axial direction.

In this chapter, the fRe of the microchannel with superhydrophobic walls will be compared to the fRe of the baseline, which is the rectangular microchannel with a flat solid wall. As will be discussed in further sections, friction reduction effects were observed with superhydrophobic microchannels. However, the value of the fRe did not stay constant with increased Re due to the air-pockets trapped within the micro-textures.

2.3 Experimental Methods

2.3.1 Side-trenched Microchannel Fabrication

In order to efficiently track the air-water interface location in each of the artificial surface roughness, the microtextures are designed as isolated micro-trenches on the side walls oriented transverse to the water flow (Fig. 8). With this design, the air-water interface location in individual micro-trenches can be visualized. To our knowledge, the study presented here is the first attempt to experimentally quantify the partial wetting effects on friction using larger aspect ratio microchannels (~1:1) with significant friction reduction effects from the superhydrophobic surfaces.

To prepare the microchannels, a bare silicon wafer was spin coated with Su-8 2050 negative photoresist (Microchem) where the replicating mold for the PDMS microfluidic channels layouts were created through photolithographic procedures. The wafer was then silanized (UCT specialties, LLC) for at least an hour in a vacuum

desiccator to fluorinate the Su-8 replicating mold. This procedure will prevent the cured PDMS from prematurely bonding and damaging the Su-8 mold. A PDMS base and solvent (Dow Corning) mixture, with a volume ratio of 10:1, was poured onto the mold and cured at 80°C for 2 hours. The cured PDMS with microfeatures was then peeled off the mold and sliced into individual slabs. A complimentary set of PDMS slabs without microfeatures were fabricated and bonded to the featured PDMS slabs using an oxygen plasma cleaner (Harrick Plasma) at 29 Watts for 20 seconds.

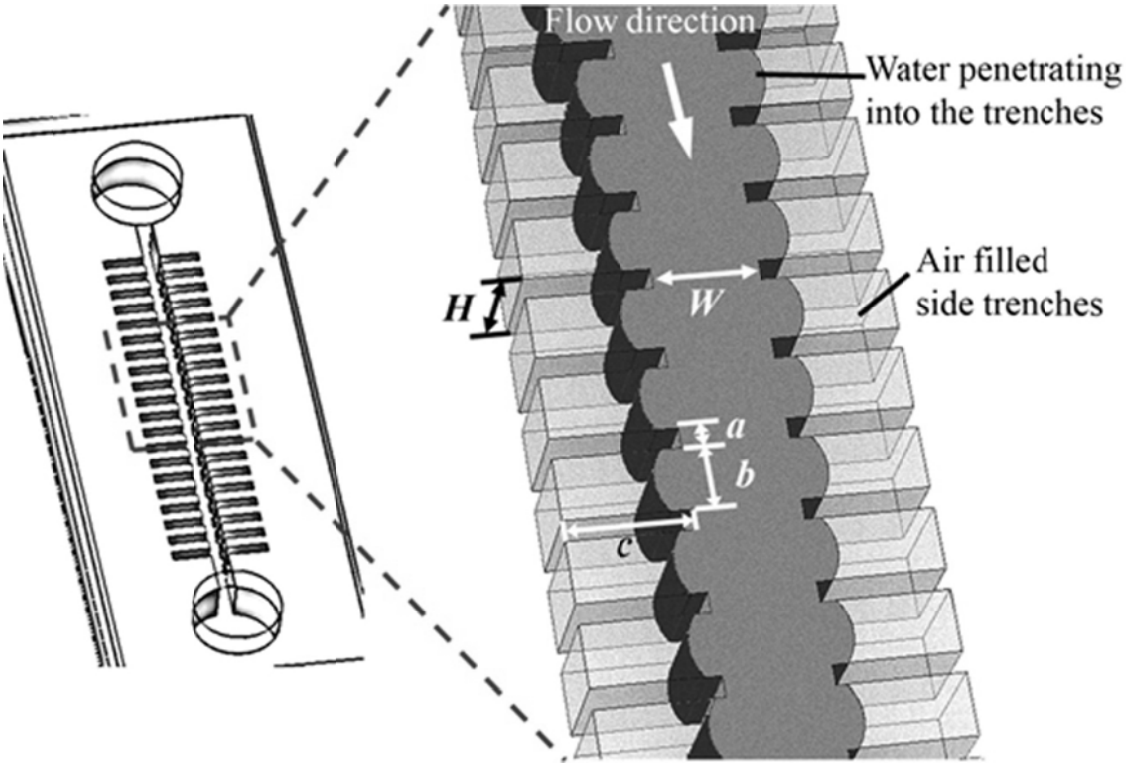

Figure 8. A schematic diagram of a side trenched microchannel with liquid penetrating into the air cavities. More penetration is to be expected upstream of the microchannel than downstream since the pressure is higher. Due to the nature of photolithography and the replicating process,[19-20] the microchannels have a trapezoidal cross-section rather than a rectangular one.

Prior to conducting tests, the microchannel samples dimensions (Table 1) were measured through optical microscopy (M=40×, NA=0.60). Careful measurement of the actual microchannel dimensions are required[21] since the friction analysis is quite sensitive to the channel geometry and dimensions.

Table 1. Mean measured dimensions of the PDMS microchannel for each micro-trench configuration (N=5) and the uncertainty due to instrument and measurement errors. Measurements were taken at multiple locations along the extent of each microchannel sample. The land (a=15μm and a=55μm) represents the nominal distance between one edge to the other, and the baseline is the microchannel without any micro-trenches on the side walls.

Trench Dimension (μm)	W_{bottom}		W_{top}		H	
	Mean (μm)	Uncert. (μm)	Mean (μm)	Uncert. (μm)	Mean (μm)	Uncert. (μm)
Baseline	94.2	0.6	106.3	0.2	125.3	1.3
a= 15, b= 65 c= 30	103.7	0.6	105.3	0.4	124.7	1.3
a= 15, b= 65, c= 60	106.6	0.7	104.5	0.2	124.9	1.2
a= 15, b= 65, c= 120	111.6	1.0	103.9	0.2	123.8	1.2
a= 15, b= 65, c= 230	110.5	1.3	104.5	0.2	123.8	1.2
a= 55, b= 65, c= 30	95.5	0.3	106.8	0.3	124.3	1.2
a= 55, b= 65, c= 60	95.9	0.5	106.7	0.2	123.1	1.3
a= 55, b= 65, c= 120	96.4	0.4	106.1	0.2	121.1	1.3
a= 55, b= 65, c= 230	95.9	0.4	106.3	0.3	120.3	1.3

2.3.2 Differential Pressure Setup

A constant pressure head setup and a differential mass measurement system (Fig. 9) are used to assess the hydrodynamic resistance of the microchannel samples. For the constant pressure head source, a water reservoir with a controllable column height is used to generate a constant differential pressure inside the microchannel.

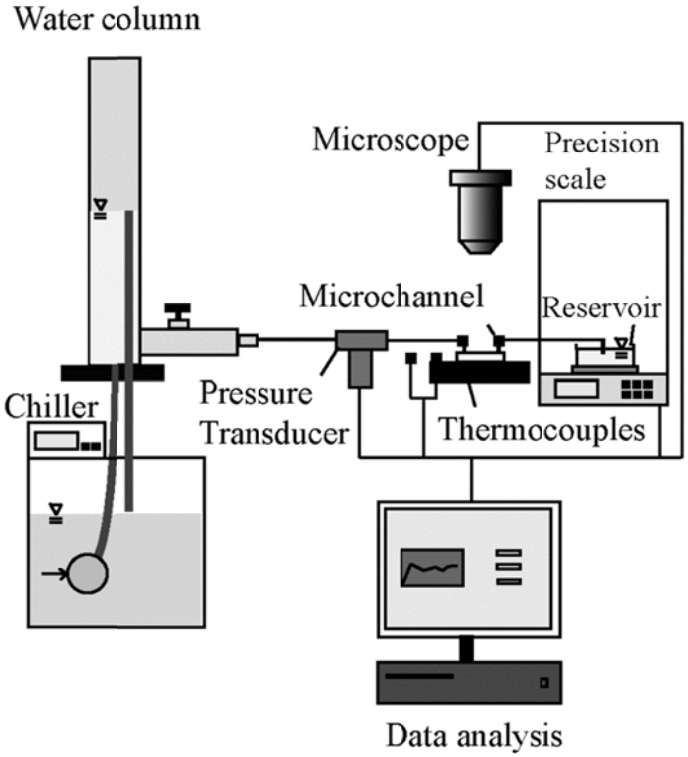

Figure 9. Schematic diagram of the experimental setup. Pressure drop, flow rate and temperature are measured during a microchannel sample experiment. The experiments were performed 5 to 6 sets for each micro-trench configurations, and newly fabricated PDMS microchannels were used for each trial. By using a new microchannel for each trial, contamination issues are minimized.

The water was supplied to the reservoir from a liquid pump submerged in a water chiller while a draining pipe in the reservoir controlled the height of the water column. In order to maintain the water temperature as constant as possible, the chiller is set at room temperature. By controlling the water column height, the differential pressure from the microchannel inlet to the outlet ranged from 800Pa to 6000Pa with an increment of 400Pa. The pressure drop was measured by connecting a differential pressure transducer (PX 409, Omega) to the tubes connecting the inlet and outlet of the microchannels. Since the differential pressure transducer was connected between the microchannel inlet and outlet ports, an extra procedure to estimate the losses between the two pressure taps have been performed, which is explained in the forthcoming sections.

Also, it was observed that if the outlet pressure was lower than atmospheric conditions, the air pockets in the left and right trenches merged together, cutting off the flow. This is due to the hydrophobic characteristics of PDMS which tends to de-wet the surface, and along with the mildly vacuum condition at the outlet section, the air pockets will significantly expand into the water layer. In order to prevent this, the absolute pressure inside the microchannel was increased above atmospheric conditions by placing the water collection reservoir approximately 10cm above the PDMS microchannel exit. Consequently, the absolute pressure in the microchannel was expected to increase approximately 1000Pa throughout the microchannel.

An example of the merging air layers if the microchannel experiences vacuum pressure conditions is shown in Fig. 10. The inlet of the microchannel is submerged in a water reservoir exposed to the atmosphere and the outlet is connected to a vacuum line with a negative differential pressure of 6000Pa. While this is an exaggerated case, results suggest that the pressure of the water flow should be under positive gage pressure

throughout the microchannel in order to prevent excessive growth of the air pockets if the pressure near the outlet is under mild vacuum conditions.

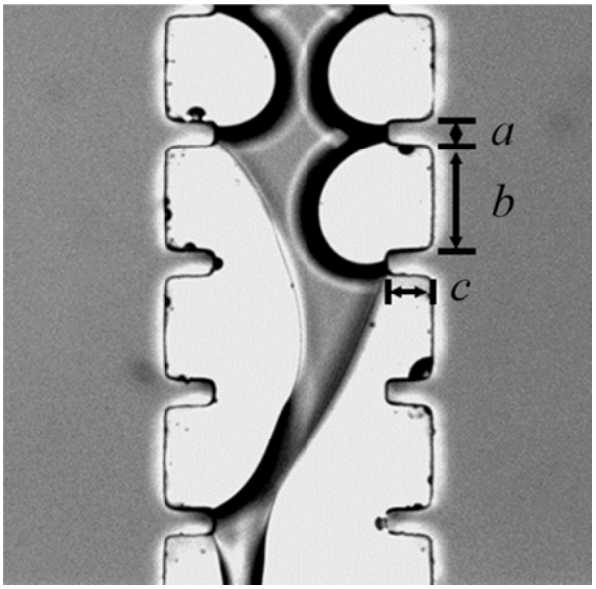

Figure 10. Micrograph (M= 10×, NA= 0.3) of a trenched microchannel (a= 15μm, b= 65μm, c= 30μm) at approximately 10% from the downstream. The air pockets immediately expanded as soon as the vacuum was applied to the microchannel and the flow was disrupted.

Flow rate measurements of the microchannels were performed by having the outlet tube from the microchannel submerged in a water reservoir resting on a precision balance (GH-252, A&D Weighing). Caution should be taken to ensure that the outlet tube is sufficiently submerged in the water reservoir. If the outlet tube is not submerged but raised above the reservoir, the water will form droplets and drip on the reservoir. This

will lead to a significant error in the pressure reading mainly because the internal pressure will change with the droplet curvature, where the relation can be expressed in terms of the Laplace pressure,

$$\Delta P = \frac{\gamma}{2\Re}, \tag{11}$$

where γ is the surface tension of the air-water interface and $\Re$ is the radius of curvature assuming a spherical droplet shape. As long as the outlet tube is submerged in the water reservoir, the pressure variation due to the Laplace pressure will not be an issue.

Since the water reservoir is exposed to the environment, the evaporation rate from the reservoir was accounted for each of the flow rate data, where the average evaporation rate was measured as 0.9μl/min. With the differential pressure and the flow rate data with the evaporation rate account for, the friction in the microchannel can be calculated. However, as indicated by Lauga and Stone,[22] changes in viscosity is also considered since this may lead to errors when quantifying the hydrodynamic resistance in the microchannel flow. Since the water viscosity decreases between 2 and 3% even for a temperature increase of 1°C, monitoring the water temperature was necessary. Two thermocouples were embedded at the inlet and outlet tubes to measure the average water temperature, and the changes in viscosity were assessed for each experiment. The viscosity values based on the average temperature measurement for each experiment were then applied to the friction factor data.

2.3.3 Uncertainty Analysis for *fRe*

Since the *fRe* and the Re (= $\rho UD_h / \mu$) involve multiple parameters, uncertainly analysis must be performed in order to ensure confidence to the data. The propagation of error for *fRe* is expressed as,

$$\frac{\delta(fRe)}{fRe} = \sqrt{\left(\frac{\delta(\Delta P)}{\Delta P}\right)^2 + \left(\frac{\delta A}{A}\right)^2 + \left(2\frac{\delta D_h}{D_h}\right)^2 + \left(\frac{\delta \mu}{\mu}\right)^2 + \left(\frac{\delta Q}{Q}\right)^2 + \left(\frac{\delta L}{L}\right)^2} \quad (12)$$

where the parameters have been explained in Eq. (9). Note should be taken for the hydraulic diameter since 2 has been multiplied in order to account for the power relation, where $\delta(fRe) = \frac{\partial(fRe)}{\partial D_h}\delta(D_h)$. Likewise, the propagation of error for *Re* is,

$$\frac{\delta(Re)}{Re} = \sqrt{\left(\frac{\delta \rho}{\rho}\right)^2 + \left(\frac{\delta Q}{Q}\right)^2 + \left(\frac{\delta D_h}{D_h}\right)^2 + \left(\frac{\delta \mu}{\mu}\right)^2 + \left(\frac{\delta A}{A}\right)^2} \quad (13)$$

It should be noted that the uncertainty mentioned above has two components: bias error and precision error, and the total uncertainty u_T can be expressed as,

$$u_T = \sqrt{B^2 + P^2} \quad (14)$$

where *B* is the bias uncertainty and *P* is the precision uncertainty.

The bias error in Eq. (14) is a systematic error which is inherent to the sample or equipment used in the experiments and is insensitive to the sample size. The uncertainty due to the bias error B can be evaluated based on equipment specifications and measured values of the microchannel dimensions (Table 2), where each bias error component can be implemented in Eq. (9) and (10).

Table 2. Bias error evaluation for the friction reduction experiment, where the bias B is based on the RSS of the individual uncertainty components.

Component	$\frac{\delta(\Delta P)}{\Delta P}$	$\frac{\delta(Q)}{Q}$	$\frac{\delta(\mu)}{\mu}$	$\frac{\delta(A)}{A}$	$\frac{\delta(D_h)}{D_h}$	B_{fRe}	B_{Re}
Bias error (%)	1.1	0.7	1.4	0.6-1.0*	0.9-1.3*	2.0-2.9	1.8-2.5

*The uncertainty range represents individual errors measured from microchannels with different micro-trench configurations (a=15μm, 55μm and c=30μm, 60μm 120μm, 230μm).

Another approach to the bias uncertainty is to test the baseline microchannel with smooth walls and measure how much the experimental fRe deviates from the theoretical values. From the residual error graph ($= fRe_{exp} - fRe_{theo}$), the bias error can be seen as the discrepancy between the average experimental value and the theoretical value, and the random error is the data scatter (Fig. 11). The bias error in this approach is estimated to be ~0.4%, which is significantly smaller than the errors indicated in Table 2. The error analysis performed throughout this experiment will be based on the bias error from the propagation of error approach since this encompasses all the uncertainty from measurement/specifications.

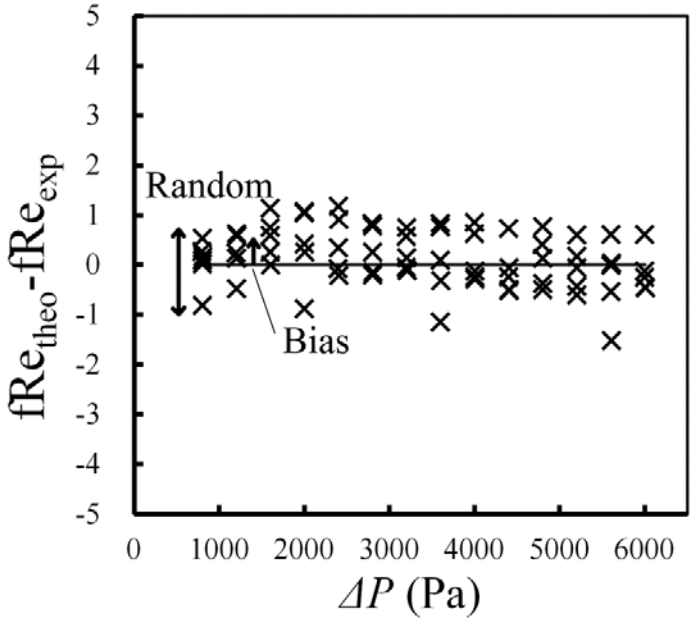

Figure 11. Plot of residual error vs. differential pressure. The *y*-axis value of each data point represents the deviation from the theoretical value.

On the other hand, the precision error *P* in Eq. (14) is a random error which occurs during the repeating experiments and represents how reproducible the data is. Since 5~6 experimental sets have been collected, the standard deviation of the mean is used to calculate the precision error. The precision error is then expressed as,

$$P = t_{v,95\%} \cdot \frac{\sigma}{\sqrt{N}} \quad (95\%) \tag{15}$$

where σ is the standard deviation, N is the number of experimental sets performed, $t_{v,\%}$ is the Student t-distribution variable and $v \equiv (N-1)$. It should be noted that while

$t_{v,95\%} \sim 2$ for a large number of samples, the value may become larger for smaller samples. Since 5~6 experimental sets have been performed, the corresponding $t_{v,95\%}$ implemented in Eq.(12) is 2.571~2.77[23]. For *fRe* and *Re*, the standard deviation of the mean has been used to analyze the precision error instead of propagating the errors in individual measurements since this enables a direct observation of the scatter of the dimensionless variables[24].

2.3.4 Liquid-air Interface Visualization

In addition to evaluating *fRe* and *Re* and the uncertainties involved, micrographs of the air-water interface location within the micro-trenches were taken throughout the microchannel extent (Fig. 12). The micrographs were acquired with an upright microscope (LV100D-U, Nikon) connected to a scientific Charge-Coupled Device (CCD) camera (CoolSnap HQ, Photometrics). Each image covered 3.5% of the entire microchannel length (18.5mm), and was taken at 12 marked locations with an even spacing of 1.65mm from the microchannel inlet to the outlet.

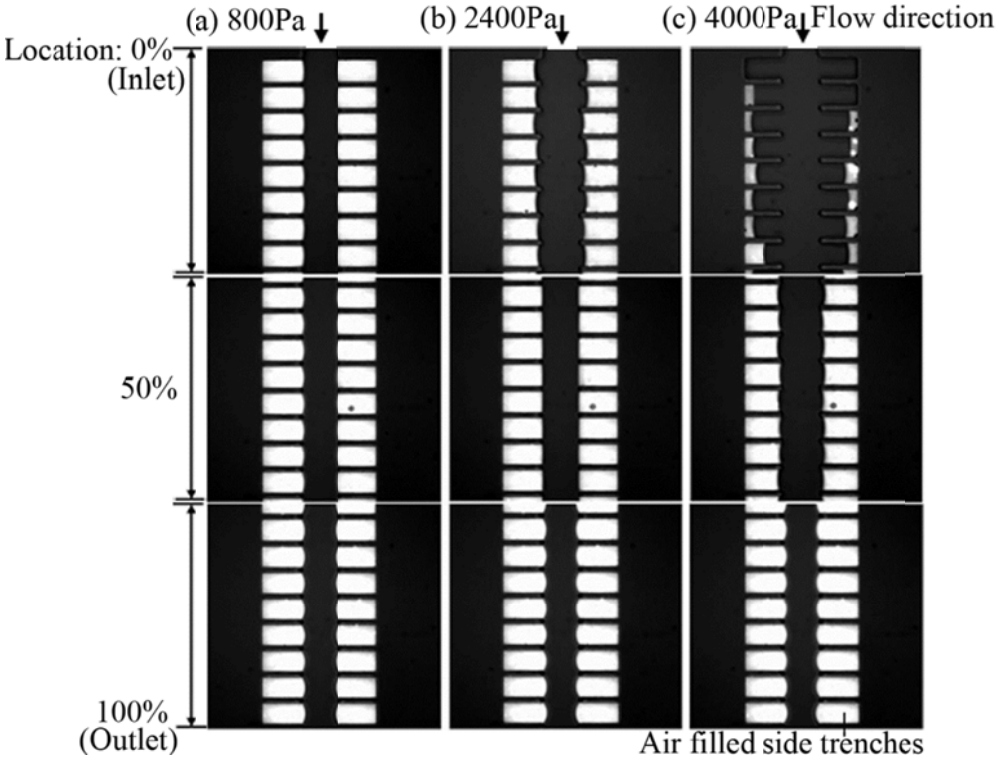

Figure 12. Microscopic images (M= 10×, NA= 0.3) of a micro-trenched microchannel (a= 15μm, b= 65μm, c= 120μm) under different differential pressures. As the inlet pressure is increased, the water layer overcame the Laplace pressure and started to penetrate into the micro-trenches. By observation, pressure is the largest near the inlet where water penetration is the deepest.

The air-water interface visualization data was primarily used in order to determine the location of the air-water interface, and if the water flooded into the micro-trenches, the degree of the water penetration was quantified as well. If the air-water interface was located at the edge or at the round vertex of the micro-trench base, the microchannel was considered as non-wetted. On the other hand, if the interface traveled into the micro-

trench gap and resided between the straight walls, the microchannel was considered as partially wetted. If the water flooded the micro-trenches and no air pockets were detected, the microtrenches were considered as fully wetted. Once the air-water interface invaded the trench, the penetrated distance was measured to evaluate the partial wetting effects on the microchannel friction. The air-water interface visualization data was also used to address the negative penetration associated with the trapped air bubbles invading into the main microchannel section. This flow pinching effect is an occurrence that would normally occur under lower inlet pressure conditions that would impact the measured friction as described later on.

2.3.5 Numerical Simulation of Local Hydrodynamic Resistance

Two numerical *fRe* bounds (COMSOL) are established by taking into accounting for the changes in cross-sectional flow area with location over the micro-trench gap section, and modeling the available air-water interface data as either 1) a solid wall or 2) a shear-free layer (Fig. 13). To calculate the two numerical limits, information on the comprehensive total hydraulic resistance value ($R_h = \Delta P/Q$) is required, which is a sum of the local resistances numerically solved for individual microtrenches with different effective flow width w_{eff}.

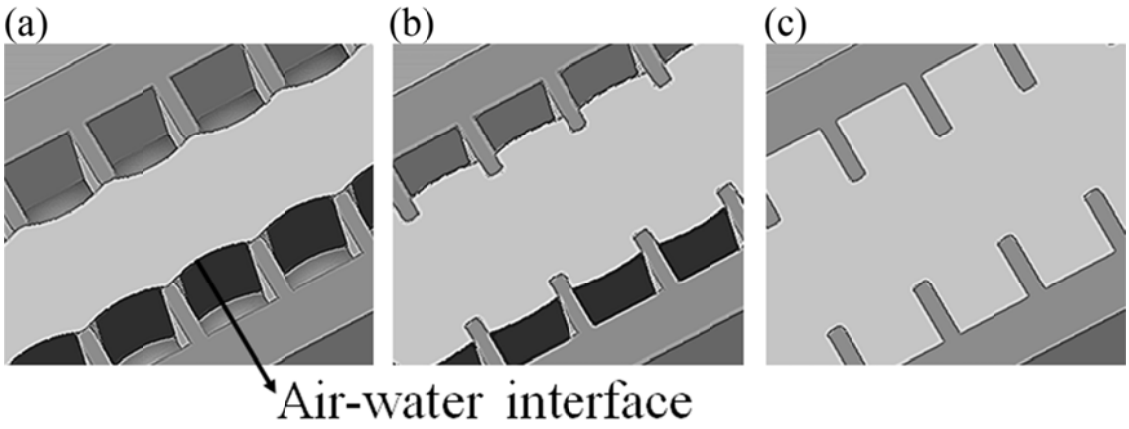

Figure 13. Example of COMSOL modeling for (a) de-wetted case, (b) partial wetted case into the microtrenches and (c) fully wetted case.

The w_{eff} was measured by averaging the distance between the two air-water interfaces, where two pairs of micro-trenches were selected over 12 locations equally spaced at 1.65mm from the microchannel upstream to downstream. In order to emulate the actual flow conditions over the micro-trenches, the curvature of the air-water interfaces and the round micro-trench edges were measured from the micrographs and were implemented in the numerical model. For each w_{eff} data, periodic trenches with the same w_{eff} were modeled until the flow was globally fully-developed (though locally the flow is constantly developing), and the corresponding hydrodynamic resistance was measured. The micro-trenched microchannels were assumed to be globally fully developed throughout the entire channel since the effective flow area changes were small and smooth. In order to determine if the flow is globally fully-developed, the pressure drop of the simulation results in the axial direction was tracked. When the pressure drop between each micro-trench period did not change significantly, the flow over that micro-

trench was said to be globally fully-developed. The individual resistances were then compiled and the total resistance for the entire microchannel was obtained for each *Re*.

It should be noted that a no-slip boundary condition is assumed at the solid wall section between the micro-trenches despite recent findings that some finite slip occurs in hydrophobic walls.[25-27] Since the slip length is in the nanometer scale, which is much smaller than the microchannel dimension, the slip effects on the solid wall can be neglected in this region despite the hydrophobic nature of PDMS.

2.4 Results

2.4.1 Friction vs. Reynolds Number

In order to quantify and compare the partial wetting effects on the microchannel friction, the microchannel friction was acquired over a range of Reynolds number conditions.

Fig. 14 represents the flow rate versus ΔP for different microchannel configurations, where the baseline experiment is the microchannel with flat side walls. In the figure, The flow rate of the microchannels with the smaller solid fraction ($\phi_S = a/(a+b) = 0.19$) increases with pressure at a higher rate than the ones with the larger solid fraction (ϕ_S=0.45). This result is not surprising as it is consistent with the conventional belief that smaller ϕ_S results in a larger effective slip.[8]

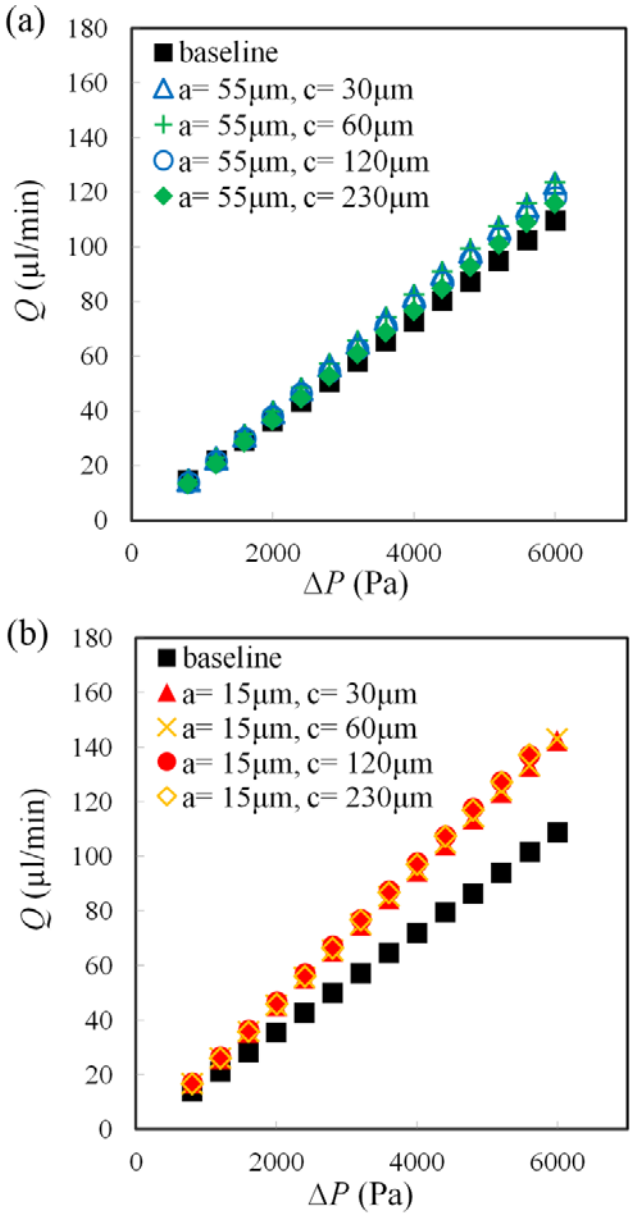

Figure 14. Flow rate versus differential pressure for microchannels with (a) a= 55µm, b= 65µm (blue and green online) and (b) a= 15µm, b= 65µm (yellow and red online) for c= 30µm, 60µm, 120µm and 230µm. The baseline plot is for a microchannel with smooth side walls, and the error bars represent the total uncertainty of 5 to 6 repeated experiments.

The appropriate dimensionless parameter to compare frictional characteristics for laminar duct flow with different microtexture configurations is the *fRe*. To reiterate, the *fRe* for an internal laminar flow is given by,

$$fRe = \frac{2\Delta P \cdot AD_h^2}{\mu QL} \tag{9}$$

where A is the nominal cross-sectional area of the non-trenched (land) section, D_h is the nominal hydraulic diameter of the non-trenched section, and μ is the averaged fluid (water) viscosity. Since the actual ΔP is measured at the external tubes connected to the microchannel inlet and outlet, all the experimentally measured ΔP were adjusted by offsetting the numerically estimated ΔP (COMSOL) from the converging inlet and the diverging outlet sections. Based on the numerical results, the experimental values were reduced by approximately 8%, and by applying the offset value to Eq. (9), the *fRe* can be calculated based on the pressure drop in the micro-trenched section only.

As observed in the baseline data (Fig. 15) based on the adjusted ΔP, the equation agrees extremely well with the theoretical value line. It should be noted that *Re* is used as the *x*-axis to provide a physical understanding between dimensionless variables. The *Re* range varies with each microchannel configuration because the inlet pressure was controlled rather than the flow rate.

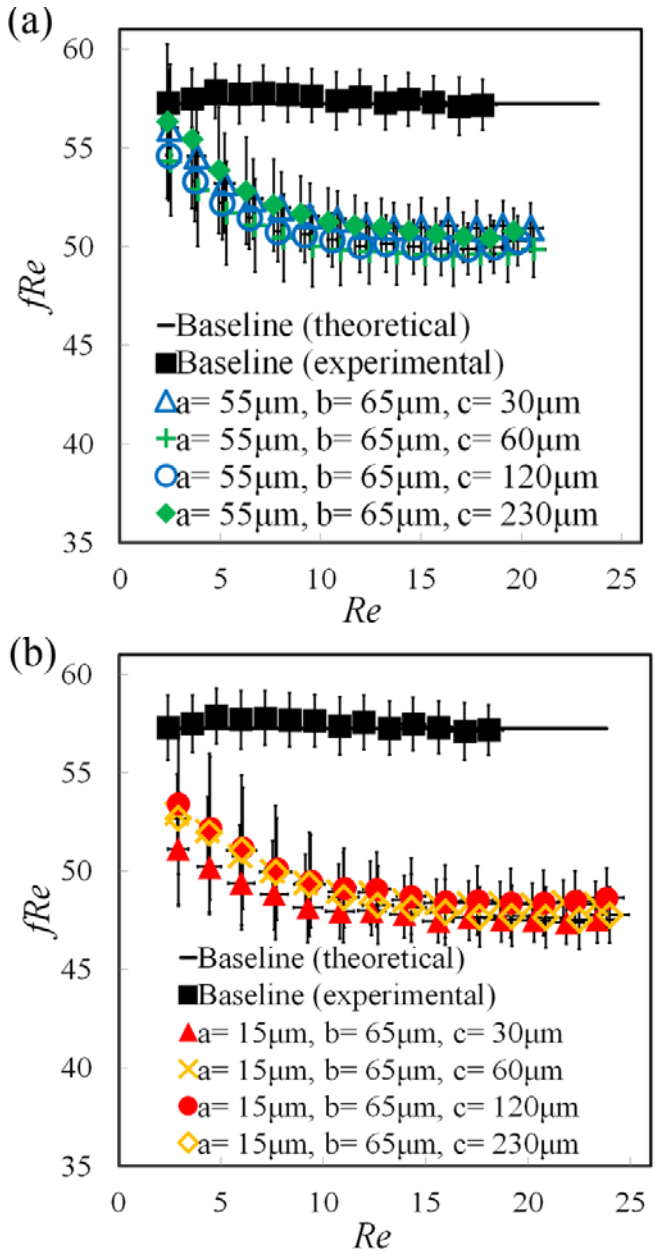

Figure 15. Graph of *fRe* vs. *Re* for (a) *a*= 55µm and (b) *a*= 15µm, where the error bars represent the total uncertainty error for 5~6 experimental sets (Eq. (11)). The theoretical *fRe* value for the baseline is ~ 57.2.[18] In the lower *Re*, *fRe* starts off at a larger value and then levels off approximately at *Re* ~ 10. The major and the minor losses from the

external tubing are neglected since the combined losses account for 0.2 – 0.3% of the major loss in the microchannel.

Several interesting features can be inferred from Fig. 15: 1) in $Re < 10$ the fRe drops drastically with increasing Re and 2) in $10 < Re < 24$ the fRe becomes rather insensitive to Re. To understand the reasons behind these trends, the experimental data is compared with two bounding limits of the fRe obtained from numerical results.

2.4.2 Comparison with Numerical Results of the Effective Friction

As mentioned in Section 2.3.4, two numerical extremes of the fRe can be established by modeling the air-water interface as either 1) a solid wall or 2) a shear-free layer while taking into account the varying cross-sectional flow area in the micro-trench gap section. To calculate the two numerical limits, information on the comprehensive hydrodynamic resistance value ($R_h = \sum R_{local}$) is required, where R_{local} is the local hydrodynamic resistance of a single trench section.

In order to numerically solve the R_{local}, the effective flow width w_{eff} was measured by averaging the distance between the two air-water interfaces, where two pairs of trenches were selected over 12 equally spaced locations from the microchannel upstream to downstream. Since the gage pressure decreases as the water travels downstream, the reduction in pressure leads to the de-wetting of the micro-trench cavities, particularly near the microchannel outlet. For micro-trench cavities near the outlet, where the absolute pressure is the smallest, the air-water interface protrudes into the microchannel.

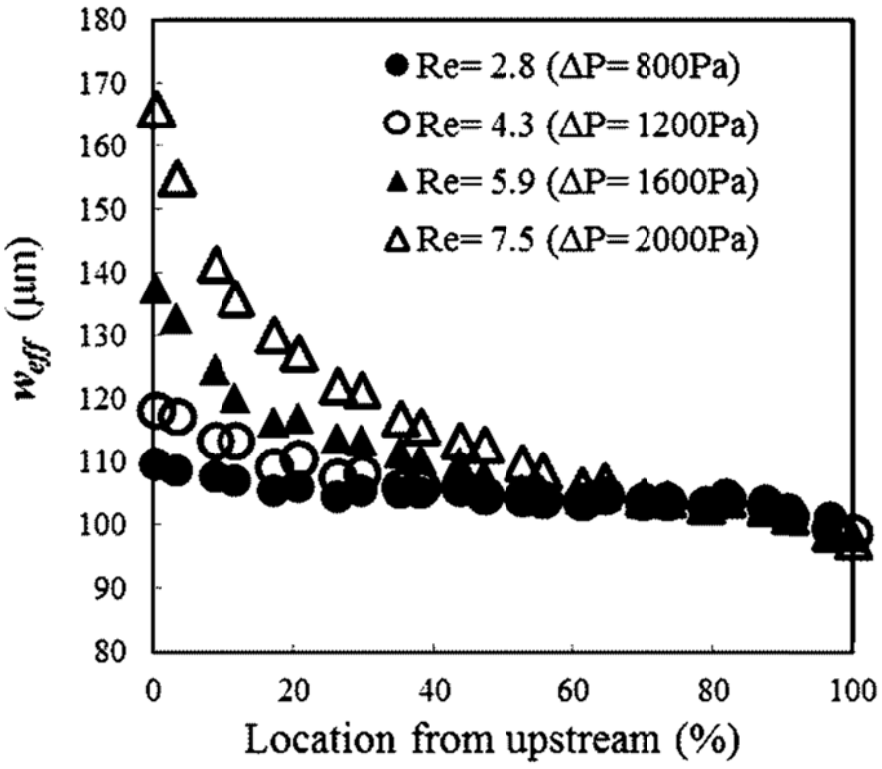

Figure 16. Graph of w_{eff} vs. microchannel location (a= 15μm, b= 65μm, c= 60μm). The w_{eff} data is measured based on the micrographs and is applied to the numerical simulation. Since the microchannel height is constant, the change in w_{eff} represents the change in flow area.

Fig. 16 is an example of the measured effective width vs. distance along the microchannel length. For ΔP = 800Pa, the absolute pressure near the inlet is close to atmospheric conditions. Hence, most of the micro-trenches are de-wetted with a relatively constant w_{eff} along the microchannel. As the inlet pressure is increased, the w_{eff} increases as well, indicating that the water has penetrated into the micro-trenches.

It has been a traditional practice in analytical models that the air-water layer is treated as a perfect shear-free layer, and the effective slip length is calculated by integrating the shear-free region and no-slip region.[22, 28-29] The trenches are not actually assumed in these models, but rather modeled as ducts with patches of walls that either has no-slip or shear-free boundary condition. While this analogy is equivalent to the methodology employed to calculate the lower $fRe_{numerical,\ shear\text{-}free}$ frictional bound in Fig. 16, the experimental data trends more closely to the upper $fRe_{numerical,\ no\text{-}slip}$ frictional bound, both in terms of frictional values and overall behavior with increasing *Re*.

The two numerical bounding *fRe* limits are calculated by implementing the w_{eff} data and are compared with the experimental *fRe* value (trench dimensions of a= 15μm, b= 65μm and c= 60μm). As expected, the experimental data falls in between the two numerical limits (Fig. 17). However, more interestingly is that the experimental data trends more closely to the upper no-slip frictional bound, both in terms of *fRe* values and overall behavior with increasing *Re*. The *fRe* vs. *Re* graph behavior also suggests two major regions of interest – the lower *Re* region (2 – 10) where the *fRe* drops drastically with increasing *Re*, and the moderate *Re* region (10 – 25) where the *fRe* levels off and becomes insensitive to *Re*. These trends are consistent among all the different micro-trench configurations (Fig. 15), and will be discussed in more detail in the following two sections.

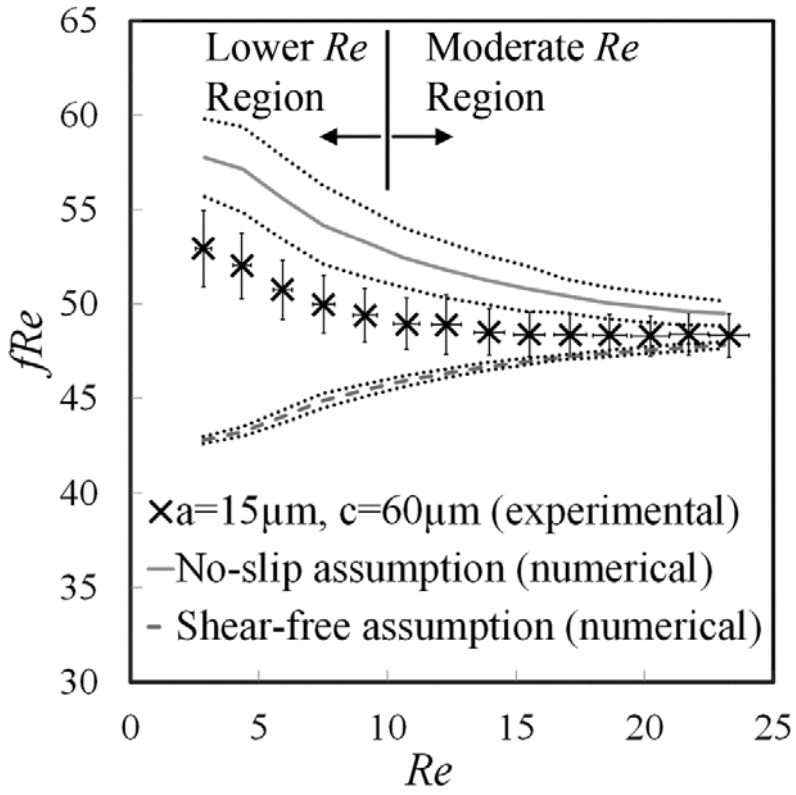

Figure 17. *fRe* vs *Re* graph for experimental and numerical results for a micro-trenched microchannel (*a*= 15µm, *b*= 65µm, *c*= 60µm). As expected, the experimental results are located between the two bounding numerical *fRe* limits. The standard deviation of the numerical results is plotted as dotted lines above and under the averaged values. Since different microchannels were used for each trial, their wetting characteristics varied slightly between samples leading to a maximum of 3% of the average value.

2.4.3 Low *Re* - Pinching Effects

In the lower *Re* region (<10), a large portion of the micro-trenches are de-wetted. Also from Fig. 15, it was observed that the friction increased with decreasing *Re*.

Recalling from the previous discussion that the air-water interface seems to behave closer to a no-slip boundary condition, the increase in hydrodynamic resistance in the lower *Re* region may be attributed to the reduction in flow area due to pinching effects. As most of or a significant number of the micro-trenches are de-wetted in the lower *Re* region, the water flow over the trenches is significantly pinched throughout the extent of the microchannel if the inlet pressure is not large enough (Fig. 18).

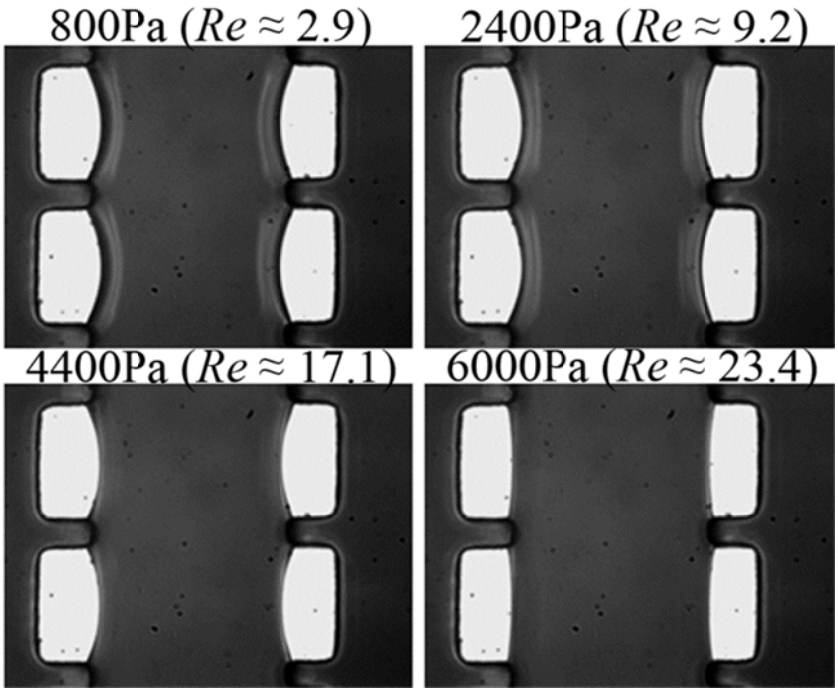

Figure 18. Micrograph (*M*= 40×, *NA*= 0.60) representing pinching effects in a micro-trench section (*a*= 15µm, *b*= 65µm, *c*= 30µm) located at 70% from upstream. It is observed that the air layer expands more into the water layer if the inlet pressure (and hence *Re*) is reduced.

The pinching effects can also be inferred from Fig. 19, where the trend of the $fRe_{experimental}$ agrees closer to the $fRe_{numerical,no\text{-}slip}$ than the $fRe_{numerical,shear\text{-}free}$. One reason why the trend of $fRe_{numerical,shear\text{-}free}$ is different from $fRe_{experimental}$ and $fRe_{numerical,no\text{-}slip}$ is because the viscous losses in this shear-free interface arrangement are primarily dominated by the water in contact with the non-textured surfaces at the top and bottom walls of the microchannel. Since there is no viscous dissipation at the left and right sides of the water layer in the micro-trench regions (where the air-water interface is located), the friction of the water layer will decrease if the microchannel is strongly de-wetted and water contact with the top/bottom walls is reduced. Unless the flow area is greatly reduced over de-wetted microtextures,[30-31] the pinching effects mentioned here suggest that the air-water interface is closer to a no-slip boundary condition and that the microchannel friction is sensitive to even small reductions in the cross-sectional flow area for the reasons mentioned above.

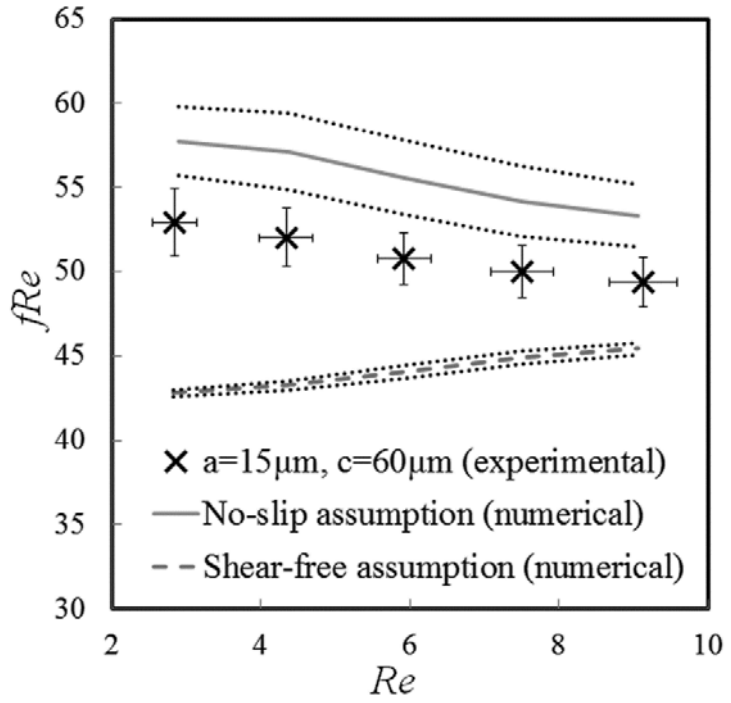

Figure 19. (Fig. 16 revisited). Comparison of $fRe_{experimental}$ and the two bounding $fRe_{effective}$ limits (numerical) in the low *Re* region. The difference between the $fRe_{experimental}$ and the numerical $fRe_{numerical,no\text{-}slip}$ bounds are 7.4% – 8.3% if the air-water interface is assumed as a solid wall (upper bound) and 8.8% – 23.6% if the interface is assumed as a shear-free layer (lower bound).

One possible explanation why the air-water interface behaves closer to a solid wall may be due to contamination of the air-water interface. Studies have shown that even slight contaminations of surfactants may result in a solid wall-like behavior of the air-water interface, and it has been an extremely difficult process to maintain the system with no contamination.[32] Even with the use of distilled water, it is possible to incur interface contamination from the microchannel surface, external tubing and/or connectors.

Recalling Figure 15, the immobilized nature of the air-water interface may be the reason why the micro-trench configurations with similar solid fractions ϕ_S exhibit similar frictional characteristics regardless of the micro-trench depth.

Consequently, the important parameter in controlling the air layer size is the Laplace pressure $\Delta P = \frac{\gamma}{\Re}$. If the air pressure overcomes the Laplace pressure, where the maximum required pressure is the trench gap size, the air layer will protrude into the water layer thus pinching the flow. While the role of Laplace pressure has been previously explored[29, 31], it can be further deduced that having a large micro-trench gap does not necessarily favor over smaller micro-trench gaps, particularly due to the risk of lowering the maximum Laplace pressure and experiencing significant pinching effects even to a mild degree. Based on the aforementioned analogy, the Laplace pressure is an important design parameter not only to calculate the flooding pressure, but also to track the effective cross-sectional flow area for cases where the micro-trench gaps are considerably large.

2.4.4 Moderate *Re* – Insensitivity between Friction and *Re*

An interesting aspect in the moderate *Re* region (10 – 25) is the fact that *fRe* becomes rather insensitive to *Re* and therefore insensitive to pressure and degree of micro-trench wetting/penetration. In order to understand the significance of this phenomenon, the wetting characteristics of the micro-trenches are explored first (Fig. 20). In the figure, the wetting of the trenches generally start at 1200Pa inlet pressure, which corresponds to *Re*= 4.3 – 4.6 for *a*= 15μm trenches and *Re*= 3.6 – 3.9 for *a*= 55μm trenches. Since the inlet pressures are well above the capillary pressure in the moderate *Re* region, majority of the

micro-trenches are wetted in this region. However, the global wetting degree of each micro-trench configurations does not significantly affect the microchannel friction.

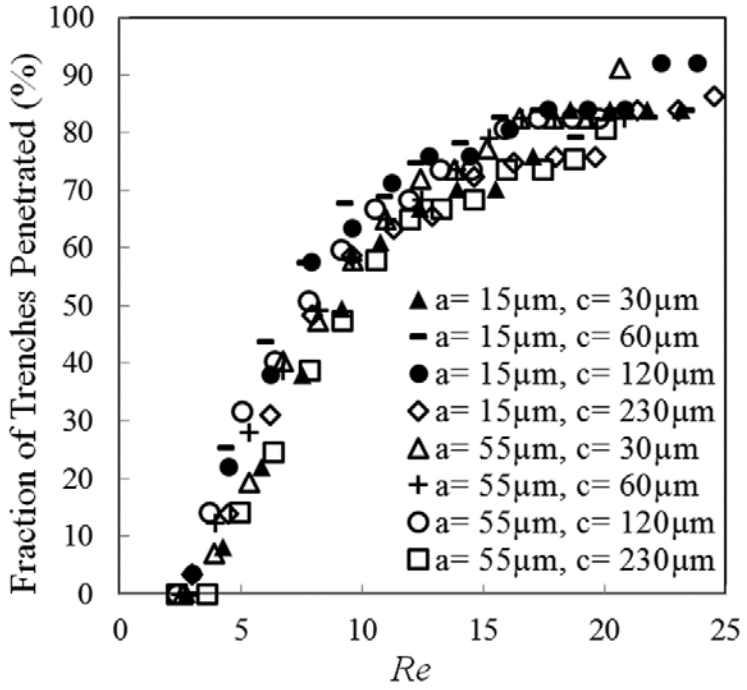

Figure 20. Fraction of trenches penetrated vs. *Re* for a single microchannel sample (left side of the trenches only). In the higher *Re* (or ΔP) range, the wetting of the trenches no longer increases significantly. The wetting percentage does not necessarily infer that the trenches are fully wetted but can also be partially wetted: it merely indicates the percentage of trenches where the liquid layer has overcome the Laplace pressure.

This insensitiveness of the microchannel friction to wetting effects is further analyzed by tracking the magnitude of the water penetration into the micro-trenches. In

Fig. 21, the shallowest micro-trench configuration (a= 15μm) demonstrates a binary behavior when transitioning from a non-wetting state to a fully-wetting state. As the micro-trench depth increases, the transition becomes progressively smoother. Nonetheless, the wetting behaviors of different micro-trench configurations do not seem to significantly affect the microchannel friction.

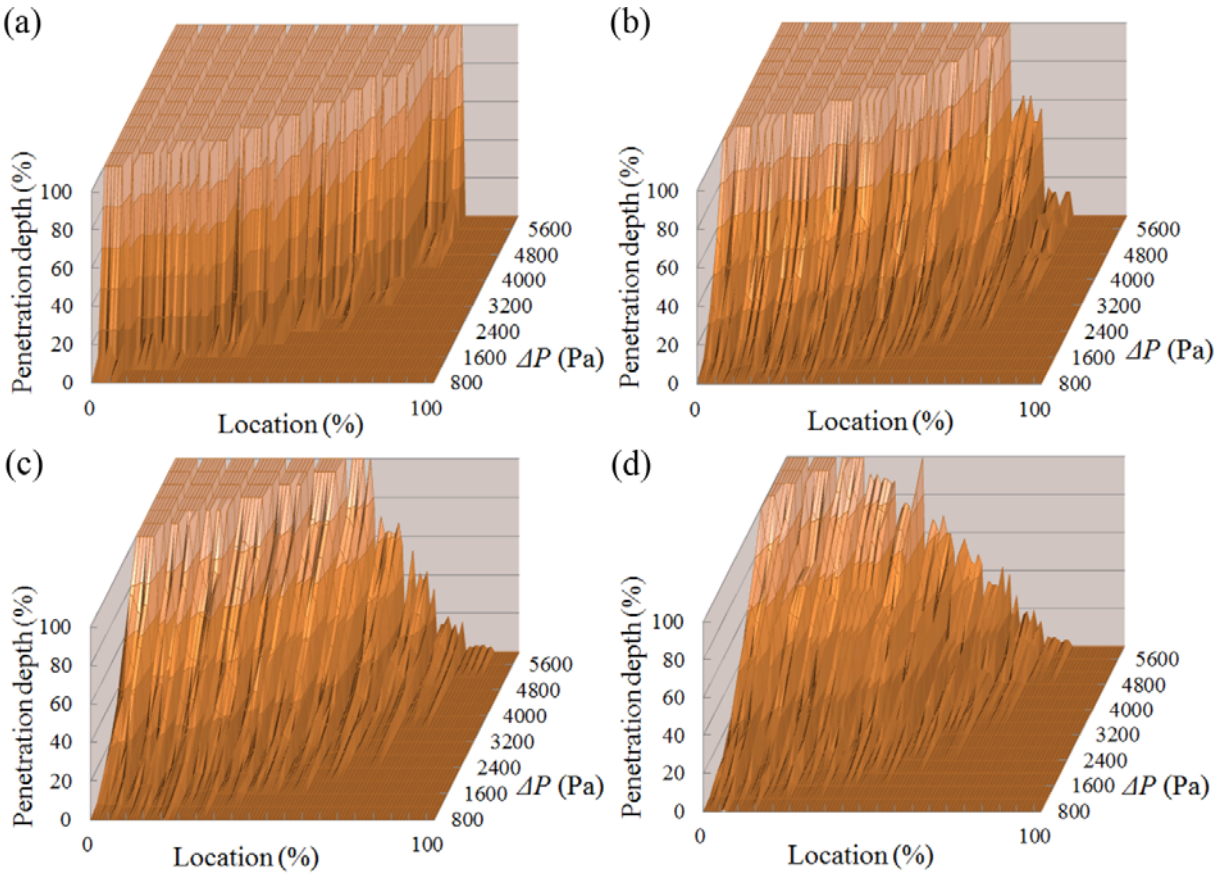

Figure 21. Penetration of water layer into the trenches (%) as a function of inlet pressure and location in the microchannel for a= 15μm configurations (left side of the trenches for

a single experiment). The micro-trench depth c varies from (a) 30μm, (b) 60μm, (c) 120μm to (d) 230μm. In the Penetration depth (%) axis, 0% represents a de-wetted state while 100% represents a fully wetted state of the micro-trench. Comparing between different micro-trench depths, the shallower trenches have a greater number of fully wetted trenches than the deeper ones. The trend for a= 55μm is similar to the data presented here.

In Fig. 22, the $fRe_{experimental}$ is compared with the numerical friction bounds for a= 15μm, c= 60μm trenched microchannel. Unlike in the lower Re region, the upper and lower bounds converge close to the experimental data as the Re increases. This is expected because both $fRe_{numerical}$ bounds reflect the actual w_{eff} data, where a large fraction of micro-trenches is fully wetted (corresponding to the upper flat surface in Fig. 21) while the number of de-wetted micro-trenches is greatly reduced in the moderate Re region.

One possible explanation for the insensitiveness of the microchannel friction to Re is the limitation on how much the streamlines can bend into the penetrated trenches since the flow is Re>1. Unless Re<<1, the effective width is not likely to increase with pressure once the air-water interface penetrates beyond a certain distance into the trenches. The limitation on how much the streamline can deflect into the micro-trenches can be observed from numerical simulations of a fully wetted micro-trench case.

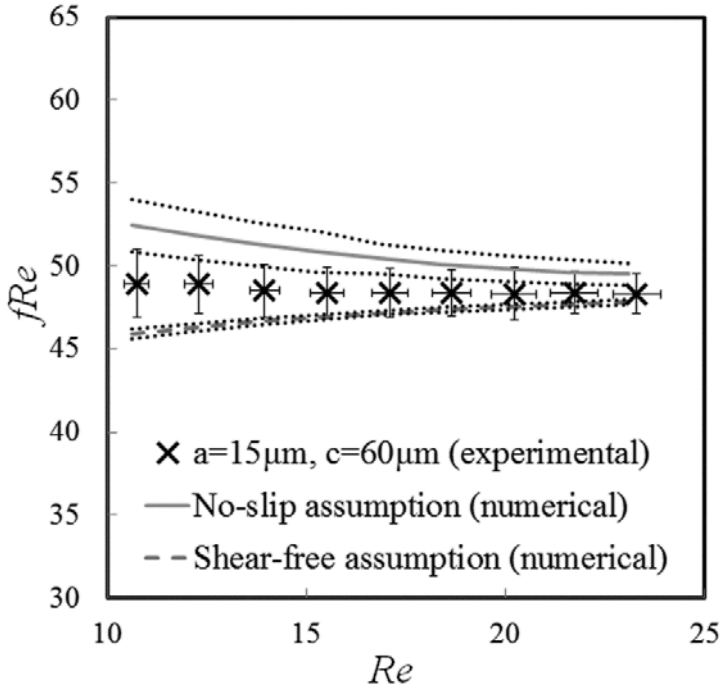

Figure 22. (Fig. 16 revisited). Comparison of $fRe_{experimental}$ and the numerical $fRe_{numerical,\ no\text{-}slip}$ limit in the moderate *Re* region. In this *Re* region the friction of the microchannel is essentially constant. Considering the fact that a significant amount of trenches are wetted beyond these *Re* ranges, the degree of the trenches do not seem to affect the microchannel friction.

The fully wetted case was selected since it will provide the maximum possible deflection of the streamlines into the trenches, at least for the geometries tested in this experiment. In Fig. 23, the magnitude of the deflection decreases with increasing *Re*, since the separated flow is able to carry more energy towards the other end of the trench. The average deflection of the streamline was calculated to be 10 – 14μm into the micro-trenches, which is much smaller than the total depth of the micro-trench. The limitations

on how much the streamlines can bend infers that the microchannel friction is less likely to be affected by *Re* (and hence ΔP) once the water penetrates beyond a certain distance into the micro-trenches.

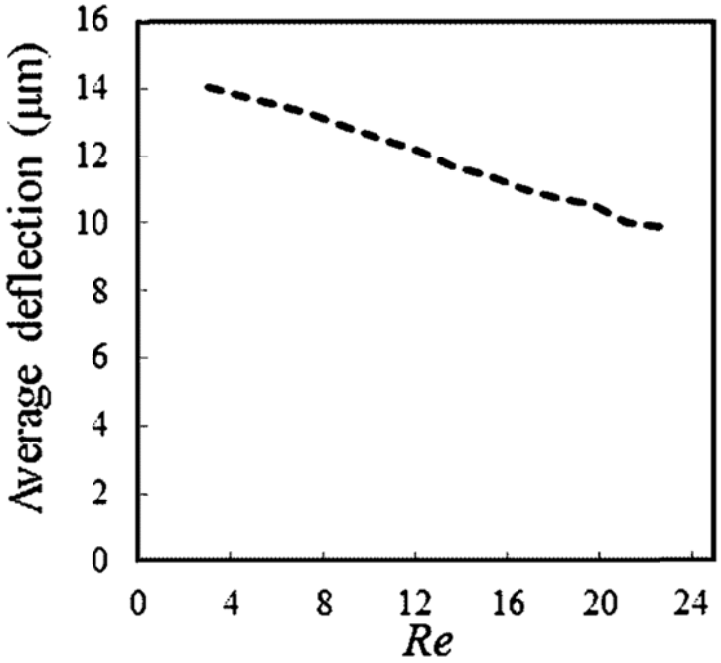

Figure 23. Numerical result of the streamline bending into a fully wet micro-trench element. For the *Re* tested here, the maximum deflection of the streamline is less than 30% of the micro-trench depth. As *Re* increases, the streamline tends to deflect less into the micro-trench.

Fig. 24 shows more COMSOL results on pathline of the particles released at the beginning of the microtrench to demonstrate how much the streamlines can deflect depending on the flow *Re*.

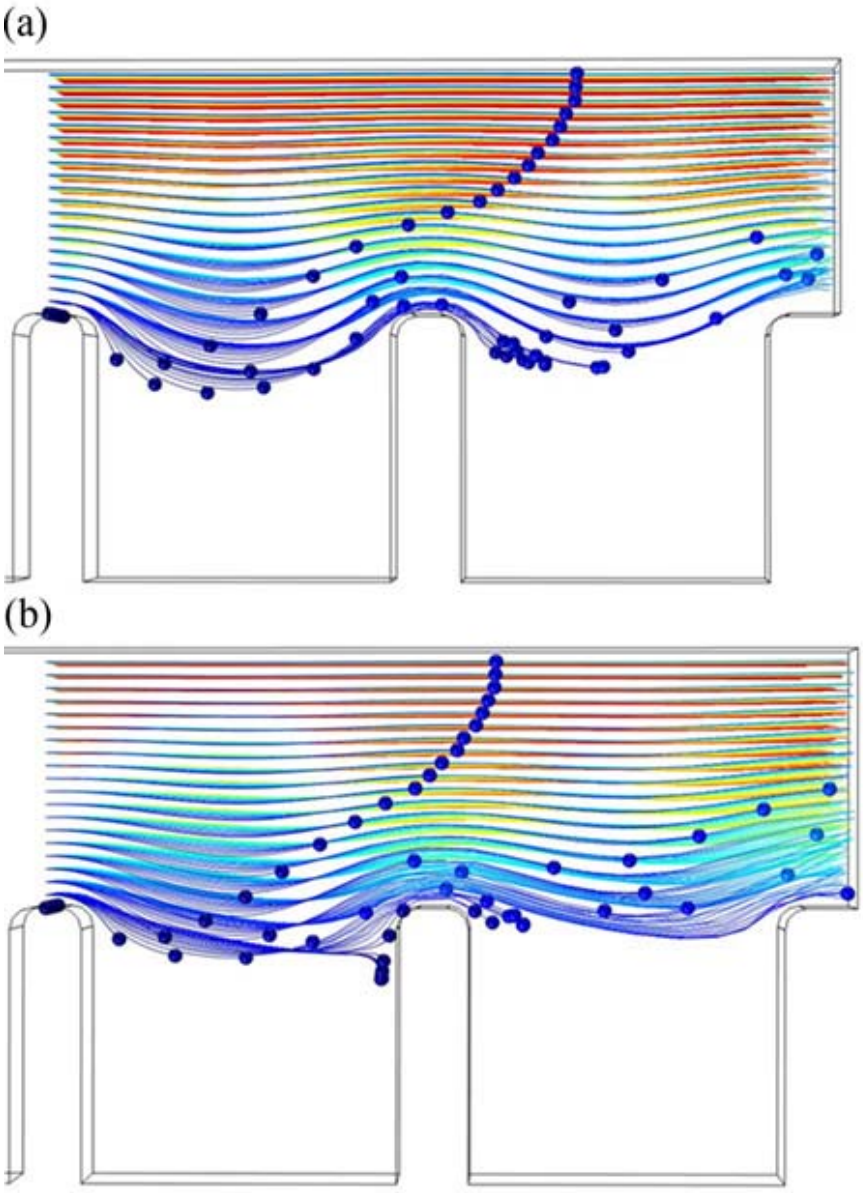

Figure 24. Numerical results on pathlines or streamlines of flow under (a) $Re \approx 2$ and (b) $Re \approx 23$. It can be observed that the streamline deflects more into the micro-trenches if the Re is lower.

While the results in the lower and moderate *Re* region point out interesting aspects of partial penetration effects on the microchannel friction, attention should be paid to the fact that the microtexture geometry used in this experiment is not ideally the most efficient design to achieve friction reduction (the micro-trenches are aligned transverse to the flow and the air-water interface is constrained by the finite gap size). However, it does provide intuition that the air-water interface in the micro-trenches may not be simply regarded as a shear-free layer and that the frictional characteristics may actually be unaffected by the wetting degree of the micro-trenches.

2.4.5 Comparison between fully wetted and initially de-wetted case

In order to further explore and validate the *fRe* behavior, the *fRe* was compared for microchannels with initially de-wetted micro-trenches and pre-wetted micro-trenches. For the pre-wetted micro-trench case, the microchannel was pressurized at ~12kPa until all the micro-trenches were fully wet. Once the micro-trenches were confirmed to be fully wetted, the experiments were performed from Re= 2.9 to Re= 22.1 corresponding to ΔP= 800Pa and 6000Pa, respectively.

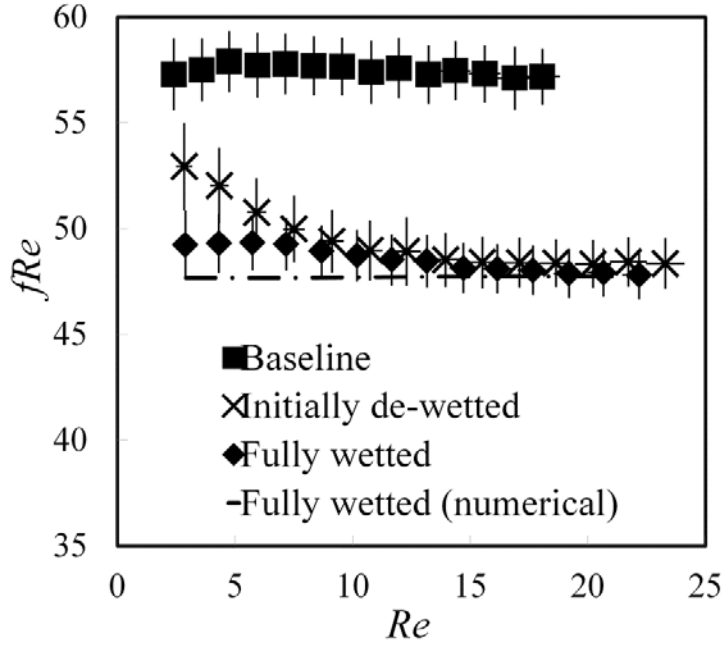

Figure 25. Comparison of friction in a microchannel between Cassie-Baxter state and Wenzel state (a= 15μm, b= 65μm, c= 60μm). For the numerical fRe calculations, a rectangular cross-sectional area is assumed since the error in fRe due to the difference between the trapezoidal microchannel geometry (measured) and the rectangular cross-section is < 0.5%.

Figure 25 compares the fRe values for microchannels which are initially under the Cassie-Baxter state (de-wetted micro-trenches), and microchannels under the Wenzel state (pre-wetted micro-trenches), alongside numerical simulations results for the latter. The fRe for the fully-wetted microchannels are generally less sensitive to Re, both experimentally and numerically, whereas the initially de-wetted microchannels started at a considerably high fRe value but then converge closely to the fully wetted micro-trenches values as the interface penetration became substantial at Re> 7. This suggests

that for $Re < 7$, the majority of the micro-trenches are de-wetted, and the pinching effects result in a considerably higher friction than the fully wetted microchannels. As mentioned in Section 2.4.2, surfactant contamination may immobilize the air-water interface leading to an increased friction at the air-water interface as a significant number of de-wetted micro-trenches are pinching at $Re < 7$. For the fully wetted micro-trenches, on the other hand, the water molecules may freely bend into the micro-trench gaps, thus increasing the effective flow area. This increase in effective flow area leads to a larger friction reduction effect than the water flow over the immobile air-water interface. Regardless of the wetting mode, it should be noted that a substantial friction reduction is achieved for both wetting and de-wetting micro-trenches compared to the baseline microchannel with no micro features.

2.5 Conclusion

In this chapter, the friction reduction characteristics of the microtextured superhydrophobic surfaces have been extensively studied. Studies of flow over the Cassie-Baxter state was prevalently assumed as a shear-free region. In order to properly assess the effects of flow over isolated air pockets, friction was characterized from a de-wetted to fully wetted superhydrophobic microchannels. Micrographs of the air-water interface location were taken for each inlet pressure settings and the corresponding flow rates were measured, where the experiments were performed between $Re = 2 - 25$. The frictional characteristics of different wetting criterion were compared with numerical simulation of the upper and lower $fRe_{numerical}$ bounds, where the upper bound is solved by

assuming a no-slip boundary condition at the air-water interface and the lower bound is solved by assuming a shear-free boundary condition at the interface.

In the lower *Re* region (2 – 10), the *fRe* of the de-wetted microchannels increased significantly with decreasing *Re*. Although conventionally the air-water interface was approximated as a shear-free boundary condition, experiments and comparison with numerical results showed that the $fRe_{experimental}$ of the air-water interface behaved much closer to the $fRe_{numerical,no\text{-}slip}$, both in terms of magnitude and trend. The reason for this behavior may be attributed to a number of reasons: 1) immobilization of the air-water interface if there is contamination due to particulates or surfactants, and/or 2) pinning of the water molecules at the interface along with the small micro-trench gap size. Thus, if the *Re* was low enough (hence small ΔP) and the micro-trenches were sufficiently de-wetting, the microchannel friction was increased due to the air pockets pinching the main water flow section.

In the moderate *Re* region (10 – 25), the frictional characteristics of the microtextured microchannels became rather insensitive to how much the air-water interface was penetrating into the micro-trenches. Comparison with numerical results suggests that this insensitiveness is due to the limitation on how much the streamlines can bend into the micro-trenches. This agrees well with the penetration measurements that most of the micro-trenches are at least partially wetting for $Re > 10$. Since under these conditions, the streamlines deflect only by a small distance into the wetting micro-trenches throughout the entire microchannel, the effective flow area becomes constant and the microchannel *fRe* levels off as well.

The above two results were further compared with the Wenzel mode microchannels, where the micro-trenches were pre-wetted and no air pockets were present. Results showed that for Re >7 the friction of the initially de-wetted micro-trenches and the fully wetted micro-trenches converged together. However, for Re <7, the fully wetted micro-trenches clearly demonstrated a lower hydrodynamic resistance than the initially de-wetted micro-trenches. While the initially de-wetted micro-trenches experience pinching effects in the low Re, the streamlines in the fully wetted micro-trenches can freely bend (although by a finite distance) into the gaps, thus resulting in an increased effective flow area. This suggests that the microchannel under the Wenzel state may be more efficient in achieving friction reduction than the ones under the Cassie-Baxter state.

2.6 Achievements

- Journal paper - "Pressure and Partial Wetting Effects on Superhydrophobic Friction Reduction in Microchannel Flow", Kim, T.J., and Hidrovo, C. H., Physics of Fluids, Vol. 24, 2012
- Refereed conference proceeding - "Superhydrophobic Friction Reduction Microtextured Surfaces", Kim, T. J. and Hidrovo, C. H., 2nd ASME Micro/Nanoscale Heat & Mass Transfer International Conference, Shanghai, China, December 18-21, 2009.

CHAPTER 3

MAINTAINING STABILITY OF SUPERHYDROPHOBIC MICROCHANNEL WALLS THROUGH HEATING

3.1 Introduction

In the previous chapter, the relation of the microchannel friction between superhydrophobic microchannel and the baseline microchannel (smooth wall) has been investigated based on the hydrodynamic resistance measurements and simulation results. Comparison of the microchannel friction between experimental results and numerical results suggested that the air-water interface in the superhydrophobic microchannel behaves closer to a no-slip boundary condition. When the pressure drop is low enough the air pockets protrude into the microchannel, thus pinching the flow and increasing the effective hydrodynamic resistance. In this section, the magnitude of the pinching is controlled by heating the microchannel, and the corresponding flow rate is tracked by taking micrographs of the micro-textured regions.

While studies have been previously performed to observe friction and drag reduction over superhydrophobic surfaces,[1, 8] there is very little work aimed at correlating the pressure and thermal effects on the stability and characteristics of this condition. A few researchers have studied the pressure effects on the Cassie-Baxter State, concluding that textured surfaces with isolated gaps result in a lower contact angle hysteresis [33]. However, studies on thermal effects to the trapped gas layer and correlating them to superhydrophobic channel flows have not been as rigorously conducted.

In this section, PDMS (Polydimethylsiloxane) microchannels were fabricated using soft lithography techniques. The roughness of the microchannel wall was large enough to induce the Cassie-Baxter state, where the water layer rested on top of a textured surface with air pockets trapped underneath the liquid layer. Flow rates were measured by varying the average temperature taken at the microchannel inlet and outlet. Similar to Chapter 2, results showed that the air pockets in the micro-texture started to flood as the inlet pressure was increased. However, as the microfluidic channel was heated, the air in the micro-gaps expanded and the penetrating water layer was pushed back to its original state. Consequently, the air gaps can withstand higher liquid pressure, thus prolonging the two phase flow in the microfluidic channel. The results observed in this section indicate that heating the cavities will provide more stability to the Cassie-Baxter state and maintain the partial two-phase flow under elevated pressures.

3.2 Background

3.2.1 Cassie-Baxter Model

This chapter focuses primarily on maintaining the air pockets under elevated pressures in a Poiseuille flow with rough walls. Thus achieving a stable Cassie-Baxter state is of major interest as this ensures a partial two phase flow and consequently leads to friction reduction in the microchannel flow. To reiterate the Cassie state, it is defined as a state where a liquid meniscus resting on top of a textured surface does not wet the gaps beneath the liquid interface. As a result the liquid resting on top of the textured surface will experience a reduction in friction since a portion of the contact surface

underneath is consisted of gas. As mentioned in Chapter 2, the conventionally used Cassie-Baxter model[34] is,

$$\cos\theta_{CB} = \phi_s \cos\theta_Y - (1-\phi_s) \tag{7}$$

where θ_{CB} is the Cassie-Baxter angle, θ_Y is the Young's contact angle, and ϕ_s is the ratio of solid contact area to the nominal area. Also, in order to ensure the stability of the Cassie-Baxter state, the roughness of the surface texture must be larger than the critical roughness factor [33, 35],

$$r_c = \phi_s - \frac{1-\phi_s}{\cos\theta_Y} \tag{16}$$

where r_c is the critical roughness factor. A roughness factor lower than r_c will result in a stable Wenzel state where there are full interstitial wetting of the microtextured surface, or a metastable Cassie-Baxter state where the liquid initially under the Cassie-Baxter state but may transition to Wenzel state if disturbance is applied. On the other hand, a roughness factor higher than r_c will likely to lead to a stable Cassie state. As will be mentioned in the later section, tests were performed on micro-textured microfluidic channels with roughness factors higher and lower than the critical roughness factor.

3.3 Experimental Setup

3.3.1 Fabrication of Microchannels

To prepare the microchannels, a bare silicon wafer was spin coated with Su-8 2050 negative photoresist (Microchem) where the replicating mold for the PDMS microfluidic channels layouts were created through photolithographic procedures. The wafer was then silanized (UCT specialties, LLC) for at least an hour in a vacuum desiccator to fluorinate the Su-8 replicating mold. This procedure will prevent the cured PDMS from prematurely bonding and damaging the Su-8 mold. A PDMS base and solvent (Dow Corning) mixture, with a volume ratio of 10:1, was poured onto the mold and cured at 95°C for 2 hours. The cured PDMS with microfeatures was then peeled off the mold and sliced into individual slabs. A complimentary set of PDMS slabs without microfeatures were fabricated and bonded to the featured PDMS slabs using an oxygen plasma cleaner (Harrick Plasma) at 29 Watts for 20 seconds.

The channel dimension for the baseline channel with no surface textures is W= 100μm, H= 110μm, L= 2cm. For the micro-textured microchannels, the liquid flow channel dimension is identical to the baseline channel while an array of micro-trenches with dimensions of a= 20μm, b= 60μm, c= 500um on the side walls are added.

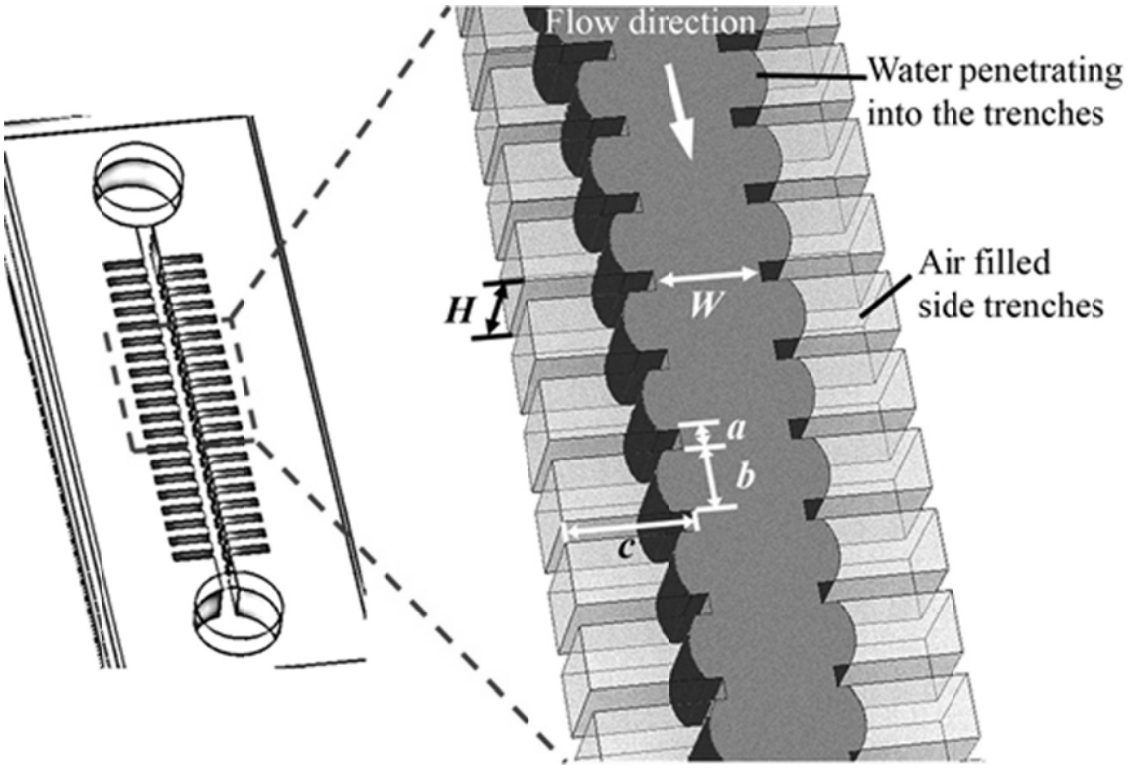

Figure 26. Schematic diagram of the micro-trenched microchannel. The nomenclatures of the microchannel is indicated in the figure.

3.3.2 Differential Pressure Setup

A water reservoir with a controllable column height was used to generate a constant pressure source (Fig. 27), where the water column outlet was connected to the microchannel inlet. By controlling the height of the water column, constant pressure conditions of 2500Pa, 3500Pa, and 4500Pa were applied to the microfludic channel. A pressure transducer was used to measure the gauge water pressure supplied to the channel.

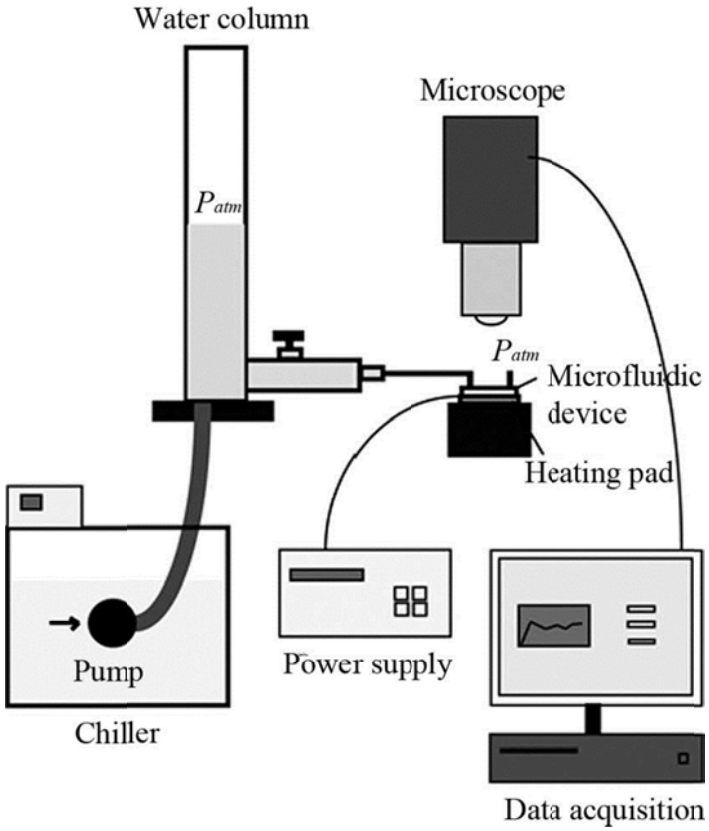

Figure 27. Schematic diagram of the experimental setup. A joule heating pad connected to a power supply is placed underneath the microchannel.

3.3.2 Heating of the Microfluidic Channel

A resistive heating pad was placed underneath the microfluidic device, and power was supplied to the heating pad (Minco) with a power supply (E3647A, Agilent) to provide a constant heat flux to the channel. The power supplied through the joule heaters was controlled by varying the voltage to the heating pad and the corresponding current was measured.

The temperature was measured by embedding two T-type thermocouples at the microchannel inlet and outlet. Under a fixed pressure head, the air-water interface was initially observed under room temperature conditions, where a CCD camera (Coolsnap, Photometric) was used to acquire the microchannel images. The temperature of the bottom substrate was then increased from 26°C to 32°C, with increments of 1°C. Measurements were performed with a microscope after the substrate temperature reached equilibrium.

3.4 Results

3.4.1 Flow Pinching Due to Heating

Water was driven in the microchannel by controlling the height of the water level in the constant pressure head column connected to the microchannel inlet. Depending on the inlet pressure, the pressure will either be in a Cassie-Baxter state with the air pockets intact or transition to the Wenzel state if the pressure overcomes the Laplace pressure in the micro-trench. Since the maximum pressure required to prevent penetration into the micro-trenches is calculated to be 1000Pa, the inlet pressures were large enough (2500Pa, 3500Pa and 4500Pa) to induce penetration starting from the inlet region (Fig. 28).

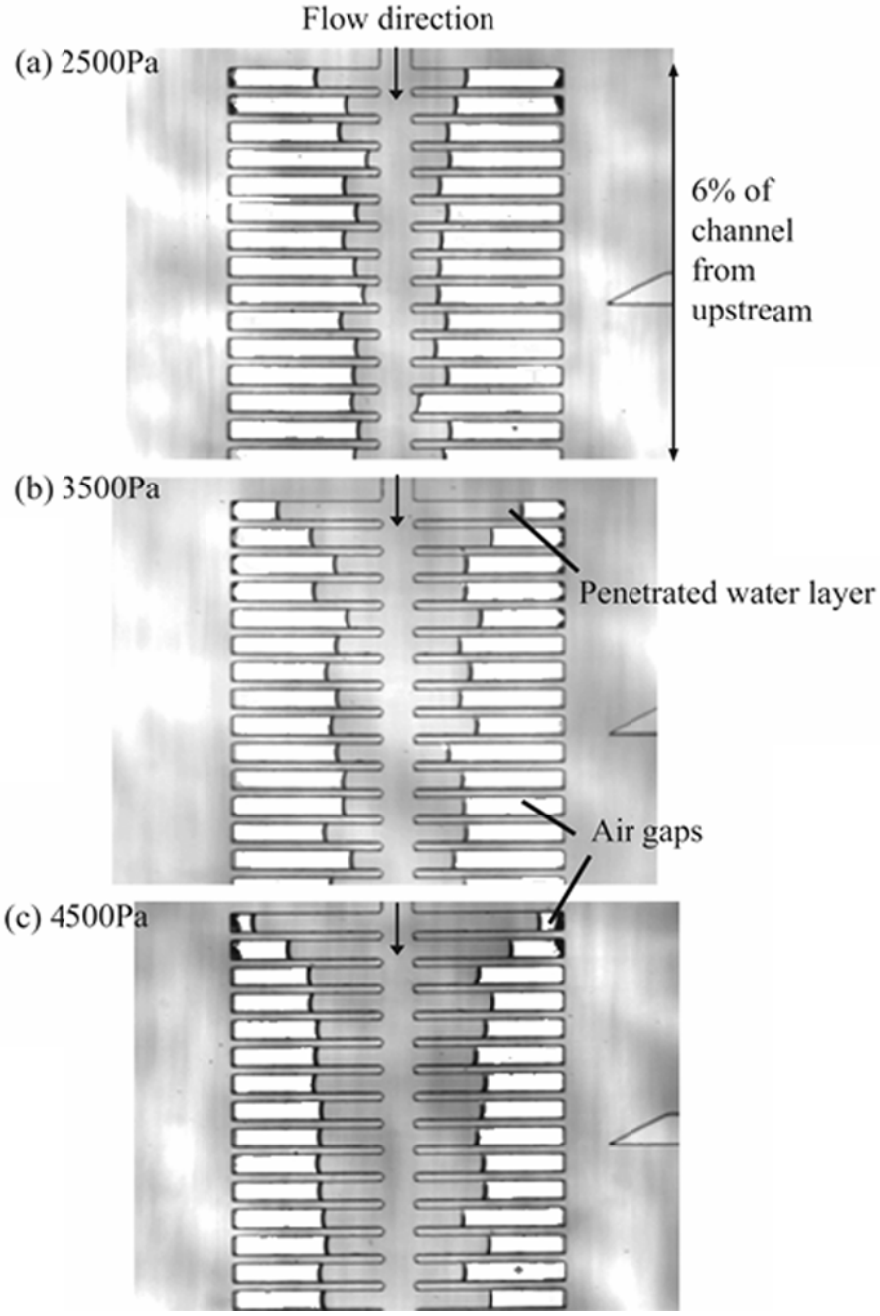

Figure 28. Micrographs of b= 60μm, c= 500μm trenched channel under (a) 2500Pa, (b) 3500Pa, and (c) 4500Pa at 25℃. Penetration of the water layer into the microcavities can be observed near the inlet. The images were taken with a 5x objective lens

However, as soon as heat was applied to the microchannel, changes in the air pockets were immediately noticeable. When the substrate temperature was at 28°C, the curvature of the penetrating air-water interface was convex (curved outwards), indicating that the liquid pressure was greater than the pressure of the air pockets. As the substrate temperature was increased to 30°C (Fig. 29), the curvature gradually flattened out, indicating that the liquid pressure and the heated air pocket pressure have balanced out. However, as the temperature was further increased to 32°C, the curvature was reversed to a concave profile (interface curved inwards towards the main water channel). Once the curvature was reversed, it became apparent that the air pocket pressure was significantly increased as the air-water interface started to retract back to its original position.

In the inlet, where the pressure is higher and the water penetration more apparent, it was observed that the air-water interface in the wetting micro-trenches were reverted back to the de-wetted case under elevated temperatures. However, in the outlet, where the pressure is closer to atmospheric conditions and the air pockets remained de-wetted, the heating of the micro-trenches led the air pockets to grow from the de-wetted state. The air pockets near the outlet started to invade into the main water channel, significantly pinching the flow (Fig. 30).

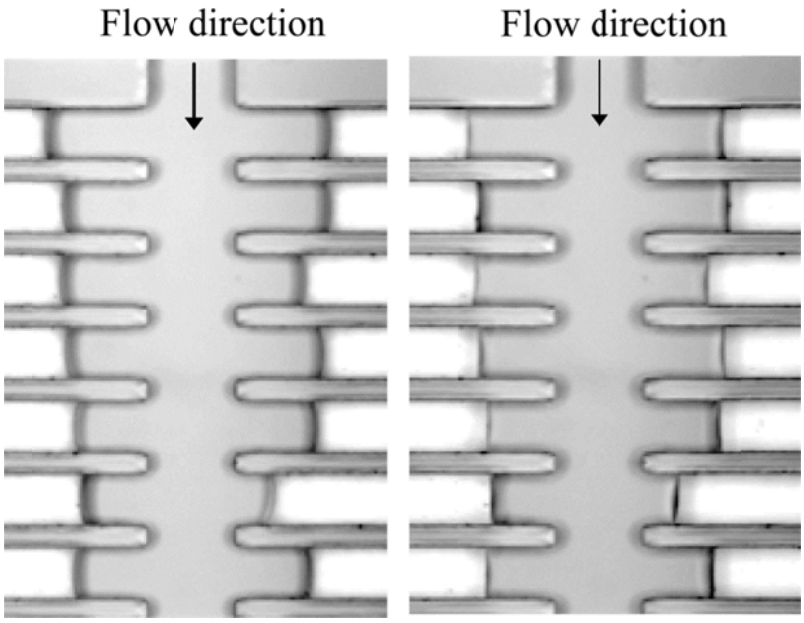

Figure 29. Micrographs of heating effects on liquid penetration near the microchannel inlet at (a) 30℃ and (b) 32℃. The inlet pressure here is at 2400Pa (gage).

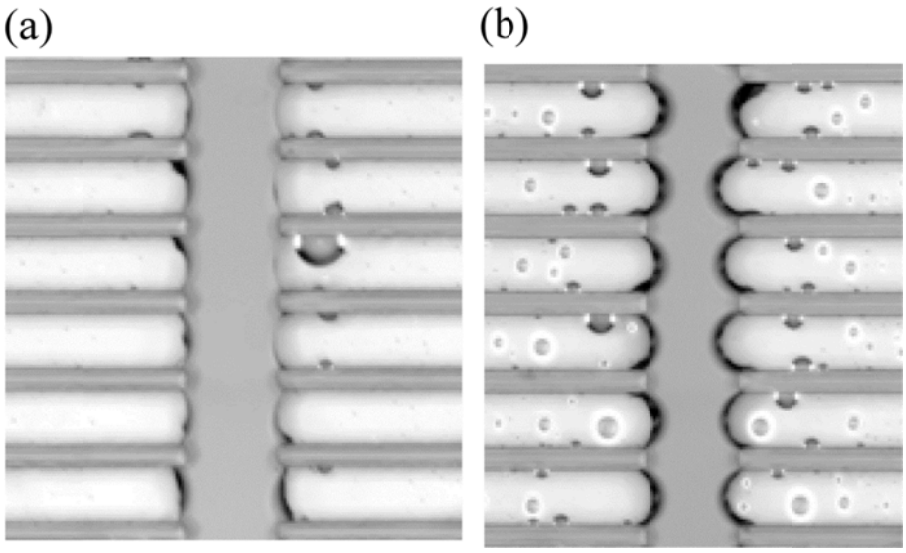

Figure 30. Micrographs of heating effects on liquid penetration near the microchannel outlet at (a) 30℃ and (b) 32℃. The inlet pressure here is at 2400Pa (gage).

The penetration depth as a function of channel location under different temperature conditions is further presented in Fig. 31. From the graph, it is apparent that the penetration depth along the channel decreases as the temperature is increased. The negative penetration depth represents the invasion of air pockets into the main water channel.

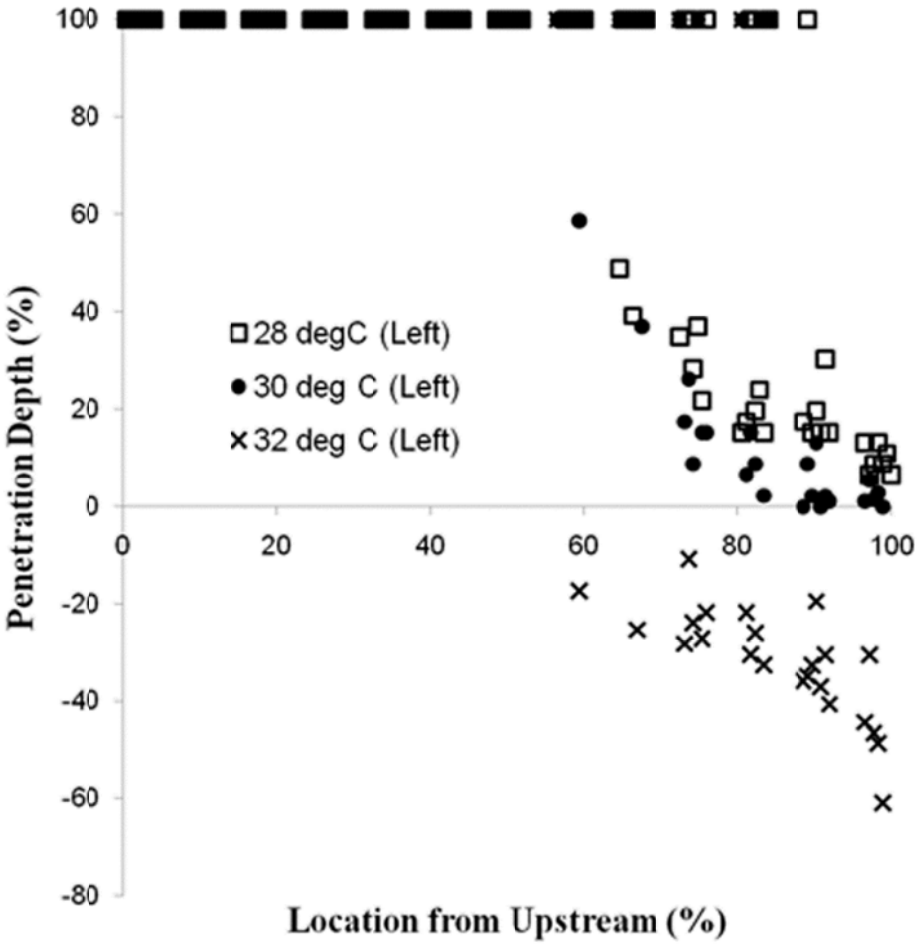

Figure 31. Penetration depth vs. location under different substrate temperature conditions for inlet pressure at 3200Pa (gage). The y-axis is normalized, where 100% represents that

the air pockets are fully wetted and -100% represents that the water layer is completely cut off due to excessive pinching.

In the figure, the inlet pressure is 3200Pa, which is approximately 2200Pa higher than the Laplace pressure. In this experiment, all of the micro-trenches along the microchannel were experience some degree of wetting at 28°C, where approximately 60% of the micro-trenches were fully wetted. As the temperature was increased to 30°C, a shift in the penetration depth can be observed due to the expansion of air pockets, where approximately 10% of the microchannel showed that the liquid layer retracted back to the non-penetrating state. When the temperature was further increased to 32°C, the remainder of the air pockets transitioned to a fully non-wetted state. However, the air pockets continued to grow and eventually invaded the main water layer, and the flow was significantly pinched. While the air pockets are controllable with temperature, it is to be noted that the fully wetted cavities throughout 60% of the channel remain fully wetted.

3.4.2 Pinching Effects and the Consequential Reduction in Flow Rate

Once the temperature inside the microchannel was greater than a certain threshold, the air pockets in the cavities continued to grow and the liquid flow started to experience significant pinching effects. Since pinching effects represent a reduction in the flow cross-sectional area, this is analogous to a closing valve. The pinching effects are more severe if the inlet pressure is lower, since even a slight increase in temperature resulted in a large reduction in flow rate until the flow was disrupted. For higher inlet pressures, the pressure of the water layer was able to balance the heated air pressure, and the flow rate

maintained at higher temperatures. However, once the temperature reached beyond a certain threshold, the air pockets started to grow again until a drastic drop in flow rate was observed.

The effects of pinching on the hydrodynamic resistance can be observed from the flow rate measurements. Figure 32 compares the flow rate vs. temperature between a smooth microchannel wall (baseline) and a micro-textured microchannel. As seen in Fig. 32(a), the flow rate of the baseline increases with temperature due to the reduction in the water viscosity. This is also true for the microchanel with micro-trenches in Fig. 32(b). Additionally, the flow rates of the micro-trenched microchannels are generally higher than the baseline microchannels under the same inlet pressure conditions, indicating a reduced friction from the air-pockets. However, the micro-trenched microchannels were very sensitive to the changes in temperature, particularly for the lower inlet pressure case where the air pockets expanded even under a slight increase in temperature. It was observed that the liquid flow was disrupted at a substrate temperature of 28°C. At higher inlet pressures, the flow rate became less sensitive to temperature, and the flow rate for all temperature converged to a similar slope.

The above results indicate that increasing the temperature of the microchannels and the air pockets was not always beneficial to the flow. Excessive heating did not reduce the friction in the channel but in fact, was detrimental to the flow. Thus, caution should be taken since excessive heating may pinch the flow and consequently increase the hydrodynamic resistance in the microchannel.

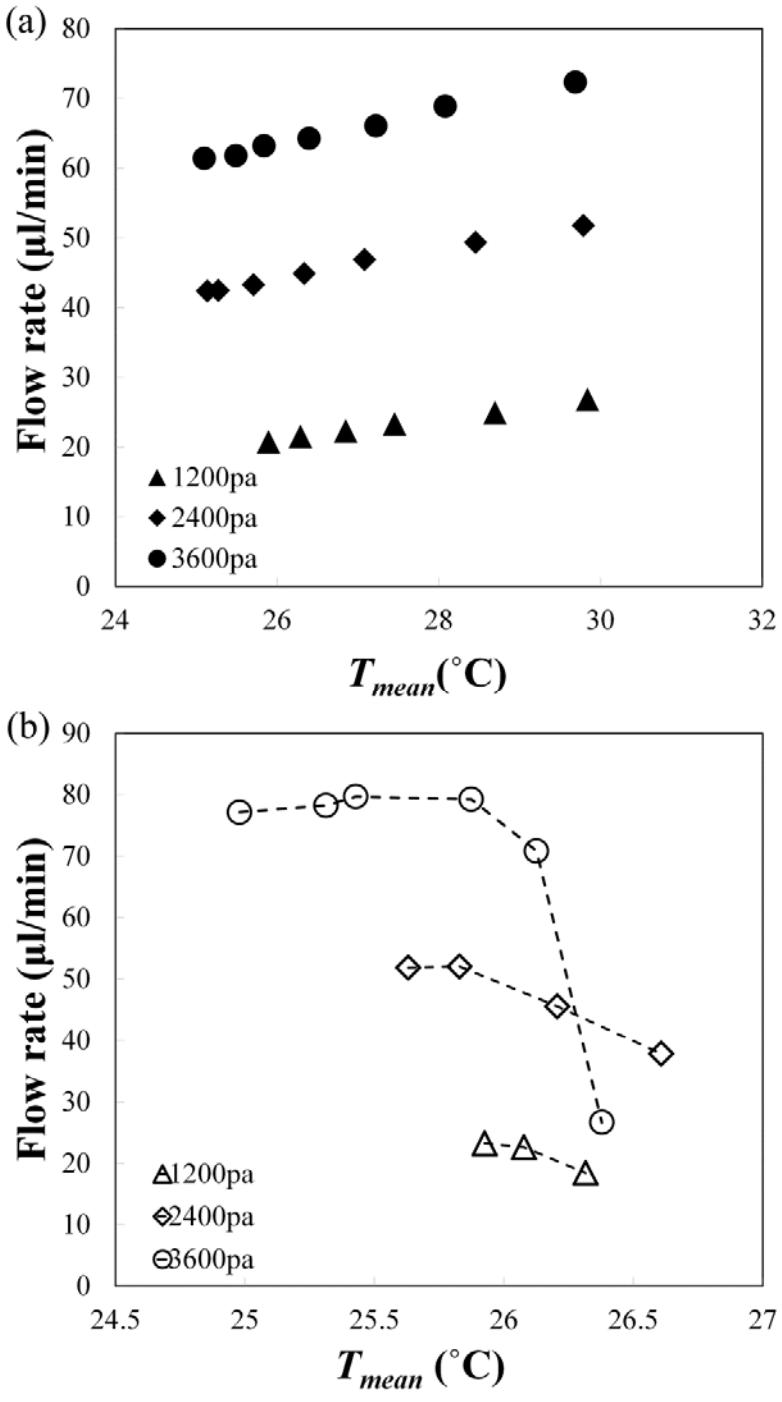

Figure 32. Flow rate vs. average temperature of (a) baseline microchannel and (b) trenched microchannel.

3.4.3 Additional Stability Issues during Initial Wetting of the Microchannel

A separate experiment has been performed to study the stability of the air pockets during the initial wetting phase. In this section, micro-trenches with different trench dimensions, and hence different roughness factors, are used to study the stability of the air pockets during the initial microchannel wetting phase. While introducing water into the microchannel, it was observed that shallower micro-trenches had a higher tendency to prematurely wet the micro-trenches.

One possibility for this premature wetting may be addressed to the stability criterion of the Cassie-Baxter state mentioned in Section 3.2.1. According to Eq. (16), three possible regimes are suggested - the Wenzel regime, the stable Cassie-Baxter regime, and the metastable Cassie-Baxter regime. If the actual roughness factor $r = 1 + 2c/(a+b)$ is greater than the critical roughness factor r_c, the liquid will be in the energetically stable Cassie-Baxter regime.

A number of different micro-trench configurations were tested and is listed in Table 3. The table also lists the corresponding critical roughness factor, solid fraction (assuming a flat air-water interface shape underneath the water layer) and the actual effective roughness factor. In the table, it can be seen that the microchannels with micro-trench dimensions of a= 15μm, c= 30μm and a= 55μm, c= 30μm have a considerably lower actual roughness factor than the critical roughness factor. It is likely that these two configurations will experience stability issues during the initial wetting phase, which is similar to imposing disturbances as the water jumps from one micro-trench to another during the wetting phase.

Table 3. Comparison of the ϕ_S , r_c, and r_{actual} for different micro-trench configurations. When calculating the r_c, the contact angle is assumed to be between θ_Y = 110° and 115°[36]. The range in contact angle is attributed by the fact that pristine condition microchannels were used rather than microchannels treated with silanized walls.

Trench Dimension	ϕ_S	r_c	r_{actual}
a= 15μm, c= 30μm	0.19	2.1 – 2.6	1.66
a= 15μm, c= 60μm	0.19	2.1 – 2.6	2.45
a= 15μm, c= 120μm	0.19	2.1 – 2.6	3.92
a= 15μm, c= 230μm	0.19	2.1 – 2.6	6.94
a= 55μm, c= 30μm	0.45	1.8 – 2.1	1.45
a= 55μm, c= 60μm	0.45	1.8 – 2.1	1.98
a= 55μm, c= 120μm	0.45	1.8 – 2.1	2.98
a= 55μm, c= 230μm	0.45	1.8 – 2.1	4.99

For micro-trench depths of c= 60μm, 120μm and 230μm micro-trench depth channels, $r_{actual} > r_c$. As explained in Equation 13, these micro-trench configurations are likely to be in the energetically stable Cassie-Baxter state. However, for both a= 15μm, c= 30μm and a= 55μm, c= 30μm micro-trenches, $r_{actual} < r_c$. This indicates that two of the shallowest micro-trench configurations are in likely to be in a metastable Cassie-Baxter state and will transition to Wenzel state if a disturbance is applied. Table 4 represents the number of premature wetted trenches normalized by the total number of trenches. Since only a= 15μm, c= 30μm and a= 55μm, c= 30μm micro-trench configurations had micro-trenches flooded with water during the initial wetting phase, the

premature wetting ratio was omitted for the other micro-trench configurations. Moreover, the a= 15μm, c= 30μm micro-trench configuration with the lowest r_{actual} had the largest ratio of prematurely wetted micro-trenches.

Table 4. The ratio of prematurely wetted trenches to the total number of trenches for both left and right side trenches combined.

Trench Dimension (μm) Land × gap × depth	Premature wetting ratio of individual trials (%)				
a= 15μm, b= 65μm, c= 30μm	15	46	36	10	22
a= 55μm, b= 65μm, c= 30μm	0	2	2	0	2

Since premature wetting should be prevented, the results suggest that the micro-trench dimension should be designed so that $r_{actual} > r_c$ when designing superhydrophobic microchannels. However, Eq. (16) neglects any pressure effect, and the actual critical roughness is likely to be different. However, the relation studied here will provide a first degree approximation of the stability of the air-water interface and design parameter recommendations of the micro-texture roughness.

3.5 Conclusion

In this chapter we studied the heating effects of the air pockets trapped between the roughness elements in a microchannel flow, where the roughness elements on the side walls were shaped as micro-trenches.

A constant pressure source was used to flow water into the microfluidic channel and the flow rate was measured using a flow meter. While the flow rate of the microchannels with smooth walls increased with temperature due to the reduction in the viscosity, the flow rate of microchannels with micro-trenches were greater in magnitude since the water was experiencing slip at the wall. Moreover, the liquid-air interface in the heated channels was able to withstand higher pressure ranges than the unheated channels.

The penetrated liquid layer was pushed back by the expanding air pockets as the temperature was further increased, and a stable Cassie-Baxter state was achieved. However, if the temperature was increased to the point that the pressure difference between the air and the water layer was too great, the air pockets started invading the main water flow section until the flow was disrupted. While this chapter focused on understanding the heating effects on the microchannel hydrodynamic resistance, the next goal is to measure the convective heat transfer coefficient for flow in a superhydrophobic microchannel.

The next chapter will focus on developing methods to heat the side walls in which the surface is superhydrophobic and to measure the convective heat transfer rate through minimally invasive temperature means.

3.6 Acheivements

- Journal paper - “Thermo-Wetting and Friction Reduction Characterization of Microtextured Superhydrophobic Surfaces”, Kim, T. J., Kanapuram, R., Chhabra, A. and Hidrovo, C. H., Journal of Fluids Engineering, Vol. 134, 2012.
- Refereed conference proceeding - “Thermo-Wetting and Friction Reduction Characterization of Microtextured Superhydrophobic Surfaces”, Kim, T. J., Glass, P. and Hidrovo, C. H., 8th ASME/JSME Thermal Engineering Joint Conference, Honolulu, HI, March 13-17, 2011.
- Refereed conference proceeding - “Stability Analysis of Cassie-Baxter State under Pressure Driven Flow”, Kim, T. J. and Hidrovo, C. H., 8th ASME International Conference on Nanochannels, Microchannels, and Minichannels, Montreal, Canada, August 1-5, 2010.

CHAPTER 4

CORRELATION OF HEAT TRANSFER AND FRICTION REDUCTION IN SUPERHYDROPHOBIC FLOWS

4.1 Introduction

In the previous chapters, the behavior of flow over the air-water interface in partially wetting microtextures has been studied. In Chapter 2, the air-water interface was observed to behave close to a no-slip boundary condition by comparing the friction factor between the experimental results and numerical results. Although the textured microchannels experienced a reduction in friction compared to the microchannels with smooth walls, comparison with numerical results suggested that both the magnitude and the trend of the friction reduction followed close to a no-slip boundary condition case. The results suggested that flow over an isolated texture with air pockets may not necessarily be the best way to achieve friction, as suggested in the same chapter that fully wetted microtextures resulted in a greater friction reduction effects. In Chapter 3, joule heaters were placed underneath the microchannels in order to study the stability of the Cassie-Baxter state under heated conditions. While results showed that the air pockets can withstand higher absolute pressures with enough heating, excessive heating was demonstrated to be detrimental to the water flow since the air pocket size expanded into the main water flow section.

The next step of this research would be to study the convective heat transfer effects as the micro-trenched microchannels are heated. As with the previous chapters, the

microtextures are designed as transverse grooves on the side walls of the microchannels in order to understand the slip behavior of the air-water layer under various conditions. Despite the vast literature on friction and drag reduction from superhydrophobic surfaces, there is very little work aimed at correlating the pressure and thermal effects on the stability and characteristics of this condition. While studies have shown the dependence of the overall convective heat transfer rate on slip length [37-39], experimental studies of the convective heat transfer rate over microtextured surfaces under heated wall conditions have not been conducted.

In this chapter, we explore methods to directly heat the side walls where the microtexture are positioned in the microchannels and effectively study the temperature drop within the microchannel through non-intrusive means. Application of heat transfer in the microscale and fabricating microheaters has received significant attention due to its high heat flux capability[40] and lab-on-a-chip applications. In order to locally heat the regions of interest in the microchannels, various methods were explored to integrate the heating elements and the microchannels. Traditionally, conductive materials were deposited and patterned on the substrate bottom and microchannels were placed on top of the heaters. [41] Since patterning the heating element involves multiple fabrication steps, other methods have been sought to simplify the embedding process. Such methods include direct installation of joule heaters into PDMS (Poly-dimethylsiloxane) microchips,[42] injection of conductive,[43] and filling of liquid metals in passages near the microchannels.[44] Siegel et. al[45] suggested the term 'microsolidics' and fabricated a 3-dimentional heating structure wrapped around the liquid microchannel by introducing molten metal into PDMS structures and curing them. In this chapter, we use a low melting temperature alloy to fill the void close to the liquid microchannel and use it as a

microheater that directly heats the side walls of the liquid microchannel. To our knowledge, we are the first to use low melting temperature alloys to fabricate a microheater which can heat the side walls of a PDMS microchannel and characterize the heat removal rate using laser induced fluorescence (LIF).

In order to measure the temperature increase in the heated sections, a minimally-intrusive method, namely the dual fluorescence thermometry (DFT) was employed. The DFT method uses two temperature sensitive fluorescence dyes, and the intensity ratio was measured under different heating conditions. With this technique, the efficiency of the microheater embedded close to the microchannel was investigated, where results show that the losses to the environment are significantly large. While the results demonstrate a low efficiency in the heat removal rate, changing a few parameters, such as increasing the mass flow rate or fabricating taller microheater sizes, increased the efficiency above 50%.

4.2 Background

4.2.1 Temperature Measurement Errors using Thermocouples

In order to measure the convective heat transfer in superhydrophobic microchannels, an accurate measurement of the temperature difference is imperative. Two hypodermic thermocouples (HYP0, Omega) were embedded directly into the microchannel. However, depending on the location where the thermocouple was embedded, the temperature readings were drastically different. As can be observed in Fig. 32, the difference between the temperature measurements from the thermocouple embedded near the outlet (location 0) and the thermocouple embedded close to the heated microchannel section (location 2)

was more than 15˚C. Although it may be desirable to embed the thermocouple deep into the microchannel as possible, the diameter of the thermocouple (0.2mm) was larger than the height of the microchannel. This may lead to uncertainties since the thermocouple will measure the temperature of both the fluid and the punctured PDMS. Another major issue is that embedding a thermocouple is a highly intrusive method, and the microchannel flow can be considerably disturbed as can be seen in the location 2 measurements in Fig. 33.

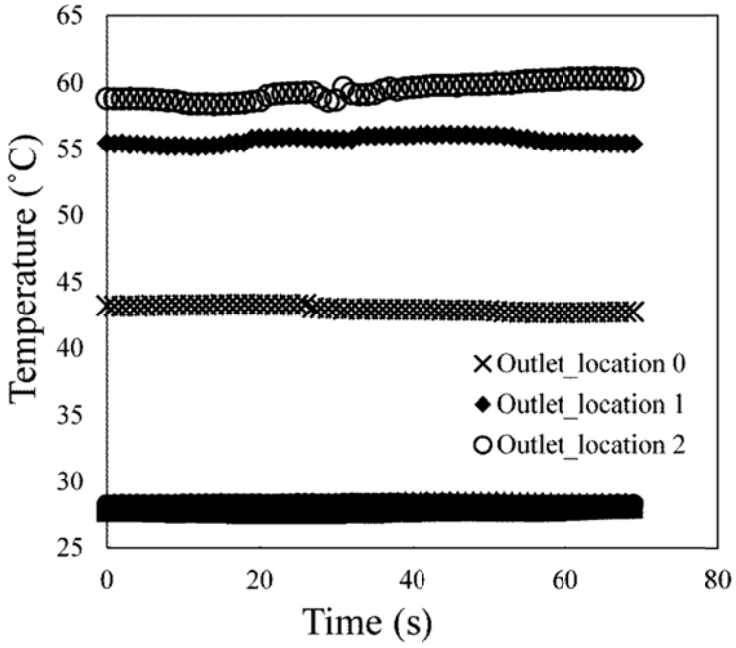

Figure 33. Graph of temperature measurements depending on location of the thermocouples. The inlet temperatures are the data points at the bottom and did not change as much with location.

In order to avoid the issues stated above, a laser induced fluorescence technique was used to measure the fluid temperature. Dual fluorescence thermometry (DFT), in particular, is known to be a minimally intrusive method, as it only requires the fluorophores to be mixed with the working fluid with concentrations in the order of 10^{-5} moles/liter. The following sections explain the principles of the DFT method.

4.2.1 Energy State of Fluorophores

Fluorescence is a light emission by a fluorophore, a chemical compound that can emit light if excited by a photon. As a photon is absorbed by the fluorophore, the fluorophore is excited both electronically and vibrationally (Fig. 34). The maximum energy state of the excited fluorophore is then relaxed vabrationally and drops to the second highest energy state. The energy retained by the fluorophore is then released through radiation and returns to its ground state.

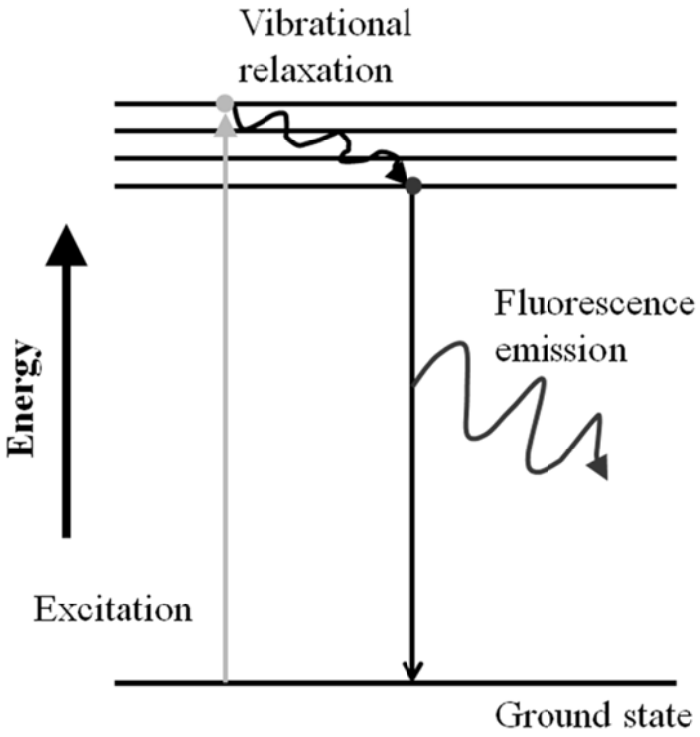

Figure 34. Schematic diagram of the energy state levels of an excited fluorophore.

Since the radiation is emitted at a lower state than the initially excited state, the wavelength is longer than the excitation wavelength. The shift between the excitation wavelength and the emission wavelength is termed as the Stokes' Shift (Fig. 35).

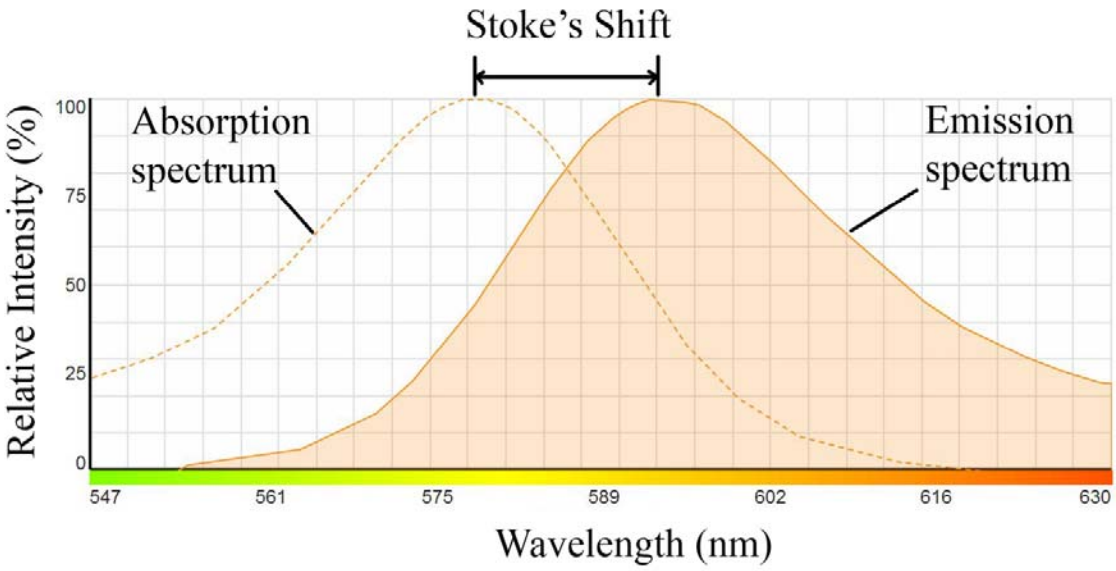

Figure 35. Example of Stokes' Shift for Sulforhodamine 101 (all the spectrum plots hereby presented are referenced from Invitrogen's SpectraViewer).

4.2.2 Optical thickness

In order to quantify the intensity of the fluorescence emission, a number of principles should be considered. The first is the Beer-Lamberts Law which defines the excitation intensity I_{ex} traveling through a solution,

$$\frac{I_{ex}}{I_0} = e^{-\varepsilon(\lambda, pH)cx} \tag{17}$$

where I_0 is the excitation intensity incident on the solution surface, ε is the absorption (extinction) coefficient, c is the molar concentration of the fluorophore, x is the distance

from the solution surface. Eq. (17) depicts that a light traveling through a medium will decay exponentially as a function of ε, c and x. A simple method to confirm this is to point a laser pointer at a fluorophore solution sensitive to the laser point wavelength. Differentiating Eq. (17) yields,

$$\frac{dI_{ex}}{I_0} = -\varepsilon c e^{-\varepsilon c x} dx - \varepsilon x e^{-\varepsilon c x} dc \tag{18}$$

Since the absorptivity is generally affected by the excitation wavelength and the pH of the solution, it is considered as a fixed parameter. Therefore, concentration c and the distance x are the two main terms that can be used as a variable. Depending on the application, it is desirable to control one of the two as a variable and the other as a fixed parameter,

$$\frac{dI_{ex}}{I_0} = -e^{-\varepsilon c x} d(\varepsilon C x) = -e^{-\frac{x}{x'}} d(\frac{x}{x'}) \tag{19}$$

$$\frac{dI_{ex}}{I_0} = -e^{-\varepsilon t c} d(\varepsilon t c) = -e^{-\frac{c}{c'}} d(\frac{c}{c'}) \tag{20}$$

where Eq. (19) sets the solution thickness as the dimensionless variable with $x' = \frac{1}{\varepsilon C}$ and Eq. (20) sets the solution concentration as the dimensionless variable with $c' = \frac{1}{\varepsilon t}$.

The second parameter to quantify the fluorophore emission is the quantum efficiency. For a small differential element of the fluorophore, the Quantum efficiency Φ is the ratio between the emission and excitation intensities,

$$\Phi \equiv \frac{dI_{em}}{dI_{ex}} \tag{21}$$

where I_{em} is the emission intensity. Substituting either Eq. (19) or (20) into Eq. (21), and integrating from 0 to t for Eq. (19) and 0 to C for Eq. (20) yields,

$$I_{em} = \Phi I_0 (1 - e^{-x^*}) \tag{22}$$

$$I_{em} = \Phi I_0 (1 - e^{-c^*}) \tag{23}$$

where $x^* = \frac{t}{x'}$ and $c^* = \frac{C}{c'}$. If the dimensionless solution thickness or the dimensionless concentration is small, the normalized intensity will behave linearly with increasing thickness or concentration and Eqs. (22) and (23) is simplified to,

$$I_{em} \approx \Phi I_0 x^* = \Phi I_0 \varepsilon c t \tag{24}$$

$$I_{em} \approx \Phi I_0 C^* = \Phi I_0 \varepsilon t C \tag{25}$$

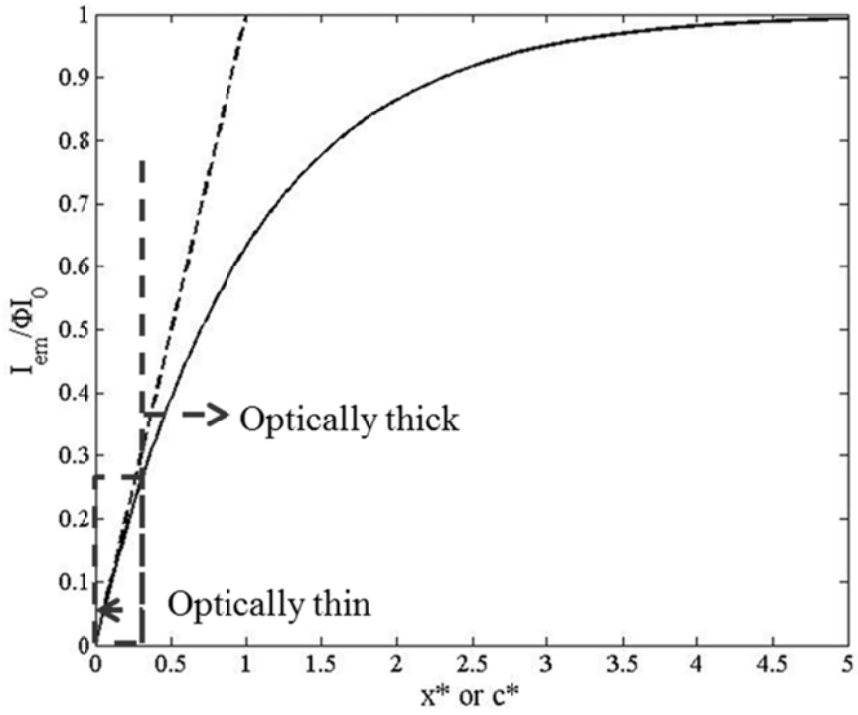

Figure 36. Graph of intensity vs. normalized solution thickness or concentration. It is easier to predict the intensity behavior if operating within the optically thin region.

If the experiment is performed in the linear region, the system is said to be optically thin. Operating in the optically thin system is of particular importance in the experiments performed in this chapter, where the reasons will be explained in the following section.

4.2.3 Dual fluorescence thermometry

Fluorescence thermometry (FT) is known to be an effective alternative to measure the fluid temperature particularly for measuring the temperature in microchannel applications.

This method uses temperature sensitive fluorophores where the emission intensity changes with temperature variation. While FT requires addition of fluorophores into the working fluid, it is advantageous relative to using thermocouples since it negates the issue of physically disturbing the fluid flow or causing errors due to discrepancy in the location the thermocouples are embedded in the microchannel. However, single fluorophore FT must account for all the parameters indicated in Eq. (24) or (25), despite the simplified relation of optically thin systems. In order to further simplify the application of FT in actual experiments, two temperature sensitive fluorophores can be used to track the temperature changes in a fluid flow, namely the dual fluorescence thermometry (DFT).

$$I_{em,1} = I_0 t \Phi_1 C_1 \varepsilon_1(\lambda, pH) \tag{26}$$

$$I_{em,2} = I_0 t \Phi_2 C_2 \varepsilon_2(\lambda, pH) \tag{27}$$

where the subscript 1 and 2 denote the two different fluorophores. The important catch is to take the ratio of the two emission intensities, where the equation becomes,

$$\frac{I_{em,1}}{I_{em,2}} = \frac{I_0 t \Phi_1 C_1 \varepsilon_1(\lambda, pH)}{I_0 t \Phi_2 C_2 \varepsilon_2(\lambda, pH)} = \frac{\Phi_1 C_1 \varepsilon_1(\lambda, pH)}{\Phi_2 C_2 \varepsilon_2(\lambda, pH)} \tag{28}$$

As can be seen in the equation, the intensity of the exciting light and the thickness of the microchannel are now neglected. Since the concentration of the two fluorophores are controlled parameters, and the absorption coefficients are constant if a single wavelength

light source is used and the pH level of the solution is fixed, the ratio of the two emission intensities will essentially be the ratio of the two quantum efficiencies (Fig. 37). Since DFT tracks the ratio of the two fluorophore intensities, it is also beneficial if the intensity of one fluorophore decreases with temperature and the other increases with temperature.[46]

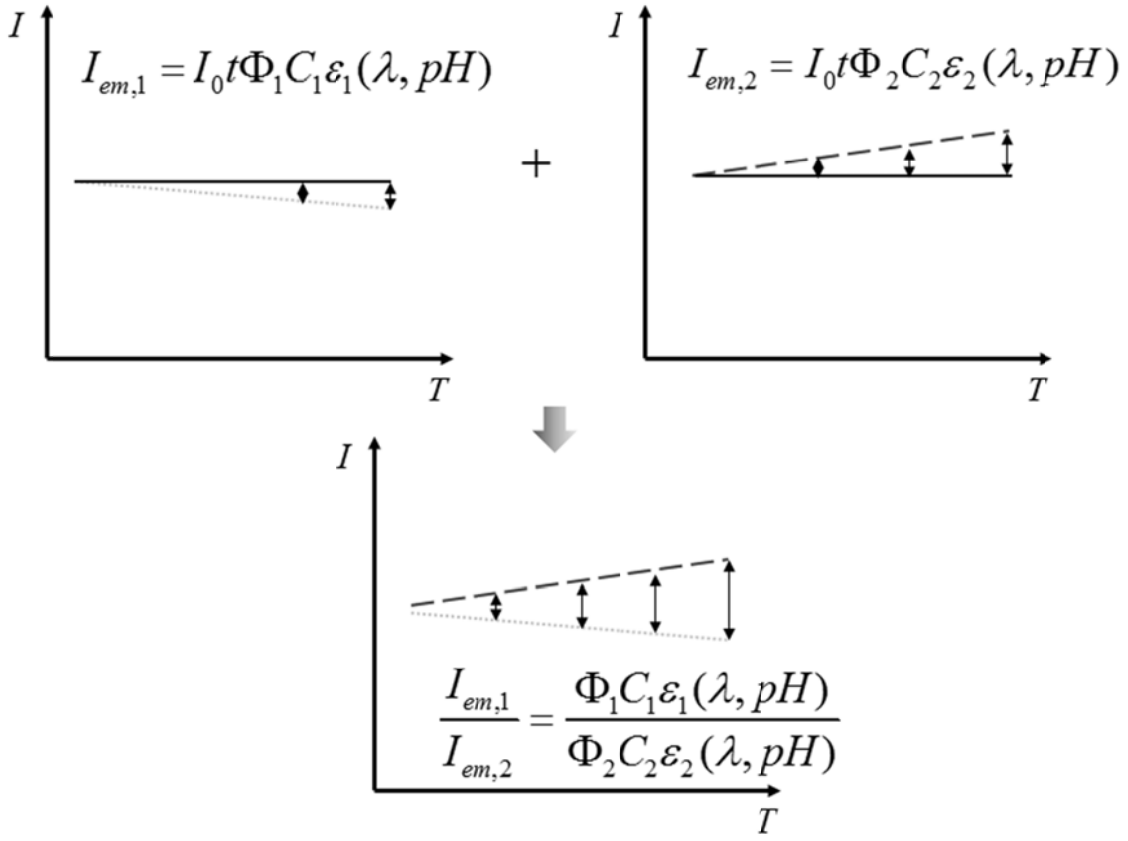

Figure 37. Graphical representation of the dual fluorescence thermometry. While the traditional FT uses one fluorophore, DFT uses the ratio of the two fluorophores to neglect any thickness effects and the excitation intensity measurements are not required.

4.2.4 Sources of error – spectral conflicts

There may be errors associated when performing the DFT, particularly due to overlapping of emission or absorption bands between the two fluorophores. Coppeta and Rogers[47] suggested three different types of possible errors due to the spectral conflicts:

- Type 1 – Type 1 is the most distinguishable spectral conflict, where the two emission bands overlap each other (Fig. 38). This will give incorrect intensity measurements since both intensities are being collected to the CCD detector. This spectral conflict is easily resolved by selecting a separate short pass and long pass emission filter.

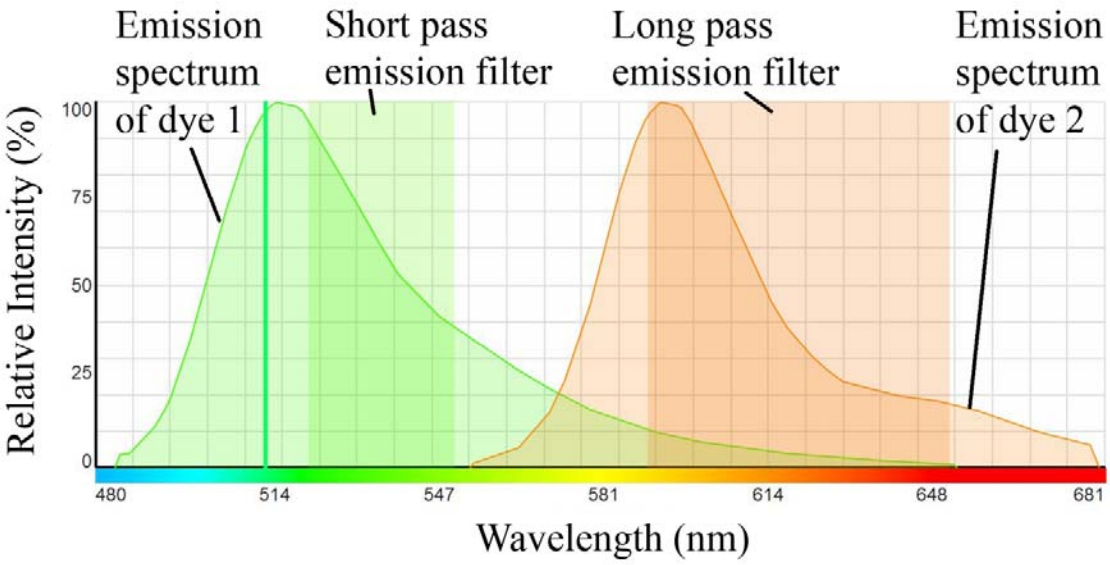

Figure 38. Type 1 spectral conflict between Fluorescein and Sulforhodamine 101. This error can be resolved by selecting different emission filters which is depicted as shaded rectangles. *The actual fluorophores used in the experiment are Fluorescein and Sulforhodamine B.

However, due to availability of the spectral information in Invitrogen's SpectraViewer, Sulforhodamine 101 was selected as a demonstration purpose in describing the spectral errors.

- Type 2 – Type to error occurs when the emission of dye 1 is reduced due to the absorption from dye 2 (Fig. 39).

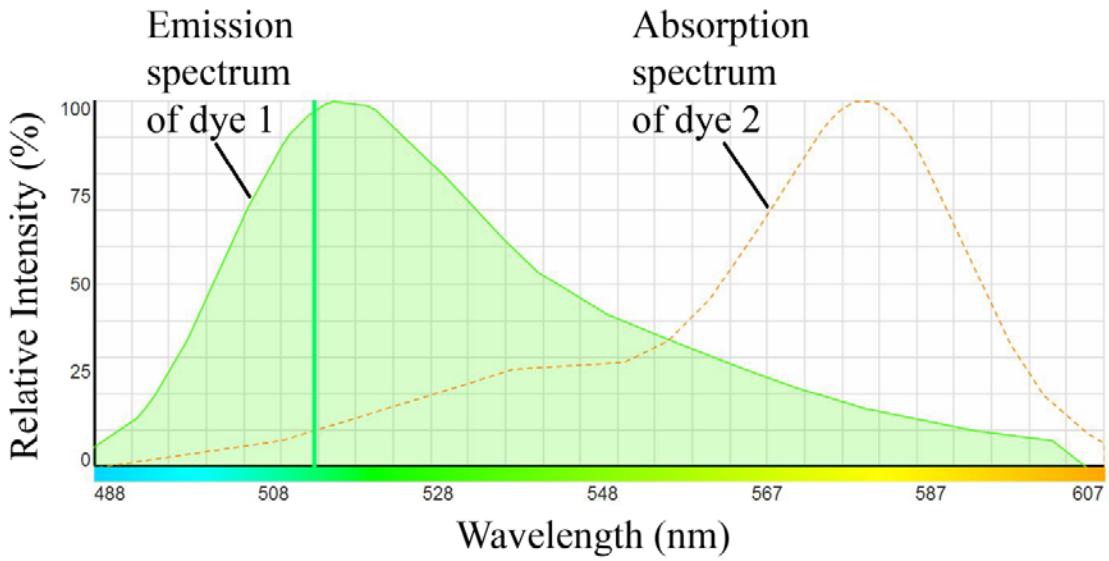

Figure 39. Graphical representation of the Type 2 error. The location where the emission overlaps with the absorption spectrum will result in the reduction of emission of dye 1.

Since the emission from dye 1 is reduced, Eq. (28) is modified to,

$$\frac{I_{em,1}}{I_{em,2}} = \frac{\Phi_1 C_1 \varepsilon_1(\lambda, pH) e^{-\varepsilon_2 C_2 t}}{\Phi_2 C_2 \varepsilon_2(\lambda, pH)} \tag{29}$$

As long as the path length and the pH are kept constant, Eq. (29) can be properly characterized. However, the error can also be minimized if the concentration of dye 2 or the path length of the medium is reduced.

- Type 3 – Type 3 error is the most severe of the three spectral conflicts. Unlike the Type 2 error, Type 3 error alters the absorption band when absorbing the emission from dye 1. In this case, the only method to prevent the error is to select a different type of fluorophore.

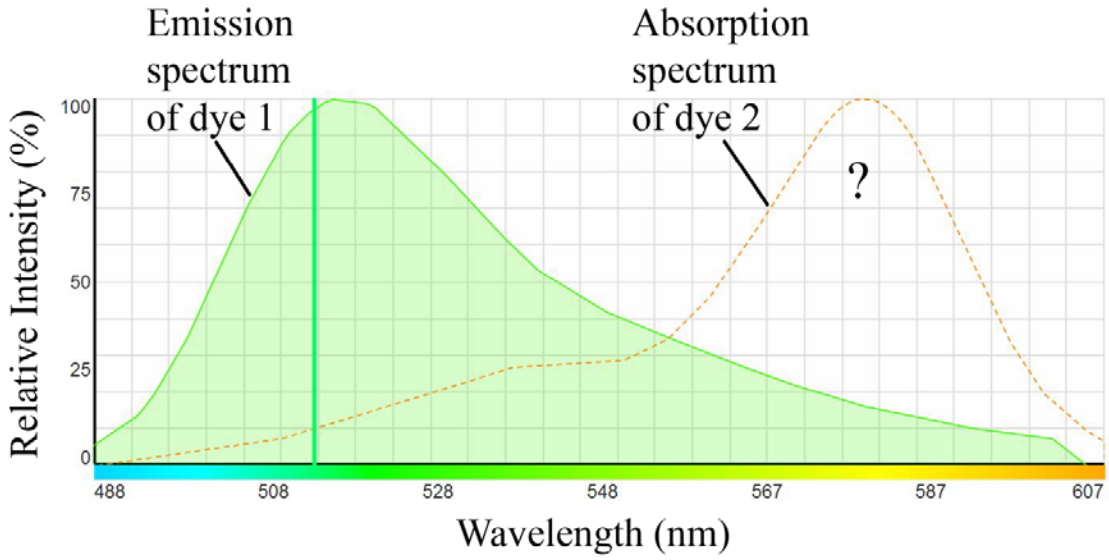

Figure 40. Type 3 spectral error. As seen in the absorption spectrum of dye 2, the aborption band itself is modified, making it impractical for ratiometric applications.

4.3 Experimental Setup

4.3.1 PDMS microchannel fabrication

Su-8 molds were fabricated with Su-8 2075 (Microchem) photoresists using photolithrographic procedures. On the silicon wafer, a positive replicas of the liquid microchannel with dimensions of W= 50μm, H= 100μm, L= 20mm and W= 100μm, H= 100μm, L= 20mm were fabricated. Two pressure ports were designed in the microchannel near the inlet and outlet to measure the pressure drop of the fluid. In the joule heater section, two extra microchannels with cross-sectional area of w= 40μm, H= 100μm were located 40μm away from the main microchannel in order to fill it with the low melting temperature alloy (Fig. 41).

A negative replica of the PDMS microchannel was fabricated using standard soft lithographic procedures from the fabricated Su-8 mold and was bonded to cover slips with oxygen plasma (Harrick Plasma). The bonded microchannels were then stored overnight under standard atmospheric conditions.

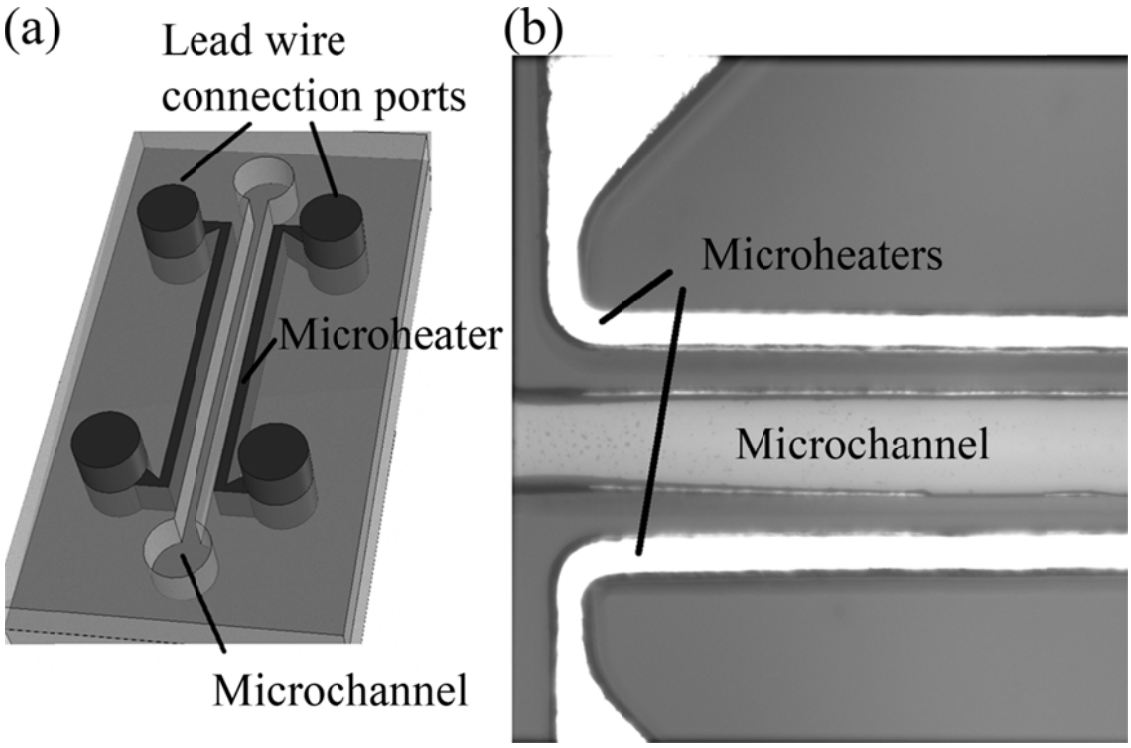

Figure 41. (a) Schematic diagram and (b) micrograph of the microchannel with microheaters embedded next to the microchannel.

4.3.2 Fabrication of Microheaters

A low melting point alloy (Bismuth 58% and Tin 42%, Rotometals) with a melting temperature of 140˚C was used to fabricate the microheaters. This alloy was selected since the melting temperature was higher than 100˚C but within the working temperature of the PDMS.[48]

The alloy was preheated on a hot plate at 160˚C along with the flat tip syringe needle which will be is used to drive the solder into the microheater channel. The solder was dispensed on top of the inlet hole and a positive pressure below 70 kPa was applied by

covering the entire inlet hole and the solder with a 5-gage dispensing needle.

For the resistivity measurement device, the molten solder was flown into a microchannel with dimensions of W= 100μm, H= 100μm, L= 2cm, and the resistivity was measured using a four point probe technique.

In order to ensure that most of the resistance is located near the main microchannel, the resistivity ρ_r of the solder material was measured,

$$\rho_r = R\frac{A}{L} \tag{30}$$

where R is the heater resistance, A is cross-sectional area and L is the length of the joule heater. Two lead wires were connected to each end of the alloy for the current source and another pair of lead wires was connected to a voltage data acquisition device (NI-9215, National Instruments) to measure the voltage drop. A current of 200mA was applied to the alloy and the corresponding resistance was measured across the alloy filled microchannel (Fig. 42).

The temperature dependence on the alloy resistivity was measured by placing the test section on top of a thermoelectric Peltier heater. The bottom of the heater was maintained at constant temperature with a heat exchanger connected to a constant temperature water bath. A hypodermic T-type thermocouple was embedded close to the test section to keep track of the temperature.

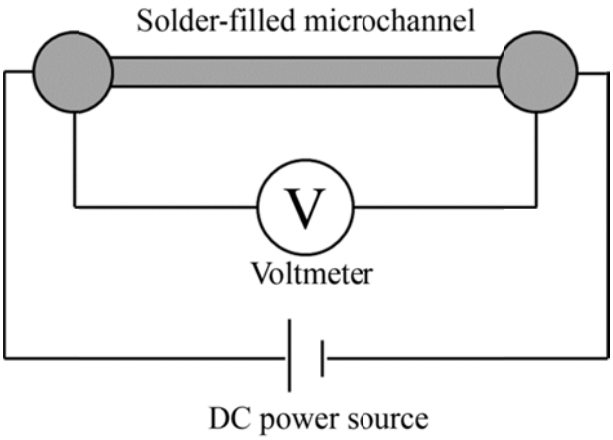

Figure 42. A schematic diagram of the four point probe technique. The low melting point alloy is flown into the microchannel and is soldered to a pair of lead wires, where one is used as a current source and the other is used as a probe connected to a voltmeter.

4.3.3 Differential Pressure Source Setup

Instead of changing the water column height to drive the fluid flow as in the previous two chapters, the experiments performed in this chapter uses a controlled chamber with a pressure regulator connected to a compressed air line. An isolated pressure chamber was necessary as all external light sources must be prevented from exciting fluorphore reservoir. The chamber was pressurized from 200Pa to 7,000Pa (gage) using a pressure regulator (QPV1, Proportionair) connected to a compressed air line. The inlet gage pressure was controlled in order to control the mass flow rate, where the volumetric flow rate was measured using a liquid flowmeter (SLG-0430, Sensirion).

Prior to loading the microchannel to this setup, the air trapped in the PDMS-glass interface was removed by filling the microchannel with water and degassing the microchannel in a vacuum desiccator for approximately an hour.

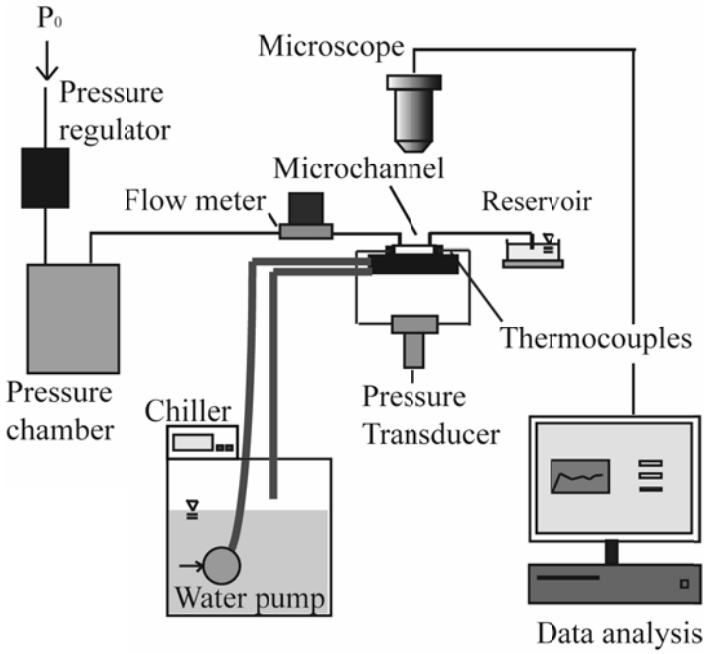

Figure 43. Schematic diagram of the experimental setup.

4.3.3 Preparation of stock solution

In this experiment, Fluorescein (Fl) and Sulforhodamine B (SrB) was selected as the fluorophore and was prepared at pH 8.5. The main advantage of the two fluorophores is that the intensity of Fl decreases with temperature while it is the opposite of SrB[46], which enables a higher ratio value with temperature change. While the Rodamine family is popularly used in fluorescence experiments, it is known to strongly adsorb on to the

PDMS surface. This leads to a significant error since the PDMS walls will have a high concentration of the Rodamine, thus the walls will look brighter in the image. On the other hand Fl and SrB are known to have negligible adsorption on negatively charged surfaces.[49]

In order to maximize and reduce the variation in intensity of the fluorophores, the fluorophore solution was prepared using a Phosphate Buffered Saline (PBS) solution which enables the fluorophore solution to maintain a constant pH. The concentration of the solution was 30μmol/L for both Fl and SrB, where the optically thin condition is satisfied. The solution pH was determined to be 8.5 so that the quantum yield of Fl can be maximized, whereas the quantum yield of SrB is insensitive to changes in pH. Moreover, Fl and SrB are known to have poor adsorption to the PDMS surface, thus increasing the signal-to-noise ratio.[46]

In order to prepare a 1 liter of 0.1 mol/liter PBS solution with pH of 8.5, 26.5ml of Sodium Phosphate Monobasic Monohydrate stock with a concentration of 0.2M and 473.5ml of Sodium Phosphate Dibasic Dihydrate stock with a concentration of 0.2M were mixed. It should be noted that the first solution decreases the pH while the latter solution increases the pH. The solvent is then mixed with 500ml of deoinized (DI) water and is thoroughly stirred using a magnetic stirrer for over 2 hours. Since the highest pH achievable by mixing the two solutions are approximately 8.0, drops of 1M of Sodium Hydroxide was added to the PBS solution until the pH level was increased to 8.5.

The fluorophore solution was then prepared using the 0.1M PBS solution, with a final concentration of 30μM for both Fl and SrB. After the fluorophore solution was significantly stirred using the magnetic stirrer, the solution was filtered through a

Buchner funnel with two layers of glass-fiber filter of 1.5 μm and 0.7μm pore size. Once the final solution was prepared, the solution was stored in a vacuum desiccator for 2 hours.

4.3.4 Dual Fluorescence Thermometry for Temperature Measurement

Dual fluorescence thermometry (DFT) utilizing temperature sensitive fluorophores enables non-intrusive temperature measurements at the microscale. The main advantage of the DFT is its high accuracy due to the highly sensitive fluorescence of the fluorophores to temperatures.[47] At constant pH, *C*, *t* and with a single light source, it is possible to measure solution temperatures from the fluorescent intensities since the quantum yield of the fluorophores is dependent on temperature.

However, the excitation intensity from the light source usually varies over spatially and temporally. Although the laser system used in this experiment demonstrated a power variation of <0.5% over 2 hours, it is necessary to decouple as many variables as possible to simplify the measurement. As explained in Section 4.2.3, the variation in I_{em} from those due to I_0, DFT was implemented by taking the ratio of the two fluorescent dyes.

An argon-ion laser at a wavelength of 514nm (Stellar-Pro Select 150, Modu-laser) was used to excite the fluorophores, and the Fl and SrB emissions were isolated by a dual channel imaging system (DV2, Photometrics). In the microscope, a first dichroic mirror close to the sample reflects the excitation wavelength (λ=514nm) while transmitting fluorescent emissions with longer wavelengths. In the dual channel imaging system, a secondary dichroic mirror transmits the Fl emissions at wavelengths λ<561nm and reflects the longer SrB emission wavelengths at λ>561nm. The Fl and SrB emissions

are further cleaned by passing through a short bandpass filter which transmits wavelengths λ = 522-552nm and a longpass filter that transmits the wavelengths λ = 590-650nm, respectively. The corresponding emission data were collected with a charge-coupled detector device (Coolsnap HQ Diff, Photometrics) with a 12-bit resolution and a single pixel size of 6.45μm.

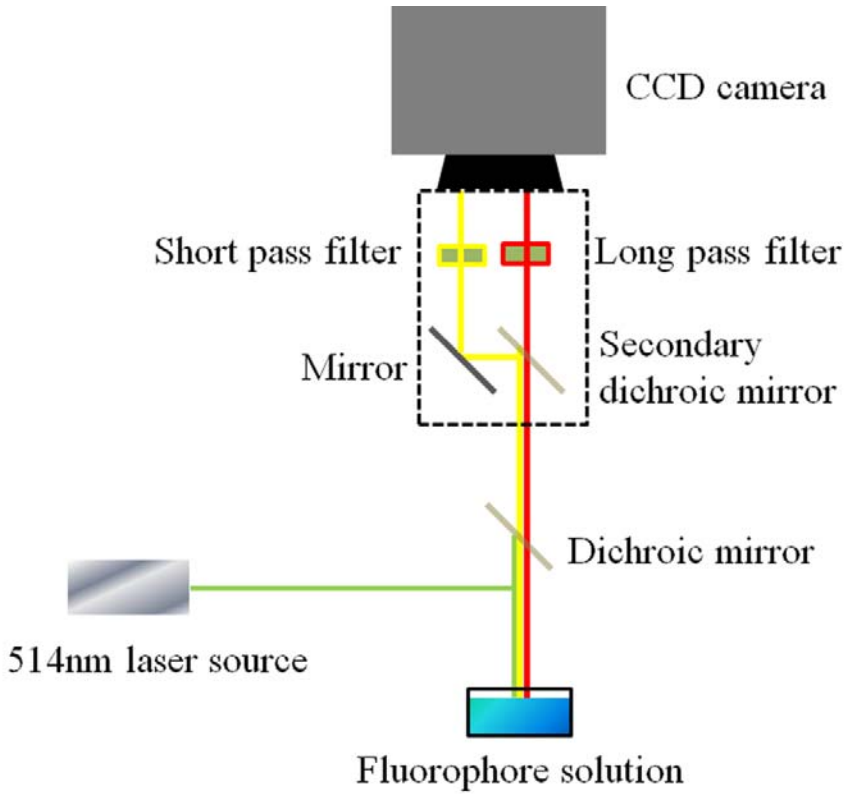

Figure 44. Schematic diagram of the dual fluorescence detection setup. The diagram inside the dotted line are the components of the dual channel imaging system.

It should be noted that the two fluorophores will have spectral errors, as explained in Section 4.2.4. For the Type 1 error, the emission of Fluorescein may roughly account for 10% of the Sulforhodamine B emission. For the Type 2 error, the intensity ratio may

deviate by approximately 2% based on Eq. (29). The aforementioned errors can be resolved by correlating the emission intensity ratio $I_{em,SrB} / I_{em,Fl}$ to individual temperature settings. In order to further increase the reliability of the DFT calibration data, calibration was performed within the PDMS microchannel.

A thermoelectric Peltier heater was placed underneath the microchannel to ensure a constant fluid temperature near the microchannel outlet. The temperature was monitored using a T-type hypodermic thermocouple (HYP0, Omega) with a tip diameter of 0.2mm embedded near the outlet. A 10× objective lens (NA=0.35, Nikon Microscopes) was used to focus the diverging section near the outlet and close to the embedded thermocouple. The water temperature was varied from 25°C to 85°C and the corresponding Fl and the SrB intensity data was collected.

4.3.5 Image pre-processing for dual fluorescence thermometry

Prior to performing ratiometry of the two intensity images, it should be noted that the two emission images are taken in one CCD detector (Fig. 45). Since ratiometry requires two emission images aligned perfectly with each other, simply splitting the image in half and overlapping the two images will lead to a significant error. Hence, one of the two emission data must be processed so that the two images are aligned with each other. Since the two emission data are not spatially identical, the images must be pre-processed in order to match the two emission images to the sub-pixel level.[50-52]

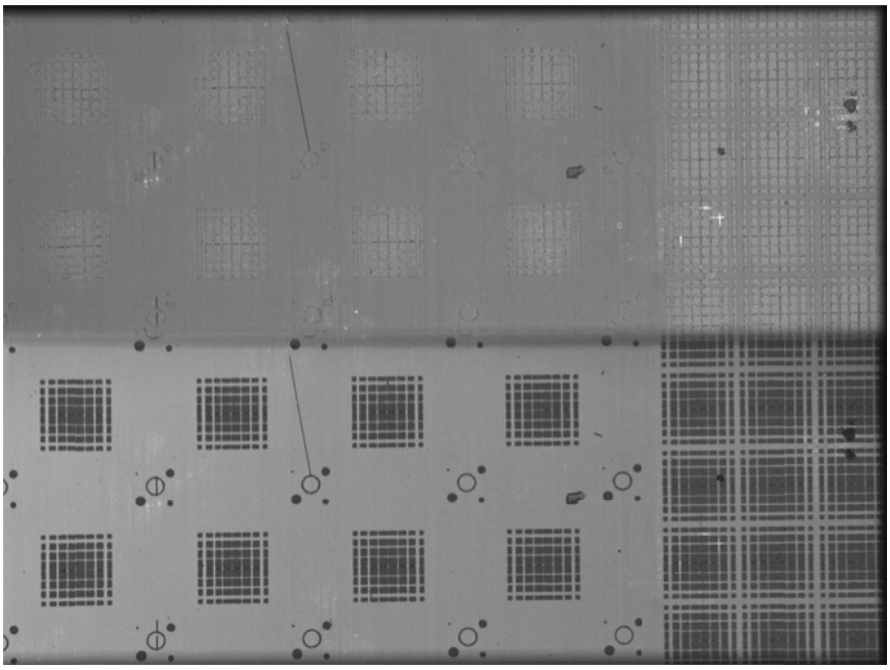

Figure 45. Two emission images of a grid array (supplied by Photometrics) taken from the dual channel imaging system with a 4x objective. Observing the right hand side of the image, it can be seen that the top and bottom images are slightly offset from each other.

In order to align the two emission images, information on how 'distorted' one emission image to the other reference image is required. A map of the displacement vector field can be acquired by imaging sandpaper (Fig. 46(a)) and splitting the two images into two separate files. With these two files as frame A and frame B, micro-particle image velocimetry (μ-PIV) can be performed (Insight 3G, TSI) and a vector field of the grains in frame A relative the frame B is mapped out (Fig. 46(b)). However, since the resolution of the μ-PIV does not correlate the displacement vectors to a single pixel level, the vector field is curve fitted by a cubic relation to fill out all the pixel locations with the displacement vectors.

Once the displacement vector is mapped out to the individual pixel level, the displacement information is applied to frame B of the sandpaper image. Based on the shifted displacement data from the PIV results, the intensity values from the secondary frame were shifted accordingly to a blank frame with the size identical to the reference frame (Fig. 47(b)). As seen Fig. 47(a), the ratiometry will result in incorrect analysis if the secondary image is not processed due to the significant misalignment of the two images. It should be noted that there are losses of information in the corrected secondary image since it is distorted into the center of the frame relative to the reference frame.

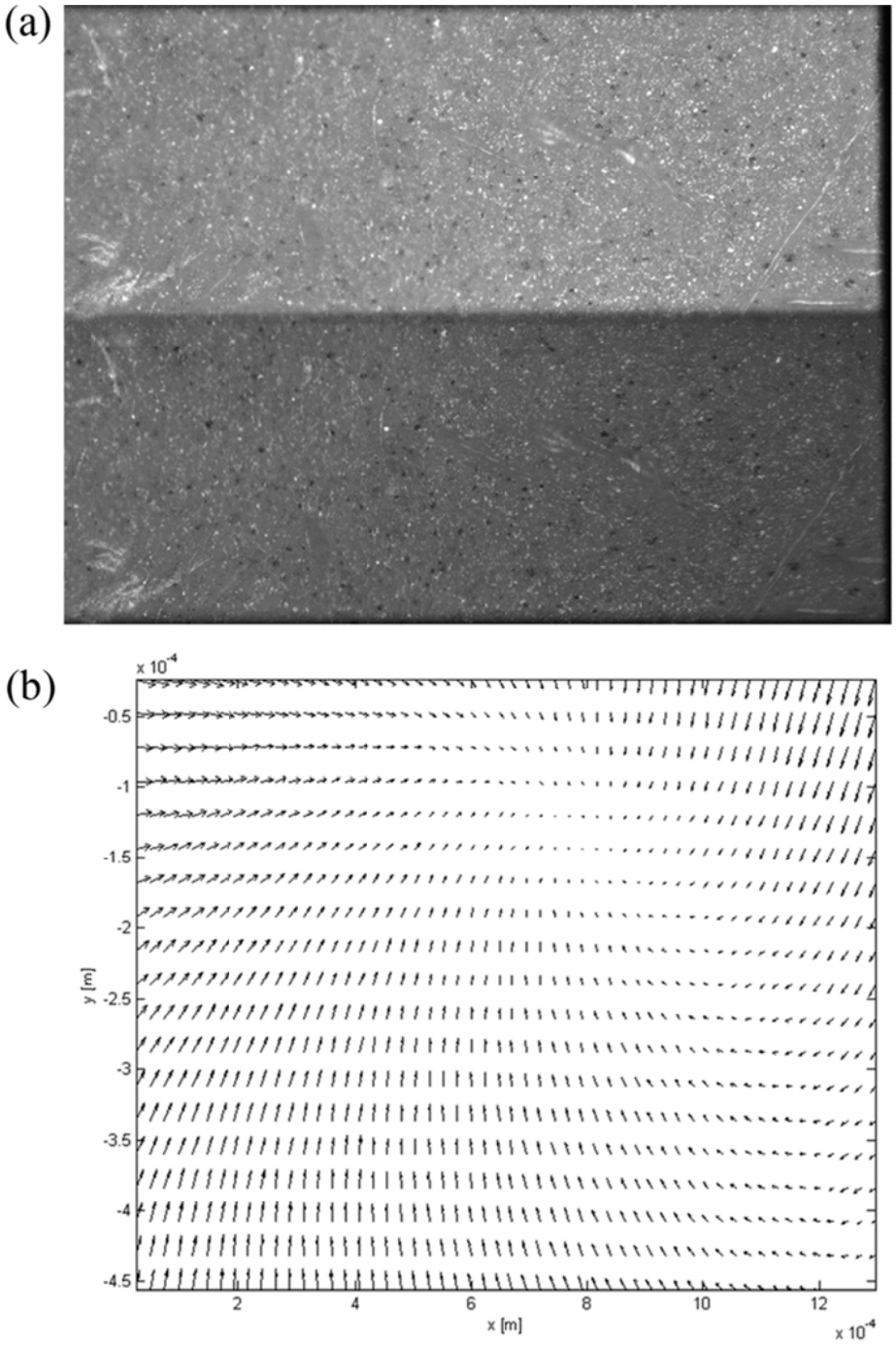

Figure 46. μ-PIV performed on a sandpaper to quantify how distorted and offset the two images are.

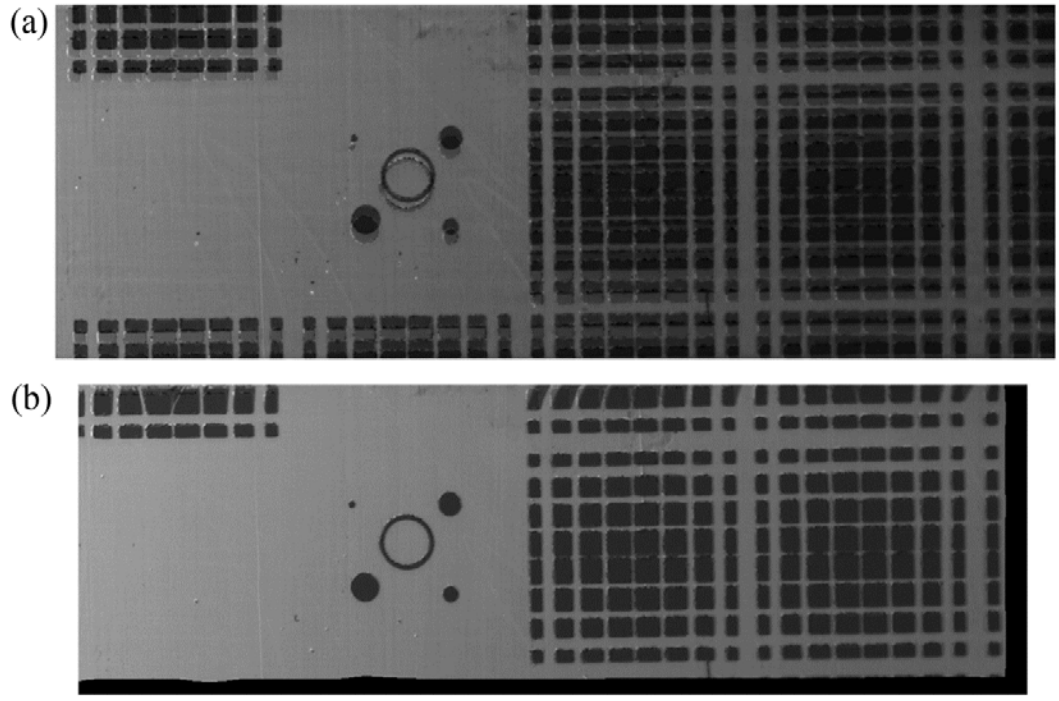

Figure 47. Comparison of the ratiometry correlation by overlapping the two images (*M*= 10x, *NA*= 0.35) taken from the dual channel imaging system for (a) uncorrected original images and (b) displacement corrected images. Since each pixel in frame B has been displaced, there are loss of information and hence a dark band appears at the edge of the image.

4.4 Results

4.4.1 Resistivity of microheaters

The resistivity of the solder alloy was measured using the four-point probe method. The main current was supplied at 200mA and the corresponding resistivity was measured under different temperature conditions. In Fig. 48, the resistivity increases approximately by 28% over the extent of the tested temperature range. Since resistivity increases with temperature, the minimum required current was calculated based on the power requirements.

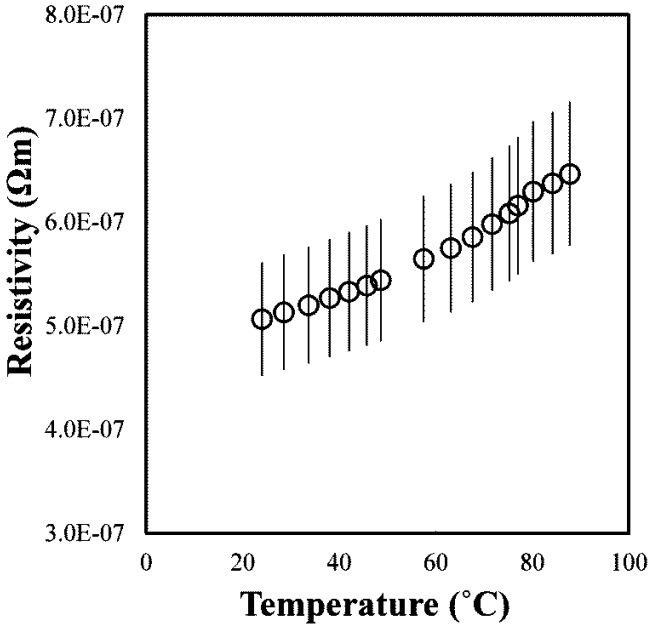

Figure 48. Measurement of resistivity vs. temperature for the Bi-Ti alloy. The error bars represent bias and precision uncertainty with a 95% confidence interval.

4.4.2 Temperature calibration for the DFT

In order to correlate the intensity ratio between the Sulforhodamine-B and Fluorescein solution vs. temperature, the intensity ratio of the two fluorophores was calibrated to the measured temperature value within the microchannel. A hypodermic T-type thermocouple was embedded close to the microchannel outlet (Fig. 49) and micrographs were taken for each temperature setting.

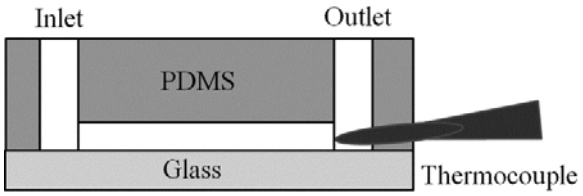

Figure 49. Schematic diagram of the temperature calibration settings, where a hypodermic thermocouple is embedded near the microchannel outlet.

To ensure that the thermocouple is measuring the actual fluid temperature, the temperature gradient in the thermocouple was analytically modeled. The thermocouple is assumed as a cylinder, and the energy balance for a differential element of the cylinder (Fig. 50(a)) is,

$$q_{cond,x} - q_{cond,x+dx} - dq_{conv} = 0 \tag{31}$$

where q_{cond} is the conductive heat transfer and dq_{conv} is the convective heat transfer, and the negative value represents heat transfer flowing out of the differential element. The thermocouple end with the copper-constantan junction is submerged in water at length L_1, and the rest is exposed to air at length L_2. It should be noted that the section where the thermocouple is embedded in PDMS is omitted since the boundary condition is assumed as adiabatic due to its high thermal resistance (Fig. 50(b)).

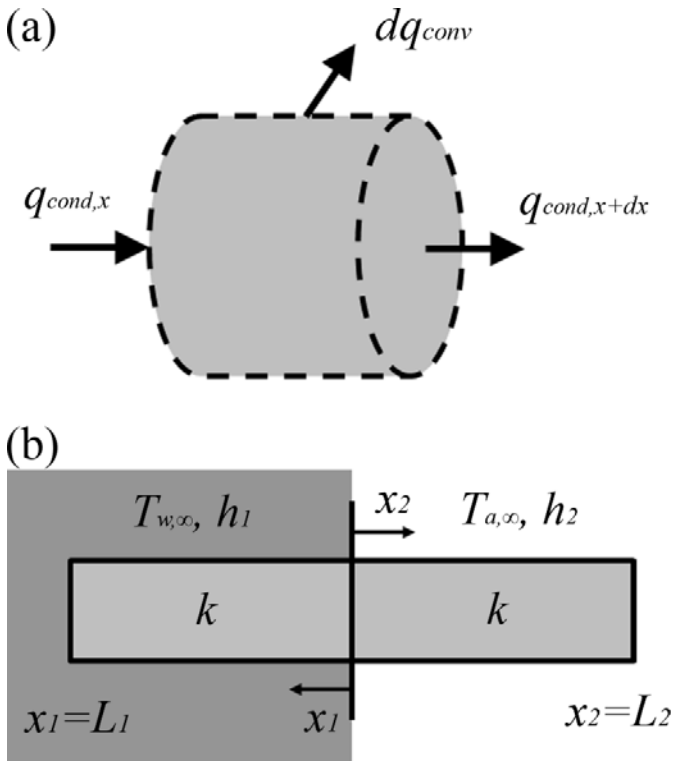

Figure 50. Schematic diagrams of (a) an energy balance of a thermocouple element and (b) the entire thermocouple modeled with length L_1 submerged in water in the microchannel and then immediately exposed to air with length L_2.

Since the thermocouple is divided into two sections with different fluids, the axis of origin is designated as the location where the phase changes (liquid and air), and the corresponding boundary conditions are,

$$
\begin{aligned}
&-kA_c \left.\frac{d\theta_1}{dx_1}\right)_{x_1=L_1} = h_1 A_c \left.\theta_1\right)_{x_1=L_1} \\
&\left.\theta_1\right)_{x_1=0} = \left.\theta_2\right)_{x_2=0} + \theta_{wa} \\
&-kA_c \left.\frac{d\theta_1}{dx_1}\right)_{x_1=0} = kA_c \left.\frac{d\theta_2}{dx_2}\right)_{x_2=0} \\
&\left.\theta_2\right)_{x_2=L_2} = 0
\end{aligned}
\tag{32}
$$

where θ are the relative temperatures ($\theta_1 = T - T_{w,\infty}$, $\theta_2 = T - T_{w,\infty}$ and $\theta_{wa} = T_{a,\infty} - T_{w,\infty}$), k is the thermal conductivity of the metal (assumed as tin), A_c is the cross-sectional area of the thermocouple, h_1 is the heat transfer coefficient of the water and h_2 is the heat transfer coefficient of the air. Solving for Eq. (31) with the boundary conditions from Eq. (32),

$$
\begin{aligned}
T &= C_1 e^{m_1 x_1} + C_2 e^{-m_1 x_1} + T_{w,\infty} \\
C_1 &= \frac{T_{w,\infty}}{2}\left\{1 + \beta\left(\left(1 - \frac{\alpha}{\alpha + e^{-2m_2 L_2}}\right)\left(1 - \frac{m_2}{m_1}\right) + \frac{1}{\alpha + e^{-2m_2 L_2}}\left(1 - \frac{m_2}{m_1}\right)\right)\right\} \\
C_2 &= e^{2m_1 L_1}\left(\frac{m_1 k + h_1}{m_1 k - h_1}\right) C_1
\end{aligned}
\tag{33}
$$

The constants in Eq. (33) are defined as,

$$\alpha = \frac{\frac{2m_2}{m_1} - \left(1 + \frac{m_2}{m_1}\right)\left(1 - e^{2m_1 L_1}\left(\frac{m_1 k + h_1}{m_1 k - h_1}\right)\right)}{\frac{2m_2}{m_1} + \left(1 - \frac{m_2}{m_1}\right)\left(1 - e^{2m_1 L_1}\left(\frac{m_1 k + h_1}{m_1 k - h_1}\right)\right)} \tag{34}$$

$$\beta = \frac{1 - e^{2m_1 L_1}\left(\frac{m_1 k + h_1}{m_1 k - h_1}\right)}{\frac{2m_2}{m_1} + \left(1 - \frac{m_2}{m_1}\right)\left(1 - e^{2m_1 L_1}\left(\frac{m_1 k + h_1}{m_1 k - h_1}\right)\right)}$$

where $m_1 = \frac{h_1 p}{kA_c}$ and $m_2 = \frac{h_2 p}{kA_c}$ (p is the perimeter of the thermocouple cross-section). The temperature profile along the thermocouple can be estimated (Fig. 51(a)) by substituting in the appropriate parameters from Table 5. The analytical model is also compared with the numerical results, where the results agree well with each other.

Table 5. Parameters required in order to calculate Eq. (30). The value of the convective coefficient h_1 is based on $Nu \approx 4.1$ for fully developed flow in a square duct with constant wall temperature[18].

Parameters	r	k	h_1	h_2	$T_{a,\infty}$
Values	100 μm	22 W/m·K	12,000 W/m^2·K	40	298.15 K

Based on the estimated thermocouple tip temperature vs. external water temperature plot (Fig. 51(b)), it can be assumed that the temperature at the thermocouple tip will be close to the actual water temperature and that the fluorescence ratio will be properly correlated to the actual fluid temperature.

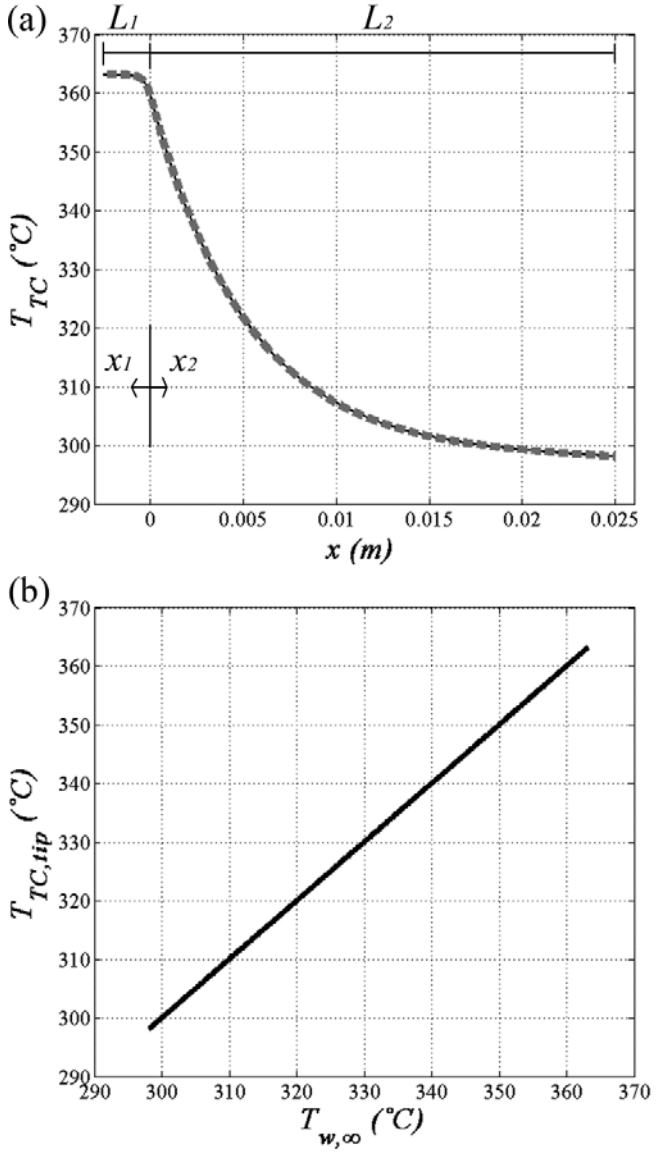

Figure 51. (a) Plot of thermocouple temperature vs. thermocouple location if the water temperature is assumed as 90˚C, where the solid line is the analytical result and the dotted line is the numerical result. (b) Plot of thermocouple tip as a function of the water temperature. The results for this particular case show a linear relation between the two temperatures.

Based on the procedures mentioned in Section 4.3.4, the DFT calibration was performed by comparing the fluorescence emission ratio to the temperature readings from the thermocouple (Fig. 52).

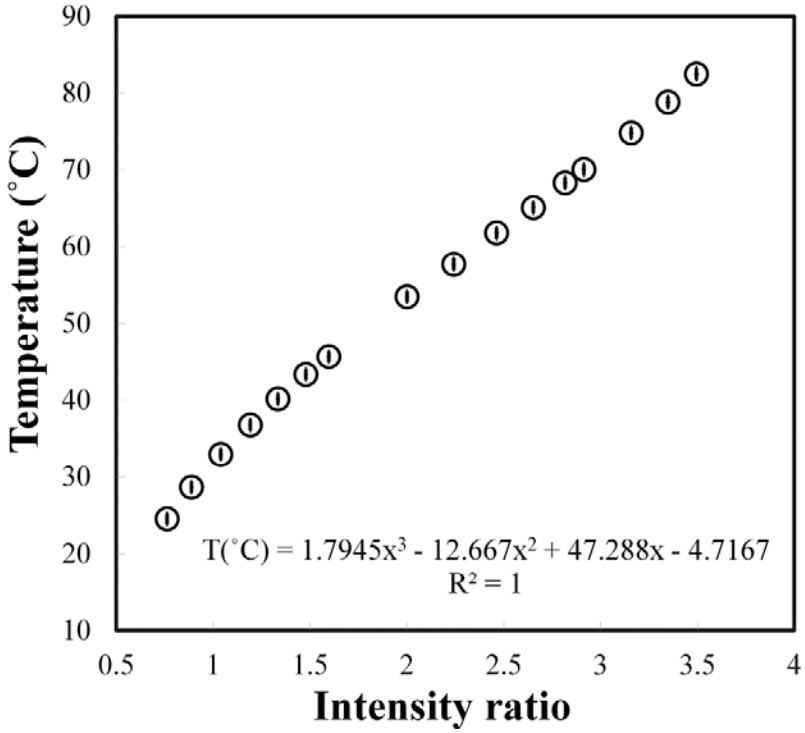

Figure 52. Fluorescence intensity ratio calibration of SrB-Fl under different fluid temperatures. The data has been curve fitted with a parametric cubic polynomial.

Using the calibrated intensity ratio data, the temperature profile across the microchannel was analyzed before and after the microheater section for every power and flow rate settings (Fig. 53).

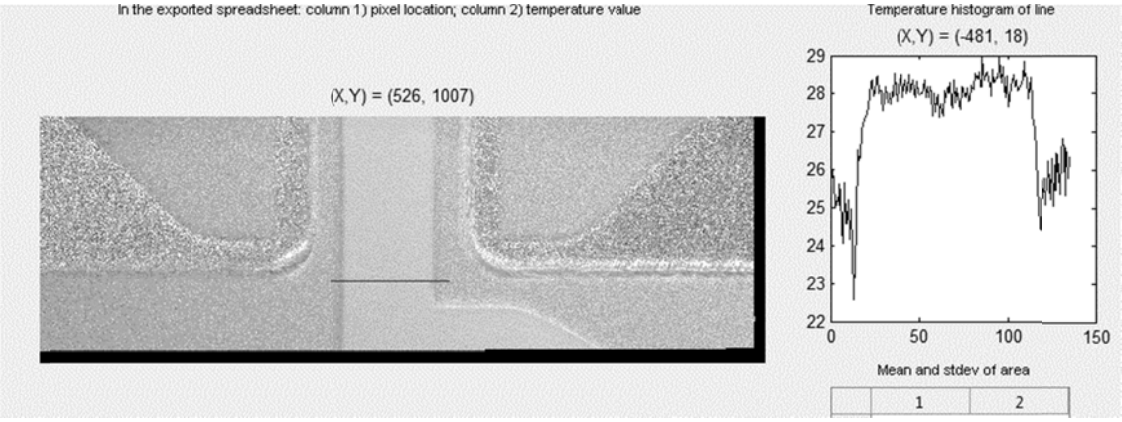

Figure 53. An example of collecting raw data of the temperature profile using the ratio values with the temperature calibrated data.

4.4.3 Bulk temperature measurement in the microchannel

In order to characterize the advective heat transfer, the bulk temperature is calculated from the temperature profile,

$$T_m = \frac{\int \rho u c T dA}{\dot{m}\bar{c}} \tag{35}$$

where ρ is the density of water, u is the axial velocity of the water flow, c is the specific heat of water, and A is the cross-sectional area of the microchannel.

However, since the variation in temperature across the microchannel is within the uncertainty (Fig. 54), the local temperature is assumed as constant across the microchannel. Also, since the specific heat does not vary significantly along the

microchannel cross-section, the integral in Eq. (35) reduces to $\dot{m}\bar{c}\overline{T}$. Since the mass flow rate and the specific heat cancels out, the bulk temperature can be assumed as the average temperature value from the temperature profile data.

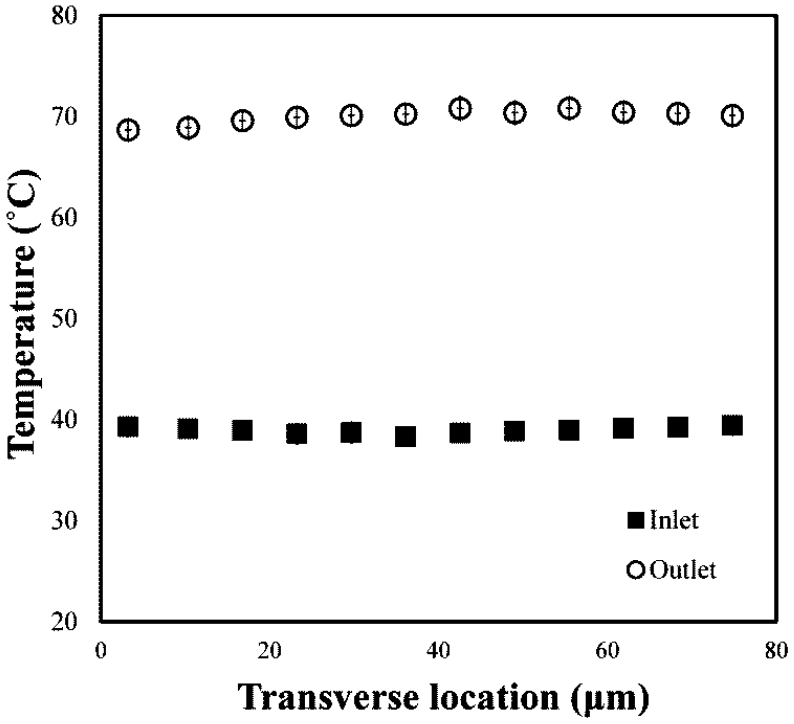

Figure 54. An example of the temperature profile before and after the microheater section. Each data point represents an average of 10 pixels across the microchannel cross-section.

4.4.4 Calculation of heat efficiency η_{eff}

The convective heat transfer efficiency η_{eff} is measured by,

$$\eta_{eff} = \frac{\dot{Q}_{conv}}{\dot{Q}_{in}} \tag{36}$$

where $\dot{Q}_{conv}$ is the convective heat transfer rate and $\dot{Q}_{in}$ is the power supplied by the joule heater. The power supplied by the heater was calculated with $\dot{Q}_{in} = VI$, where V is the voltage and I is the current. The four point probe method is implemented at the junction between the microheaters and the lead wires to neglect the bias from the lead wires. For the numerator in Eq. (36), the convective heat transfer rate was calculated with $\dot{Q}_{conv} = \dot{m}\Delta(cT_m)$, where $\dot{m}$ is the mass flow rate, c is the specific heat of the water and T_m is the bulk temperature. As explained in the previous section, the bulk temperature can be assumed as the measured average temperature across the microchannel.

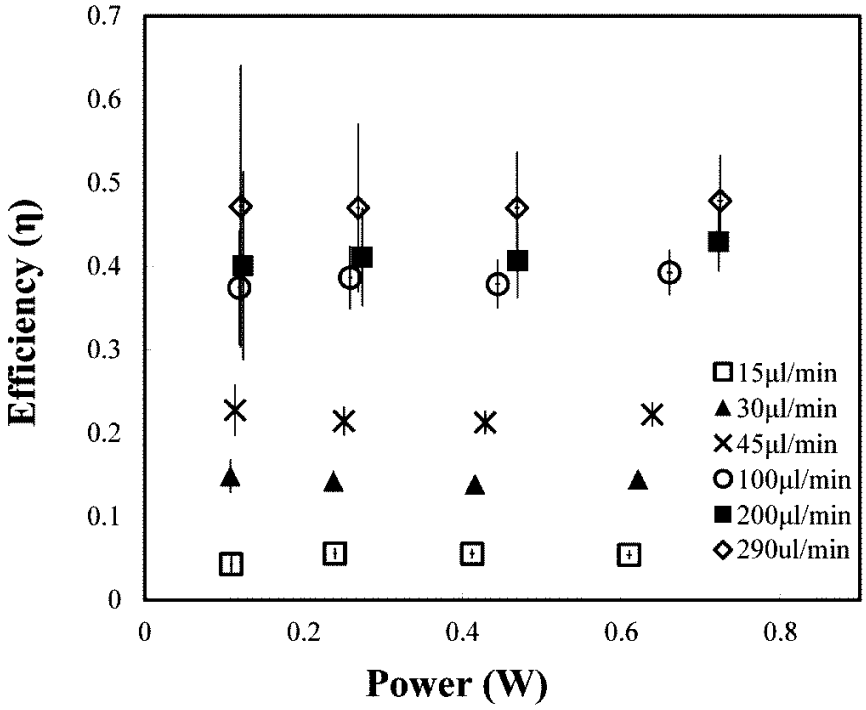

Figure 55. Graph of advective efficiency vs. power for different flowrates. The uncertainty increases for lower power settings due to smaller temperature differences.

As expected, the advective efficiency results indicate that the efficiency is constant with power supplied through the microheaters (Fig. 55). Also, the efficiency increases with higher flow rates since higher mass flow rate can transport energy more efficiently. It should be noted that the uncertainty increases for higher flow rates and/or smaller power input. Since the uncertainty of the current T-type thermocouple ranges from 0.5-1.0˚C, the error relative to the temperature difference will become significant if the mass flow rate or the power supplied to the microheaters is reduced.

4.4.5 Heat Loss Estimation

Although the advective efficiency increased with flow rate in Fig. 55, it was observed that there are limitations on how much the efficiency can increase if the efficiency is plotted as a function of the flow rate. In Fig. 56, the advective efficiency starts off at ~6% at 15μl/min and increases rather linearly up to 100μl/min, where the corresponding efficiency is ~39%. However, the efficiency levels off beyond 100μl/min, where the efficiency reaches 47% even though the flow rate has been further increased to 290μl/min.

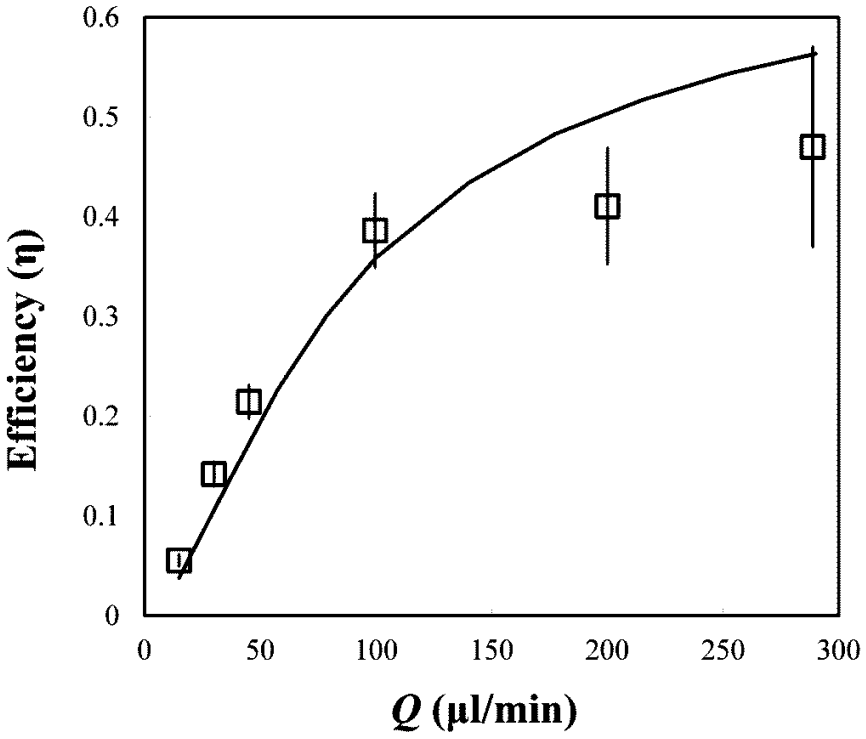

Figure 56. Comparison of numerical and experimental results of efficiency vs. flow rate. The slopes for both cases start levelling off as the flow rate is increased.

Numerical simulation was performed and compared with the experimental results in order to explore the behaviour of heat loss levelling off. The microchannel with integrated microheaters similar to the actual sample was modelled, where properties of PDMS[53-54] and Tin was used to define the material characteristics of the microchannel and microheaters, respectively. A forced convection coefficient of $40 W/m^2 \cdot K$ was set as the boundary condition at the outer layer of the PDMS chip since circulation of air was apparent near the experimental setup due to the fans from the laser, power supply and the camera. The power supplied to the microheaters was set as 244mW, where an approximate lead wire resistance of 4% was implemented. As can be seen in the figure, the numerical results demonstrate a similar behaviour to the experimental results, suggesting that the heat loss to the environment is significant despite the poor thermal conductivity (~$0.25 W/m \cdot K$) of the PDMS.

In order to explore the significance of the heat loss, numerical analysis on thermal resistances ($R_{th} = \frac{\Delta T}{Q}$) is performed as a function of flow rate (Fig. 57). For flow rates under 100µl/min, the advective resistance R_{adv} is dominant and most of the heat is lost to the environment. However, the advective resistance diminishes with $dR_{adv}/d\dot{m} = -1/\dot{m}^2$ and becomes comparable to the heat loss resistance as the flow rate is increased above 100µl/min.

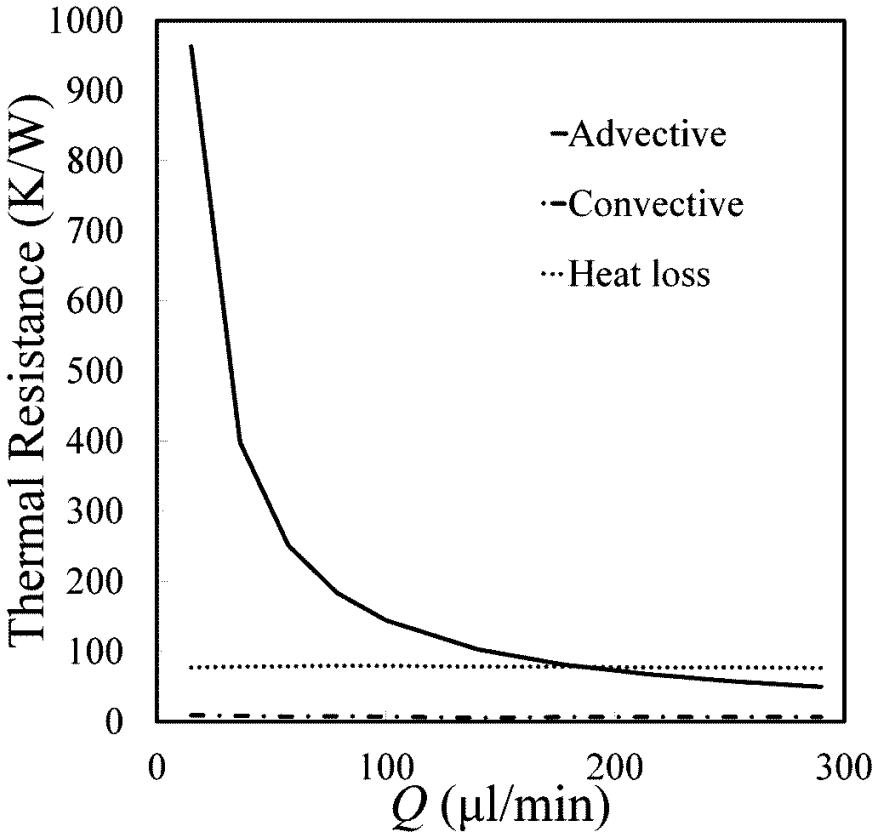

Figure 57. Graph of numerical results on thermal resistance vs. flow rate for different heat transfer modes. The advective resistance is dominant for flow rates under 100μl/min.

It should be noted that while the convective heat transfer resistance is below 13% of the advective resistance for flow rates under 290μl/min, it becomes dominant if the mass flow rate is infinitely increased. It is expected that for very large flow rates, the heat loss to the environment will become negligible, and the advective resistance will become similar to that of the convective resistance. However, since the hydraulic resistance is large for microchannels ($\frac{\Delta P}{Q} \sim \frac{1}{D_h^4}$), it is likely that for realistic applications the advective resistance will be comparable to the heat loss resistance.

4.4.6 Microchannel/Microheater Aspect Ratio Effects on Efficiency

The advective efficiency can be increased by increasing the aspect ratio of the microchannel cross-section. In Fig. 58, microheaters with two different aspect ratios (height/width) of 1.3 and 2.5, corresponding to microchannel heights of 50μm and 100μm, are compared under the power generated at ~250mW.

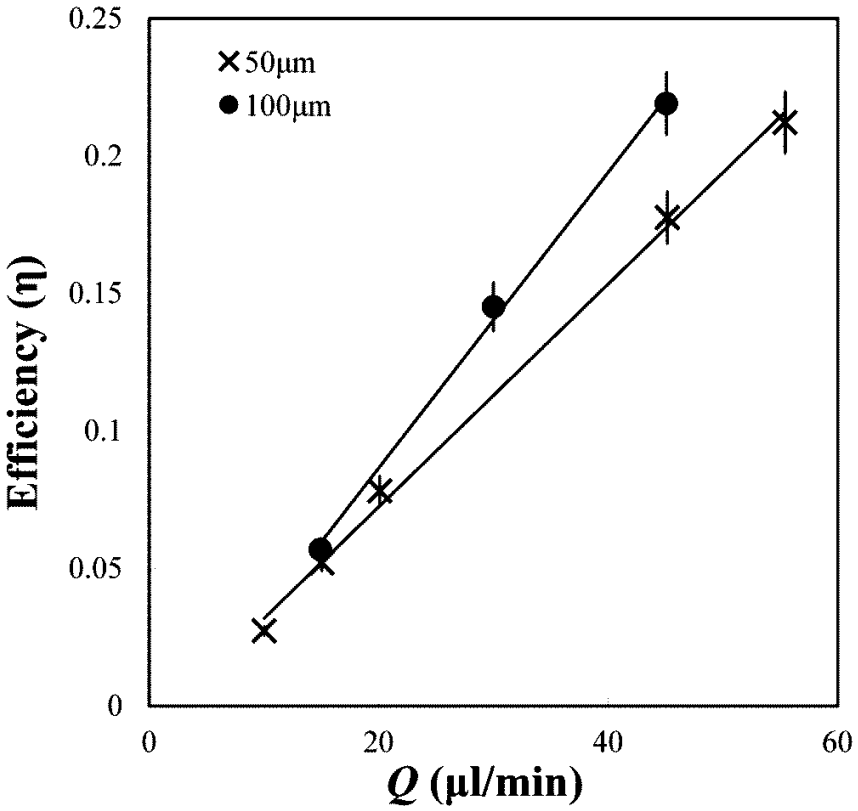

Figure 58. Comparison of heating efficiency vs. flow rate for two different microchannel/microheater heights (50μm and 100μm). A linear line is curve fitted to enhance visualization of the trends.

Results suggest that the efficiency vs. mass flow rate is increased by ~30% as the microheater aspect ratio is increased from 1.3 to 2.5, which is expected since more surface area of the main microchannel is exposed to the microheater. However, the increase in efficiency is not as significant compared to the ~100% increase in the microheater and microchannel aspect ratio.

4.4.7 Possible Sources of Measurement Error

The advective efficiency measurements may be affected by factors other than the heat loss. One such example is the preheating effects of the microchannel near the inlet region, particularly if the flow rate is low in the microchannel and the heating power is large in the microheaters. Since less heat will be removed by advection under low flow rate conditions, the microheaters will likely to conduct heat evenly throughout the entire PDMS slab. Consequently, the water will be significantly heated near the microchannel inlet (Fig. 59). If the room temperature is assumed as the inlet temperature, the advective efficiency will increase by eg. 2-3% at Q= 15μl/min. As the flow rate increases, the preheating effect diminishes and the inlet temperature can be maintained close to the ambient temperature.

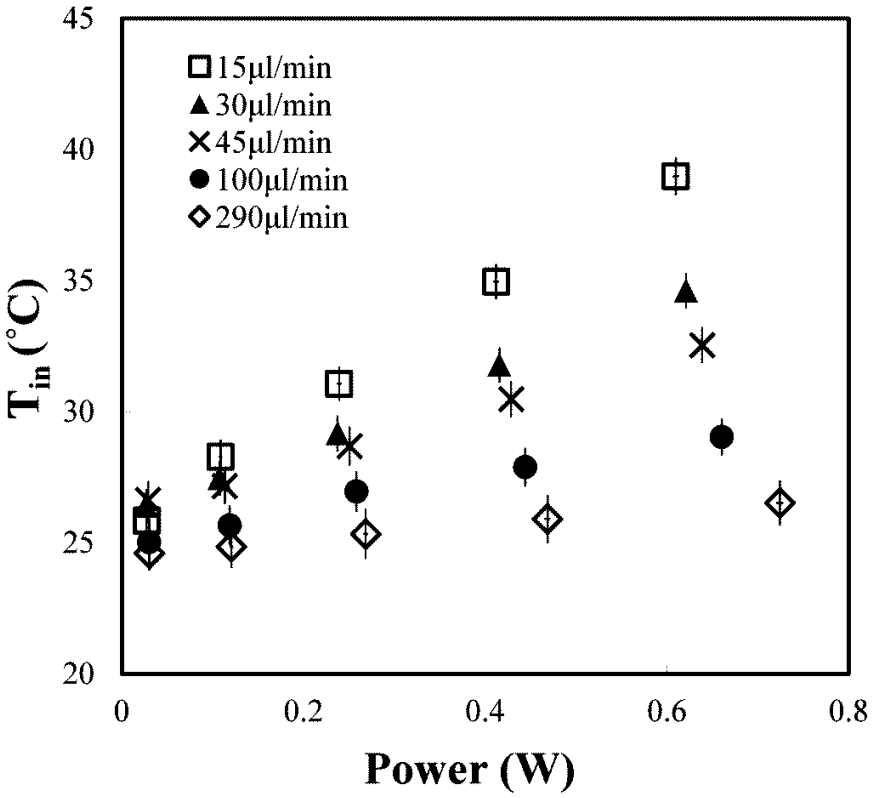

Figure 59. Comparison of water temperature upstream of the heating section for different flow rates.

Another source of error may be caused by the lead wire effects in the microheater section. The microheater is consisted of the main heater section and the converging/diverging section, where the latter section is required to connect the external electric wire. Since the voltage drop was monitored at the electrical wires connected to the microheater inlet and outlet, the measured resistance includes the converging and diverging sections as well. By inspecting the geometrical dimensions of the microheater,

the resistance from the converging/diverging section is approximately 4% of the entire microheater and the efficiency may increase by ~1% if this section is neglected.

Regardless of the possible measurement errors, it can be inferred that the heat loss to the environment is significant. Since the goal of this chapter is to provide a basis to measure the convective efficiency of a superhydrophobic microchannel, achieving a high efficiency system is important. There are a number of suggestions to improve the efficiency. One way is to increase the height of the Su-8 mold. Since the height of the microchannel and the microheater is identical, the advantage in increasing the height will be two-fold: 1) the hydrodynamic resistance will be reduced thus resulting in a higher mass flow rate (and convection) with the same inlet pressure, and 2) the microheater area facing the microchannel will increase, thus reducing the losses towards the top and bottom of the microheater. Another possible method to increase the efficiency is to apply additional thermal resistance at the bottom and top of the microchannel. Since the PDMS has a thermal conductivity of 0.25 W/m·K, it is similar to acrylic. It is possible to at least replace the insulation at the bottom of the microchannel with a different material (eg. mineral wool which has a thermal conductivity coefficient of 0.04 W/m·K).

4.4.8 Correlating Hydrodynamic Resistance to Average Fluid Viscosity

As an extension to understanding the significance of heat loss effects, the hydrodynamic resistance is correlated to the average fluid viscosity in the microchannel, where the viscosity is based on the arithmetic average of the inlet and outlet temperature measurements.Since the microchannel dimensions and the fRe (Eq. (9)) are constant the

hydrodynamic resistance $R_h = \Delta P / Q$ is mainly a function of the fluid viscosity, $R_h = C \cdot \mu$, where the constant C is a function of the microchannel dimension.

Figure 60 compares the hydrodynamic resistance and the averaged viscosity, where the viscosity corresponds to the average temperature measured before and after the heating section. The graph is normalized by the initial values in order to compare if the hydrodynamic resistance and the viscosity maintains a linear relation. If the mass flow is large (Fig. 60(b)), the hydrodynamic resistance and the average viscosity decrease at a similar rate. This indicates that the temperature increases linearly throughout the majority of the microchannel and that the average viscosity of the water can be used to analytically estimate the hydrodynamic resistance. However, for the low mass flow rate case (Fig. 60(a)), the two parameters deviate significantly from each other as the temperature is increased. One explanation for the reason behind this discrepancy is due to the propagation of heat throughout the entire microchannel under low flow rates. Figure 61 represents the numerical results of bulk temperature vs. microchannel location with 244mW heating from the microheaters, which corresponds to $T_{avg} \sim 35^{\circ}C$ in Fig. 60. As seen in Fig. 61, the bulk temperature profile for Q = 15μl/min reaches a maximum near the middle of the PDMS, where the thermal resistance is the largest, and starts to decrease as the fluid travels downstream towards the outlet. The results clearly explain the large discrepancy in trends between the average viscosity and the hydrodynamic resistance: the average viscosity in Fig. 60 is based on the arithmetic mean of the measured bulk temperature near the inlet and outlet while the hydrodynamic resistance is the actual measurement of the fluid hydrodynamic resistance. In order to match the two normalized trends, it is recommended to measure multiple locations along the microchannel to address the nonlinear behaviour of the temperature profile.

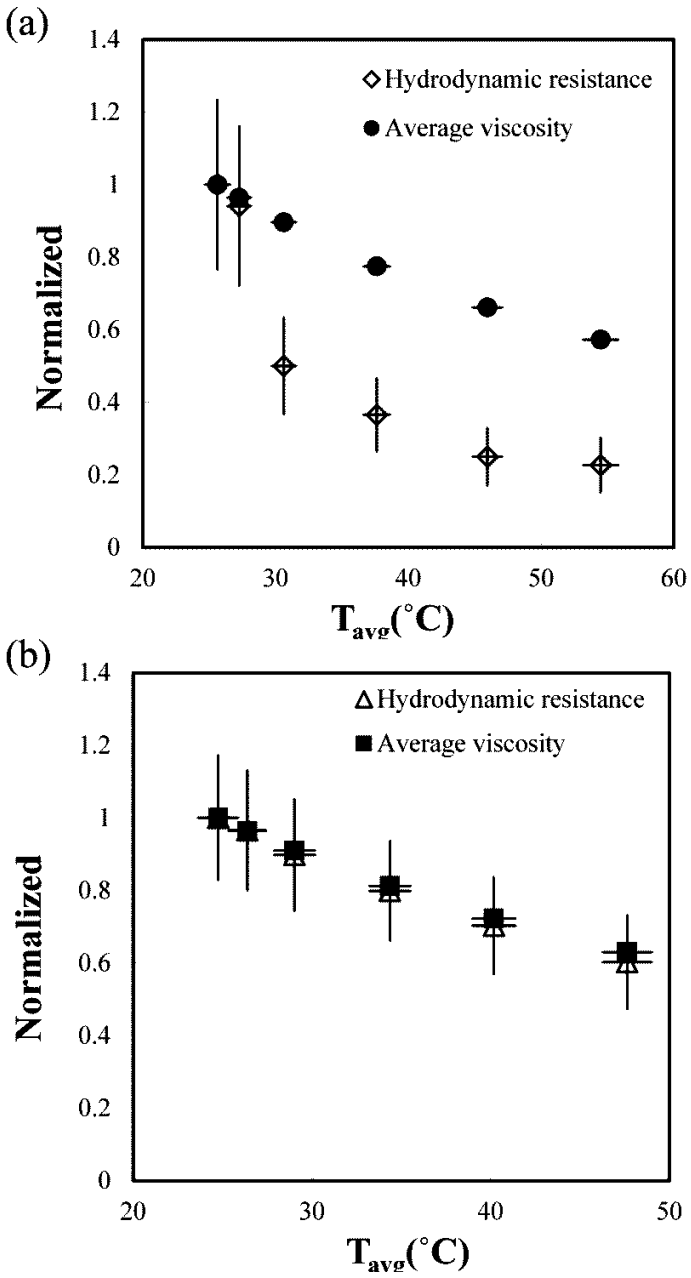

Figure 60. Comparison between the drop in hydrodynamic resistance and the average viscosity with temperature increase in the microchannel for (a) 15µl/min and (b) 100µl/min.

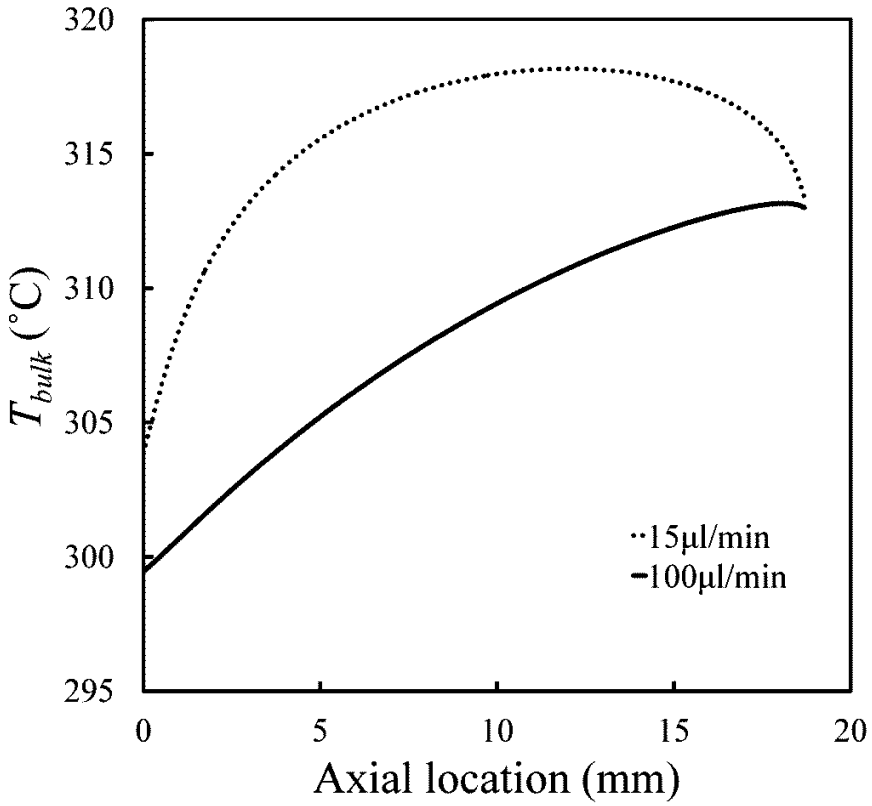

Figure 61. Numerical results of bulk temperature vs. axial location along the microchannel. The power from the microheater is set to 244mW which corresponds to $T_{avg} \sim 35$°C in Fig. 60.

The bulk temperature for a higher flow rate of Q = 100μl/min, on the other hand, increases rather linearly. For this case the arithmetic mean of the temperature to correlate the viscosity is a valid assumption, as can also be implied from Fig. 60(b).

4.5 Conclusion

In this chapter, microheaters that can deliver heat through the microchannel side walls were fabricated and the heat efficiency was evaluated by performing DFT with a continuous laser source. The joule heaters aligned to the side of the microchannel were fabricated by filling the voids with low melting temperature alloys, and the efficiency was performed by analyzing the temperatures upstream and downstream of the microheater section.

Results suggest that an advective efficiency of ~50% can be achieved with a 100μm×100μm (height×width) microchannel if the mass flow rate is increased to 290μl/min and that the heat loss to the environment is dominant (>78%) for flow rates under 50μl/min. Since the heat loss is significant despite the low thermal conductivity of the PDMS (~$0.25 W / m^2 \cdot K$), extra insulation should be applied to the microchip and the height to width aspect ratio of the microheater/microchannel should be increased. Since the purpose of this chapter is to serve as a basis to quantifying heat transfer effects in superhydrophobic microchannels, the results presented here will provide a baseline in designing microheater embedded microchannels.

4.6 Achievements

- Journal paper – "Thermal Efficiency Characterization of Tall Microheaters Embedded in Poly(dimethylsiloxane) Microchannels", submitted

CHAPTER 5

CONCLUSION AND RECOMMENDATIONS

The purpose of this research is to characterize the frictional behavior of superhydrophobic microchannels and compare the results with the conventional assumptions on flow over micro-textured surfaces under the Cassie-Baxter state. The study focuses on three major topics:

1) Quantifying the friction reduction effects in a superhydrophobic microchannel flow under room temperature conditions (Chapter 2)
2) Studying the effects on friction under heated conditions in a superhydrophobic microchannel flow (Chapter 3).
3) Developing methods to deliver heat from the side walls and accurately measure the convective heat transfer effects as an effort to enable measurements on heat transfer in superhydrophobic microchannels for future work (Chapter 4).

In Chapter 2, the friction reduction effects were studied for microchannels with micro-trenches, or transverse grooves, oriented on the side walls. This enable tracking of the air-water interface whether the micro-trenches were wetting or de-wetting. Comparison with numerical results showed that the air-water interface behaved close to a no-slip boundary condition and that the friction may actually increase if the micro-trenches are strongly de-wetting. As the microchannel inlet pressure (hence the *Re*) was increased to the point that most of the micro-trenches were partially wetting, the friction became insensitive to *Re*. This may be attributed to the fact that the streamlines cannot deflect beyond a certain distance into the micro-trench, and the effective flow area will be

constant in the wetting micro-trenches throughout the entire microchannel. The two intitially de-wetted micro-trench experiments were then compared with a fully wetted case where all the micro-trenches were completely wetted prior to the experiment. Comparing the two cases (de-wetted vs. fully wetted), it can be suggested that the fully wetted micro-trenches may lead to significant friction reduction as well. Moreover, for cases where the absolute pressure in the microchannel is small, the fully wetted case may be beneficial over the de-wetted case in terms of maximizing friction reduction.

In Chapter 3, heat transfer is introduced in order to increase the stability of the Cassie-Baxter state. Results showed that heating the micro-trenches can maintain a de-wetted state even if the inlet pressure is high enough to cause the micro-trenches to wet normally under room temperatures. However, if the microchannel is excessively heated, the air-pockets will continue to grow until the main water channel is significantly pinched. This results in a reduction in flow area and the microchannel friction increases until eventually the water layer is completely disrupted due to the air layer merging together. The results presented in this chapter demonstrate that a stable Cassie-Baxter state is achievable if the temperature is carefully controlled. However, because the air pockets sizes are difficult to control with temperature, it can also be inferred that pre-wetting the micro-trenches is more advantageous than trying to maintain the Cassie-Baxter state, considering the results in Chapter 2 that significant friction reduction can be achieved by the Wenzel state as well. It should be noted that the analogy in Chapter 2 and 3 mainly applies to microfluidic channels with micro-grooves transverse to the water flow direction.

In Chapter 4, as part of the future experiments where the final goal is to characterize the convective heat transfer coefficient of flow over micro-trenches under varying

penetration states, microheaters which can heat the side microchannel walls have been fabricated and the temperature measured using laser induced fluorescence. Low melting temperature alloy was introduced into the microheater section of the PDMS device, where the microheater height is identical to the water microchannel. With the embedded microheaters, the convective heat transfer efficiency is characterized by measuring the temperature gradient at the heated section using dual fluorescence thermometry. While ~50% heat removal efficiency was observed, this was mainly achieved by increasing the mass flow rate above 100μl/min. Since our goal is to measure the heat transfer coefficient with the air pockets intact, the mass flow rate introduced in this section is undesirable since the gage pressure within the microchannel will be large enough to flood the air pockets. A few methods can be suggested to reduce the heat losses to the environment such as, adding an extra insulating layer or replacing the insulator with a lower conducting material underneath the microchannel, and increase the PDMS thickness to add extra thermal resistance to the top side of the microchannel.

There are still many questions to be answered regarding the hydrodynamic and heat transfer characteristics of superhydrophobic microchannels. While the friction reduction effects of partially wetting micro-textures have been studied through the measurement of the Darcy friction - Reynolds number product, it is recommended to measure the slip velocity at the air-water interface under different water penetration levels, where one method to experimentally achieve this is by using micro-particle image velocimetry techniques. Moreover, with the apparatus and measurement methods developed to accurately characterize the temperature gradients in the microchannel, it is expected that the convective heat transfer can be measured in the future for flow in superhydrophobic microchannels under different wetting and heating criteria.

REFERENCES

[1]C. H. Choi, U. Ulmanella, J. Kim, C. M. Ho and C. J. Kim, "Effective slip and friction reduction in nanograted superhydrophobic microchannels," Physics of fluids **18** (8), 087105 (2006).

[2]A. V. Belyaev and O. I. Vinogradova, "Effective slip in pressure-driven flow past super-hydrophobic stripes," Journal of Fluid Mechanics, 489 - 499 (2009).

[3]C. Lee and C. J. Kim, "Maximizing the giant liquid slip on superhydrophobic microstructures by nanostructuring their sidewalls," Langmuir **25** (21), 12812-12818 (2009).

[4]D. Byun and H. C. Park, "Drag Reduction on Micro-Structured Super-hydrophobic Surface," in *Proceedings of the 2006 IEEE International Conference on Robotics and Biomimetics* (IEEE, Kunming, 2006), p. 818-823. ISBN: 1-4244-0571-8.

[5]P. Joseph, C. Cottin-Bizonne, J. M. Benoit, C. Ybert, C. Journet, P. Tabeling and L. Bocquet, "Slippage of water past superhydrophobic carbon nanotube forests in microchannels," Physical review letters **97** (15), 156104 (2006).

[6]C. H. Choi and C. J. Kim, "Large slip of aqueous liquid flow over a nanoengineered superhydrophobic surface," Physical review letters **96** (6), 66001 (2006).

[7]C. Cottin-Bizonne, C. Barentin and L. Bocquet, "Scaling laws for slippage on superhydrophobic fractal surfaces," Physics of fluids **24** (1), 012001 (2012).

[8]J. P. Rothstein, "Slip on superhydrophobic surfaces," Annual Review of Fluid Mechanics **42**, 89-109 (2010).

[9]R. N. Wenzel, "Resistance of solid surfaces to wetting by water," Industrial & Engineering Chemistry **28** (8), 988-994 (1936).

[10]C. F. Carlborg, G. Stemme and W. V. D. Wijngaart, "Microchannels with Substantial Friction Reduction at Large Pressure and Large Flow," in *Proceedings of the 22nd IEEE International Conference on Micro Electro Mechanical Systems* (IEEE, Sorrento, 2009), p. 39-42. ISBN: 978-1-4244-2978-3.

[11]M. Jin, X. Feng, J. Xi, J. Zhai, K. Cho, L. Feng and L. Jiang, "Super Hydrophobic PDMS Surface with Ultra Low Adhesive Force," Macromolecular rapid communications **26** (22), 1805-1809 (2005).

[12]L. Bocquet and E. Lauga, "A smooth future?," Nature materials **10** (5), 334-337 (2011).

[13]J. Ou and J. P. Rothstein, "Direct velocity measurements of the flow past drag-reducing ultrahydrophobic surfaces," Physics of fluids **17** (10), 103606 (2005).

[14]J. Ou, B. Perot and J. P. Rothstein, "Laminar drag reduction in microchannels using ultrahydrophobic surfaces," Physics of fluids **16** (12), 4635-4643 (2004).

[15]C. Lee and C. J. Kim, "Underwater Restoration and Retention of Gases on Superhydrophobic Surfaces for Drag Reduction," Physical review letters **106** (1), 14502 (2011).

[16]C. F. Carlborg, M. Do-Quang, G. Stemme, G. Amberg and W. V. D. Wijngaart, "Continuous flow switching by pneumatic actuation of the air lubrication layer on superhydrophobic microchannel walls," in *Proceedings of the 21st IEEE International Conference on Micro Electro Mechanical Systems* (IEEE, Tucson, 2008), p. 599-602. ISBN: 978-1-4244-1793-3.

[17]T. N. Krupenkin, J. A. Taylor, E. N. Wang, P. Kolodner, M. Hodes and T. R. Salamon, "Reversible wetting-dewetting transitions on electrically tunable superhydrophobic nanostructured surfaces," Langmuir **23** (18), 9128-9133 (2007).

[18]R. K. Shah and A. L. London, *Laminar flow forced convection in ducts: a source book for compact heat exchanger analytical data*. (Academic press New York, 1978), p. 256-259.

[19]H. Lorenz, M. Despont, N. Fahrni, J. Brugger, P. Vettiger and P. Renaud, "High-aspect-ratio, ultrathick, negative-tone near-UV photoresist and its applications for MEMS," Sensors and Actuators A: Physical **64** (1), 33-39 (1998).

[20]S. Natarajan, D. Chang-Yen and B. Gale, "Large-area, high-aspect-ratio SU-8 molds for the fabrication of PDMS microfluidic devices," Journal of Micromechanics and Microengineering **18**, 045021 (2008).

[21]I. Papautsky, T. Ameel and A. B. Frazier, "A review of laminar single-phase flow in microchannels," in *Proceedings of the 2001 ASME International Mechanical Engineering Congress and Exposition* (New York, 2001), p. 1-9. ISBN:

[22]E. Lauga and H. A. Stone, "Effective slip in pressure-driven Stokes flow," Journal of Fluid Mechanics **489** (1), 55-77 (2003).

[23]R. S. Figliola, D. E. Beasley and R. Figliola, *Theory and design for mechanical measurements*. (Wiley New York, 1995), p.

[24]A. Mills and B. Chang, "Error analysis of experiments: a manual for engineering students," Unpublished. http://www.seas.ucla.edu/mae/Error_ Analysis_of_ Experiments. pdf (2003).

[25]C. H. Choi, K. J. A. Westin and K. S. Breuer, "Apparent slip flows in hydrophilic and hydrophobic microchannels," Physics of fluids **15**, 2897-2902 (2003).

[26]D. C. Tretheway and C. D. Meinhart, "Apparent fluid slip at hydrophobic microchannel walls," Physics of fluids **14**, L9-L12 (2002).

[27]C. Cottin-Bizonne, A. Steinberger, B. Cross, O. Raccurt and E. Charlaix, "Nanohydrodynamics: The intrinsic flow boundary condition on smooth surfaces," Langmuir **24** (4), 1165-1172 (2008).

[28]J. R. Philip, "Flows satisfying mixed no-slip and no-shear conditions," Zeitschrift für Angewandte Mathematik und Physik (ZAMP) **23** (3), 353-372 (1972).

[29]C. Ybert, C. Barentin, C. Cottin-Bizonne, P. Joseph and L. Bocquet, "Achieving large slip with superhydrophobic surfaces: Scaling laws for generic geometries," Physics of fluids **19**, 123601 (2007).

[30]J. Hyväluoma and J. Harting, "Slip flow over structured surfaces with entrapped microbubbles," Physical review letters **100** (24), 246001 (2008).

[31]A. Steinberger, C. Cottin-Bizonne, P. Kleimann and E. Charlaix, "High friction on a bubble mattress," Nature materials **6** (9), 665-668 (2007).

[32]R. Clift, J. R. Grace and M. E. Weber, *Bubbles, drops, and particles*. (Academic press New York, 1978), p. 38 - 41.

[33]A. Lafuma and D. Quéré, "Superhydrophobic states," Nature materials **2** (7), 457-460 (2003).

[34]A. B. D. Cassie and S. Baxter, "Wettability of porous surfaces," Trans. Faraday Soc. **40** ( ), 546-551 (1944).

[35]T. J. Kim and C. H. Hidrovo, "Stability Analysis of Cassie-Baxter State under Pressure Driven Flow," in *Proceedings of* (ASME, 2010), p. ISBN:

[36]A. Mata, A. J. Fleischman and S. Roy, "Characterization of polydimethylsiloxane (PDMS) properties for biomedical micro/nanosystems," Biomedical Microdevices **7** (4), 281-293 (2005).

[37]R. Enright, M. Hodes, T. R. Salamon and Y. Muzychka, "Analysis and Simulation of Heat Transfer in a Superhydrophobic Microchannel," in *Proceedings of* (ASME, Washington, 2010), p. 157-168. ISBN:

[38]D. Maynes, B. Webb and V. Soloviev, "Analysis of Laminar Slip-Flow Thermal Transport in Microchannels With Transverse Rib and Cavity Structured Superhydrophobic Walls at Constant Heat Flux," in *Proceedings of* (ASME, Honolulu, 2011), p. T10120. ISBN:

[39]D. Maynes, B. Webb and J. Davies, "Thermal transport in a microchannel exhibiting ultrahydrophobic microribs maintained at constant temperature," Journal of Heat Transfer **130** (2), 022402 (2008).

[40]T. M. Harms, M. J. Kazmierczak and F. M. Gerner, "Developing convective heat transfer in deep rectangular microchannels," International Journal of Heat and Fluid Flow **20** (2), 149-157 (1999).

[41]K. Sun, A. Yamaguchi, Y. Ishida, S. Matsuo and H. Misawa, "A heater-integrated transparent microchannel chip for continuous-flow PCR," Sensors and Actuators B: Chemical **84** (2), 283-289 (2002).

[42]R. Fu, B. Xu and D. Li, "Study of the temperature field in microchannels of a PDMS chip with embedded local heater using temperature-dependent

fluorescent dye," International Journal of Thermal Sciences **45** (9), 841-847 (2006).

[43]D. Vigolo, R. Rusconi, R. Piazza and H. A. Stone, "A portable device for temperature control along microchannels," Lab on a Chip **10** (6), 795-798 (2010).

[44]M. D. Dickey, R. C. Chiechi, R. J. Larsen, E. A. Weiss, D. A. Weitz and G. M. Whitesides, "Eutectic Gallium-Indium (EGaIn): A Liquid Metal Alloy for the Formation of Stable Structures in Microchannels at Room Temperature," Advanced Functional Materials **18** (7), 1097-1104 (2008).

[45]A. C. Siegel, D. A. Bruzewicz, D. B. Weibel and G. M. Whitesides, "Microsolidics: Fabrication of Three-Dimensional Metallic Microstructures in Poly (dimethylsiloxane)," Advanced Materials **19** (5), 727-733 (2007).

[46]M. Kim and M. Yoda, "Dual-tracer fluorescence thermometry measurements in a heated channel," Experiments in Fluids **49** (1), 257-266 (2010).

[47]J. Coppeta and C. Rogers, "Dual emission laser induced fluorescence for direct planar scalar behavior measurements," Experiments in Fluids **25** (1), 1-15 (1998).

[48]W. W. Y. Chow, K. F. Lei, G. Shi, W. J. Li and Q. Huang, "Microfluidic channel fabrication by PDMS-interface bonding," Smart Materials and Structures **15** (1), S112 (2005).

[49]K. D. Suda-Cederquist, "Near-Wall Thermometry via Total Internal Reflection Fluorescence Micro-Thermometry (TIR-FMT)," (2007).

[50]C. H. Hidrovo and D. P. Hart, "Emission reabsorption laser induced fluorescence (ERLIF) film thickness measurement," Measurement Science and Technology **12** (4), 467 (2001).

[51]S. Saeki, D. P. Hart and C. H. Hidrovo, "Spectroscopic Study on YAG (532) Laser Dyes using DELIF for Oil Film Thickness and Temperature Measurement," Journal of the Visualization Society of Japan **21** (Suppl 2), 19-20 (2001).

[52]M. David, D. Fogg, C. H. Hidrovo, R. Flynn and K. Goodson, "Development and calibration of a two-dye fluorescence system for use in two-phase micro flow thermometry," in *Proceedings of* (IEEE, 2006), p. 79-86. ISBN: 0780395247.

[53]B. Yang and Q. Lin, "A latchable microvalve using phase change of paraffin wax," Sensors and Actuators A: Physical **134** (1), 194-200 (2007).

[54]Z. Han and A. Fina, "Thermal conductivity of carbon nanotubes and their polymer nanocomposites: a review," Progress in Polymer Science **36** (7), 914-944 (2011).